

SPECIFIC INTERACTIONS OF CARBON DIOXIDE IN SUPERCRITICAL FLUID  
PROCESSES AND NANOPARTICLE PROCESSING

Except where reference is made to the work of others, the work described in this dissertation is my own or was done in collaboration with my advisory committee. This thesis does not include proprietary or classified information.

---

Philip Wesley Bell

Certificate of Approval:

---

Steve Duke  
Associate Professor  
Chemical Engineering

---

Christopher B. Roberts, Chair  
Department Chair  
Chemical Engineering

---

Ram B. Gupta  
Professor  
Chemical Engineering

---

Yoonkook Park  
Assistant Professor  
Tuskegee University

---

Stephen L. McFarland  
Dean  
Graduate School

SPECIFIC INTERACTIONS OF CARBON DIOXIDE IN SUPERCRITICAL FLUID  
PROCESSES AND NANOPARTICLE PROCESSING

Philip Wesley Bell

A Dissertation

Submitted to

the Graduate Faculty of

Auburn University

in Partial Fulfillment of the

Requirements for the

Degree of

Doctor of Philosophy

Auburn, Alabama  
December 16, 2005

SPECIFIC INTERACTIONS OF CARBON DIOXIDE IN SUPERCRITICAL FLUID  
PROCESSES AND NANOPARTICLE PROCESSING

Philip Wesley Bell

Permission is granted to Auburn University to make copies of this dissertation at its discretion, upon request of individuals or institutions and at their expense.  
The author reserves all publication rights.

---

Signature of Author

---

Date of Graduation

## VITA

Philip Wesley Bell, son of Joseph Allen Bell, Junior and Sandra Pattillo Bell, was born on October 27, 1979, in Atlanta, Georgia. He graduated suma cum laude from Woodward Academy in May of 1997. He attended the California Institute of Technology and graduated with a Bachelor of Science degree in Chemical Engineering in June of 2001. In August of 2001, he entered the Graduate School at Auburn University.

DISSERTATION ABSTRACT

SPECIFIC INTERACTIONS OF CARBON DIOXIDE IN SUPERCRITICAL FLUID  
PROCESSES AND NANOPARTICLE PROCESSING

Philip Wesley Bell

Doctor of Philosophy, December 16, 2005  
(B.S., California Institute of Technology, 2001)

222 Typed Pages

Directed by Christopher B. Roberts

Specific interactions of molecules with supercritical carbon dioxide (CO<sub>2</sub>) are of fundamental importance to the understanding of current processes and to the development of new processes. While relatively weak interactions are important for solubility and dissolution concerns, strong interactions play a major role in reaction chemistry. Chapter 1 provides background information on the solvent characteristics of CO<sub>2</sub>, FTIR and NMR spectroscopy methods to examine high-pressure solutions and specific solvent-solute interactions. It also gives motivation to further examine solute-solvent interactions in CO<sub>2</sub> and to apply knowledge of these interactions to various processes.

Chapter 2 discusses the utilization of Fourier transform infrared (FTIR) spectroscopy to study the effect of CO<sub>2</sub> density on the dimerization of various carboxylic acids. The interaction of CO<sub>2</sub> with the carboxylic acid functional group is shown to be relatively strong. These strong interactions can be used to manipulate reactions involving carboxylic acids.

Chapter 3 discusses the use of high pressure nuclear magnetic resonance (NMR) spectroscopy to probe the nature of the interactions between CO<sub>2</sub> and carboxylic acids. The change of the chemical shift of the acidic proton of a carboxylic acid with CO<sub>2</sub> density is shown to be nonlinear, suggesting a specific interaction with CO<sub>2</sub>. Unfortunately, the acid peak is the composite of the monomer and the dimer peaks, so the changing equilibrium constant with CO<sub>2</sub> density also results in a nonlinear change with CO<sub>2</sub> density. These effects on the peak shift are therefore indistinguishable.

Chapter 4 discusses the visualization of the supercritical fluid antisolvent (SAS) precipitation process. This process takes advantage of the interactions of CO<sub>2</sub> with an injected solvent to cause mutual diffusion leading to the precipitation of an insoluble solute. This process can show drastically different behavior by simple adjustments of the processing parameters.

Chapter 5 discusses new methods of polymerization in a reactive SAS process. The interaction of CO<sub>2</sub> with amine groups is used to form nylon 6 during the spray process. The mass transport in this process is also developed. In a different process, the interaction of CO<sub>2</sub> with carboxylic acids is used to dissolve methacrylic acid so that sonication induced polymerization can occur during the SAS process. The polymethacrylic acid formed in this process is precipitated because of its insolubility in

CO<sub>2</sub>. Each of these polymerizations resulted in low yields. More experiments need to be performed to advance the development of these processes.

Chapter 6 discusses the stable dispersion of silver nanoparticles in CO<sub>2</sub> using a non-fluorinated ligand, isostearic acid. The ability of CO<sub>2</sub> to solvate the tails of the short, stubby, methylated ligand allows for steric stabilization of the nanoparticles in CO<sub>2</sub>. Silver nanoparticles are stably dispersed in both a CO<sub>2</sub>/hexane mixture and in pure CO<sub>2</sub>. Particles are also synthesized and dispersed in CO<sub>2</sub> in a single step without the use of any fluorinated compounds. This process again takes advantage of the ability of CO<sub>2</sub> to solvate branched, methylated tails by using a branched, methylated silver precursor. These results are the first reports of stable steric dispersions of nanoparticles in CO<sub>2</sub> without the use of any fluorinated compounds.

Chapter 7 provides conclusions. The IR studies showed a relatively strong interaction between CO<sub>2</sub> and carboxylic acids. High pressure NMR studies were used to probe the nature of this interaction. High resolution imaging of the SAS process showed that the spray characteristics could be significantly changed by adjusting the processing parameters. Two new polymerization techniques were explored in a reactive SAS process that takes advantage of specific interactions with CO<sub>2</sub>. Finally, the ability of CO<sub>2</sub> to effectively solvate the tails of isostearic acid was used to synthesize and disperse silver nanoparticles in CO<sub>2</sub>. These are the first examples of sterically stabilized dispersions of nanoparticles in CO<sub>2</sub> without any fluorinated compounds.

## ACKNOWLEDGEMENTS

I would like to thank Dr. Christopher B. Roberts for his wonderful guidance during my graduate work at Auburn University. I cannot imagine having had a better, more enthusiastic advisor. I would also like to thank Dr. Yoonkook Park for both his guidance and his development of the apparatus and techniques used in the IR studies.

Thanks to all my fellow group members and the group members of Dr. Gupta who helped every day both through discussions and experimentally. Amol Thote helped tremendously with the *ab initio* calculations in support of the IR work. Thanks to Dr. Jessop for the high-pressure NMR cell design and Joe Aderholdt for fabricating the cells. I would like to thank Dr. Livant, Dr. Beckman, and Dr. Eckert for allowing me use of NMR instruments at Auburn University, the University of Pittsburgh, and Georgia Tech, respectively. Thanks to Colin Thomas for his help in collecting the NMR data. Without Amendi Stephens' hard work, the spray process photography would not have been possible. I would like to thank Ranjit Thakur for his collaboration on the polymerization work. Thanks to Madhu Anand, Dr. Chandler McLeod, and Dr. Liu for help with nanoparticle synthesis and dispersion. Thanks to Xin Fan for the solubility data.

Without the support of my family, throughout my educational career, I would not be where I am today. Last, but not least, I would like to thank my wife, Gracie Kelley Bell, who has kept me focused during my graduate studies.

The following publications were a product of this dissertation:

P. W. Bell, A. J. Thote, Y. Park, R. B. Gupta, and C. B. Roberts, "Supercritical Fluid Solvent Effects On Carboxylic Acid Dimer Formation," Proceedings of the 6<sup>th</sup> International Symposium on Supercritical Fluids, Versailles, France, paper no. PTp14, 2003

P. W. Bell, A. J. Thote, Y. Park, R. B. Gupta, and C. B. Roberts, "Strong Lewis Acid-Lewis Base Interactions between Supercritical Carbon Dioxide and Carboxylic Acids: Effects on Self-Association," *Industrial & Engineering Chemistry Research*, (2003), 42(25), 6280-6289

P. W. Bell, A. P. Stephens, C. B. Roberts, and S. Duke, "High-Resolution Imaging of the Supercritical Antisolvent Process," *Experiments in Fluids*, (2005), 38(6), 708-719

P. W. Bell, M. Anand, Fan, X., R. M. Enick, and C. B. Roberts, "Stable Suspensions of Silver Nanoparticles in Carbon Dioxide without Use of Fluorinated Compounds" *Langmuir*, released on web

Computer software used: Microsoft Office, ImageJ, Endnote 6.0, Guassiar98, Omnic E.  
S. P. 5.1

## TABLE OF CONTENTS

LIST OF FIGURES	xvi
LIST OF TABLES	xxv
CHAPTER 1	
INTRODUCTION	
INTRODUCTION	1
SOLVENT NATURE OF CO <sub>2</sub>	3
NUCLEAR MAGNETIC RESONANCE STUDIES	15
SUPERCRITICAL FLUID PARTICLE FORMATION STUDIES	23
IMPACT OF CO <sub>2</sub> INTERACTIONS IN NANOPARTICLE SYNTHESIS AND DISPERSION	28
CONCLUSIONS	32
CHAPTER 2	
IR STUDIES OF CARBON DIOXIDE EFFECTS ON CARBOXYLIC ACID DIMERIZATION CONSTANTS	
INTRODUCTION	35
EXPERIMENTAL METHODS	37
MATERIALS	37
APPARATUS	37
PROCEDURE	38
DETERMINATION OF EQUILIBRIUM CONSTANTS	40

MODELING	41
RESULTS AND DISCUSSION	43
FORMIC ACID	43
PROPIONIC ACID	44
TRIFLUOROACETIC ACID (TFA)	47
<i>AB INITIO</i> COMPUTATIONS	49
ESTABLISHMENT OF THE PRESENCE OF TRIFLUOROACETIC ACID LINEAR DIMER IN CO <sub>2</sub>	51
CONCLUSIONS	52
CHAPTER 3	
NMR INVESTIGATIONS OF SPECIFIC INTERACTIONS BETWEEN CARBON DIOXIDE AND CARBOXYLIC ACIDS	
ABSTRACT	70
INTRODUCTION	71
EXPERIMENTAL	72
RESULTS	73
DISCUSSION	74
CHAPTER 4	
HIGH-RESOLUTION IMAGING OF THE SUPERCRITICAL ANTISOLVENT PROCESS	
ABSTRACT	82
INTRODUCTION	82
THEORY	84
DESCRIPTION OF EXPERIMENTS	90
SAS APPARATUS	90

IMAGING SYSTEM APPARATUS	91
MATERIALS	92
PROCEDURE	92
VISUALIZATION RESULTS	94
DISCUSSION	98
EVALUATION AND CAPABILITIES OF VISUALIZATION TECHNIQUE	101
CONCLUSIONS	102
ACKNOWLEDGMENTS	103
CHAPTER 5	
POLYMERIZATION AND PRECIPITATION DURING THE SUPERCRITICAL ANTISOLVENT PRECIPITATION PROCESS	
ABSTRACT	113
INTRODUCTION	113
EXPERIMENTAL METHODS	115
MATERIALS	115
APPARATUS	116
PROCEDURE	116
RESULTS	117
TRANSPORT MODEL FOR NYLON 6 FORMATION	119
POLYMERIZATION OF CAPROLACTAM	122
MASS TRANSPORT IN THE SUPERCRITICAL ANTISOLVENT PROCESS	125
OVERALL TRANSPORT MODEL	129
CONCLUSIONS	130

CHAPTER 6  
STABLE DISPERSIONS OF SILVER NANOPARTICLES IN CARBON  
DIOXIDE WITH FLUORINE-FREE LIGANDS

ABSTRACT	140
INTRODUCTION	141
EXPERIMENTAL	144
MATERIALS	144
AG-AOT-TMH SYNTHESIS	144
PHASE BEHAVIOR MEASUREMENTS	145
NANOPARTICLE SYNTHESIS	146
PARTICLE IMAGING	147
INFRARED SPECTROSCOPY	147
PARTICLE DISPERSIONS	147
ONE-STEP SYNTHESIS AND STABILIZATION IN CO <sub>2</sub>	150
RESULTS AND DISCUSSION	150
CONCLUSIONS	159
CHAPTER 7	
CONCLUSIONS	
IR STUDIES OF CARBON DIOXIDE EFFECTS ON CARBOXYLIC ACID DIMERIZATION CONSTANTS	179
NMR INVESTIGATIONS OF SPECIFIC INTERACTIONS BETWEEN CARBON DIOXIDE AND CARBOXYLIC ACIDS	180
HIGH-RESOLUTION IMAGING OF THE SUPERCRITICAL ANTISOLVENT PROCESS	181

POLYMERIZATION AND PRECIPITATION DURING THE SUPERCRITICAL ANTISOLVENT PRECIPITATION PROCESS	183
STABLE DISPERSIONS OF SILVER NANOPARTICLES IN CARBON DIOXIDE WITH FLUORINE-FREE LIGANDS	184
CONCLUSION	185
REFERENCES	186

## LIST OF FIGURES

Figure 2-1	Experimental setup for high-pressure FTIR measurements.	58
Figure 2-2	Schematic diagram of a high-pressure cell: A, housing; B, window holder; C, cap; D, ZnSe window; E, lead sheet; F, inlet, outlet temperature, and pressure port.	59
Figure 2-3	Generalized carboxylic acid dimerization equilibrium where $K$ is the dimerization constant and $R$ is a carbon chain.	60
Figure 2-4	FTIR spectra of the C=O stretching band for formic acid in carbon dioxide at 303 K and 88 bar.	61
Figure 2-5	Variation of $K$ for formic acid with density along different isotherms in carbon dioxide and ethane solvents. The solid lines indicate the MLFHB modeling results and the dashed lines represent linear extrapolations to the gas phase $K$ values (Park, Gupta et al. 2002).	62
Figure 2-6	Variation of $K$ for propionic acid with density along different isotherms in carbon dioxide and ethane solvents. The solid lines indicate the MLFHB modeling results.	63

- Figure 2-7 TFA spectra taken at 25 °C and 82.7 bar in CO<sub>2</sub>. The three peaks shown correspond to the monomer, cyclic dimer, and linear dimer of TFA in that order as the wavenumber decreases. 64
- Figure 2-8 TFA spectra taken at 25 °C and 117 bar in CO<sub>2</sub>. At this density (0.841 g/cm<sup>3</sup>), only two distinct peaks, corresponding to the monomer and the cyclic dimer of TFA, are observed. The third peak, corresponding to the linear dimer of TFA, has essentially vanished. 65
- Figure 2-9 Variation of *K* for trifluoroacetic acid with density along different isotherms in carbon dioxide solvent. 66
- Figure 2-10 Acid Dimers: a) Formic Acid Dimer, b) Propionic Acid Dimer, c) Trifluoroacetic Acid Dimer (cyclic), d) Trifluoroacetic Acid Dimer (linear). 67
- Figure 2-11 Optimized structures of Acid Dimers in the presence of CO<sub>2</sub>. a) Formic Acid Dimer, b) Propionic Acid Dimer, c) Trifluoroacetic Acid Dimer (cyclic). 68
- Figure 2-12 Optimized structures of Acid Dimers in the presence of Ethane. a) Formic Acid Dimer, b) Propionic Acid Dimer, c) Trifluoroacetic Acid Dimer (cyclic). 69
- Figure 3-1 PEEK NMR cell used in the NMR investigations of CO<sub>2</sub> interactions with carboxylic acids. The tan part is the

	PEEK cell body, and the black part is the carbon-reinforced PEEK cap.	76
Figure 3-2	Ethane $^1\text{H}$ chemical shift as a function of $\text{CO}_2$ density at 295 K.	77
Figure 3-3	The aldehyde $^1\text{H}$ chemical shift of formic acid relative to ethane as a function of $\text{CO}_2$ density at 295 K.	78
Figure 3-4	The acid $^1\text{H}$ chemical shift of formic acid relative to ethane as a function of $\text{CO}_2$ density at 295 K.	79
Figure 3-5	The aldehyde $^1\text{H}$ chemical shift of formic acid relative to ethane as a function of $\text{CO}_2$ density at 323 K.	80
Figure 3-6	The acid $^1\text{H}$ chemical shift of formic acid relative to ethane as a function of $\text{CO}_2$ density at 323 K.	81
Figure 4-1	SAS apparatus and imaging equipment used in precipitation experiments. JG is the Jerguson guage high pressure view cell.	104
Figure 4-2	Still images of the injection of pure liquid solvents, acetone and methylene chloride, into supercritical $\text{CO}_2$ at various times and positions.	105
Figure 4-3	Still images of the injection of 1 wt% PLA solution in methylene chloride into supercritical $\text{CO}_2$ at various times and positions using three different magnifications.	106

Figure 4-4	Still images of the injection of a saturated PLA in methylene chloride solution at various times and positions using two different magnifications.	107
Figure 4-5	Still images of the injection of 1 wt% budesonide in methylene chloride solution at various times and positions using two different magnifications.	108
Figure 4-6	Still images at three different times at the nozzle showing the injection development for a 1 wt% solution of PLA injected into supercritical CO <sub>2</sub> .	109
Figure 4-7	Still images at three different times at position 4 showing the development of droplets and particles observed with time.	110
Figure 5-1	Ring-opening reaction between water and caprolactam.	131
Figure 5-2	Experimental apparatus used in the polymerization reactions during the supercritical antisolvent precipitation process. P1 is the pump used for introducing carbon dioxide, CO <sub>2</sub> , to the reaction vessel, R. P2 is the pump used to inject a liquid solution containing the monomer to be polymerized.	132
Figure 5-3	Scanning electron microscopy images of Nylon 6 polymerized during the supercritical antisolvent precipitation process. The first two images are magnified 200 times and show both particulate and fiber-like Nylon 6.	

	The image on the right is magnified 2000 times showing fibers in more detail.	133
Figure 5-4	Scanning electron microscopy images of Nylon 6 polymerized with TiO <sub>2</sub> during the supercritical antisolvent precipitation process. The image on the left is magnified 500 times, the image in the center is magnified 3k, and the image on the right is magnified 30k.	134
Figure 5-5	Fourier transform infrared transform spectra of pure caprolactam (red), pure Nylon 6 (dark blue), and the caprolactam reaction product (light blue).	135
Figure 5-6	Differential scanning calorimetry scans of pure Nylon 6 (green), the caprolactam reaction product (blue), and pure caprolactam (brown).	136
Figure 5-7	Scanning electron microscopy images of polymethacrylic acid polymerized during the supercritical antisolvent precipitation process with enhanced mass transfer. From left to right, the images are magnified 50, 500, and 2000 times.	137
Figure 5-8	Scanning electron microscopy images of polymethacrylic acid polymerized during the supercritical antisolvent precipitation process with enhanced mass transfer. From left to right, the images are magnified 5k, 50k, and 60 times.	138

Figure 5-9	Illustration of caprolactam transport in the SAS process. $n_A$ represents the flux of caprolactam, $A$ . $\rho_{A2}$ is the concentration of caprolactam in the methylene chloride, MC, phase. $\rho_{A4}$ is the concentration of caprolactam in the $CO_2$ bulk.	139
Figure 6-1	Schematic diagram of the setup used to concentrate the silver particles dispersed in a hexane/ $CO_2$ mixture (10% hexane by volume). A represents an ISCO 260D syringe pump, B represents a 6-port injection valve, C represents a high-pressure needle valve, D represents a variable volume high-pressure UV-vis vessel with 3 quartz windows, E represents a movable piston, F represents a high-pressure hand-operated syringe pump, G represents a high-pressure needle valve, and H represents a collection vessel. The yellow portion in the bottom of the collection vessel is hexane chilled by ice water.	160
Figure 6-2	Molecular structure of iso-stearic acid. $M_n=284$ g/mol.	161
Figure 6-3	Phase Behavior of Iso-Stearic Acid/ $CO_2$ Mixture at 295 K. No data was collected for the small VL1 two phase region at the $CO_2$ -rich end of the diagram.	162
Figure 6-4	TEM image of iso-stearic acid coated silver particles precipitated from a hexane dispersion.	163

Figure 6-5	Particle size distribution of the iso-stearic acid coated silver nanoparticles.	164
Figure 6-6	ATR-FTIR spectrum of iso-stearic acid coated silver nanoparticles.	165
Figure 6-7	UV-vis spectrum of iso-stearic acid coated silver particles dispersed in a hexane-CO <sub>2</sub> mixture (11% hexane by volume) at 276 bar and 295 K. This spectrum was collected 4 hours after the introduction of CO <sub>2</sub> solvent and is baseline corrected.	166
Figure 6-8	UV-vis spectrum of iso-stearic acid coated silver particles recovered from a hexane-CO <sub>2</sub> mixture (10% hexane by volume) at 276 bar and 295 K in hexane.	167
Figure 6-9	TEM image of iso-stearic acid coated silver particles recovered from a hexane-CO <sub>2</sub> mixture (10% hexane by volume) at 276 bar and 295 K in hexane.	168
Figure 6-10	UV-vis spectrum of silver particles dispersed off of a quartz surface in CO <sub>2</sub> at 276 bar and 295 K. This spectrum is taken after 17 hours and has been baseline corrected.	169
Figure 6-11	TEM image of iso-stearic acid coated silver particles recovered from CO <sub>2</sub> at 276 bar and 295 K in hexane.	170
Figure 6-12	Molecular structure of Ag-AOT-TMH (Fan et al. 2005).	171
Figure 6-13	Phase behavior of AOT-TMH and Ag-AOT-TMH at 40 °C (Fan et al. 2005).	172

- Figure 6-14 Uv-vis spectra of silver nanoparticles formed in CO<sub>2</sub> with 10% cyclohexane co-solvent at 295 K and 276 bar. The spectra have been scaled to have an absorbance of 0 at 700 nm for comparison. The dotted line corresponds to the initial absorbance, the dashed line to the absorbance after 24 hours, and the solid line to the absorbance after 5 days. 173
- Figure 6-15 TEM image of silver nanoparticles collected from a 10% cyclohexane in CO<sub>2</sub> mixture at 295 K and 276 bar. These particles were collected by directly spraying the contents of the vessel onto the TEM grid by depressurization. 174
- Figure 6-16 UV-vis absorbance spectrum of silver nanoparticles synthesized in neat CO<sub>2</sub> collected after 3 days. 175
- Figure 6-17 TEM image of silver nanoparticles collected from pure CO<sub>2</sub> at 295 K and 276 bar. These particles were collected by directly spraying the contents of the vessel onto the TEM grid by depressurization. 176
- Figure 6-18 UV-vis absorbance spectra of nanoparticles synthesized in CO<sub>2</sub> at 295 K and 276 bar. The dotted line corresponds to 10% cyclohexane co-solvent by volume, the dashed line to 2% cyclohexane co-solvent by volume, and the solid line no added cosolvent. 177
- Figure 6-19 UV-vis absorbance spectra for silver nanoparticles dispersed in CO<sub>2</sub> at 295 K with 10% cyclohexane co-

solvent by volume. Each curve corresponds to a different pressure going from the bottom curve (106 bar) to the top curve (276 bar).

178

## LIST OF TABLES

Table 2-1	LFHB scaling parameters for pure fluids. (Gupta, Combes et al. 1993)	54
Table 2-2	LFHB parameters for carboxylic acid self-association.	55
Table 2-3	Comparison of estimated free energy change upon hydrogen-bonding in different systems.	56
Table 2-4	Dimerization energies for carboxylic acids in gas phase, CO <sub>2</sub> , and ethane using different basis sets.	57
Table 4-1	of experimental conditions used in the SAS visualization experiments.	111
Table 4-2	Droplet size distributions ( $\mu\text{m}$ ) for 1% PLA in methylene chloride at 4.5 sec at various positions.	112

# CHAPTER 1

## INTRODUCTION

### **Introduction**

Supercritical fluids have many characteristics that make them desirable for use as solvents. Some of these characteristics are that the density, diffusivities, solubility parameter, heat transfer coefficients, and mass transfer coefficients, can be varied from those of the liquid phase to that of the vapor phase continuously (Bleich et al., 1994; Bukur et al., 1997; Dixon et al., 1993; Huang and Roberts, 2003; Hyatt, 1984; Kazarian et al., 1993; McHugh and Krukoni, 1994; McLeod et al., 2003; O'Shea et al., 1991; Randolph et al., 1993; Shekunov et al., 2001). The ability of the thermophysical properties of a supercritical fluid to be tuned with simple adjustments in temperature and pressure provides opportunities for these fluids to be employed in a number of processes.

As an example, one of the many applications of supercritical CO<sub>2</sub> involves the production of fine particles via spray techniques and this will be discussed in detail in a subsequent chapter. A number of related particle production techniques have been developed with slight variations in the operating procedures including aerosol solvent extraction system (ASES) (Bleich et al., 1994), gas antisolvent precipitation (GAS) (Randolph et al., 1993), precipitation with a compressed fluid antisolvent (PCA) (Dixon

et al., 1993; Lengsfeld et al., 2000; Mawson et al., 1997), supercritical antisolvent (SAS) (Yeo et al., 1993) process, and solution-enhanced dispersion by supercritical fluids (SEDS) (Shekunov et al., 2001). What all of these processes have in common is that a solution containing a dissolved species (solute) is mixed with a compressed, sometimes supercritical, fluid such as CO<sub>2</sub> which serves as an antisolvent. Upon mixing, the solvent is dissolved by the compressed fluid, in which the solute species is insoluble and therefore precipitates from solution. Molecular interactions between compressed CO<sub>2</sub> and the various species in these processes play a key role in the performance and therefore design of such processes.

Another method to take advantage of the adjustable properties of supercritical fluids is to use them as a reaction solvent. Ellington et al. (Ellington et al., 1994) measured the observed rate constants for the esterification reaction of phthalic anhydride with methanol carried out in supercritical CO<sub>2</sub>. They observed a dramatic enhancement of the rate constant near the critical pressure for CO<sub>2</sub> as compared to the rate constant at higher pressures. They attributed this enhancement to higher local concentrations, or solute clustering, of methanol near the dissolved phthalic anhydride. Hou et al. (Hou et al., 2001) used this idea of clustering for the esterification reaction of ethanol and acetic acid. They observed that the reaction rate increased dramatically near the critical pressure for the mixture over the observed rate constants at higher or lower pressures.

A specific class of reaction that has benefited from the tunable properties of supercritical fluids is polymerization reactions. Lousenberg and Shoichet (Lousenberg and Shoichet, 2000) produced linear poly(TFE-*co*-VAc) molecules in supercritical carbon dioxide. The properties of carbon dioxide suppressed the abstraction reaction, which

reduced branching and resulted in the linear polymer. Baradie and Shoichet (Baradie and Shoichet, 2002) showed that these polymers could be synthesized without the use of surfactant in CO<sub>2</sub> and have a relatively narrow size distribution. Baradie and Shoichet (Baradie and Shoichet, 2003) also showed that the surface of the polymers had a higher concentration of fluorine than the bulk because of the interactions between CO<sub>2</sub> and fluorocarbons. Owens et al. (Owens et al., 2002) combined the SAS process with polymerization in supercritical CO<sub>2</sub> to form polymer particles with size and morphology that can be adjusted by changing the processing conditions. Because the polymers are made in the SAS process, solvent extraction does not require any extra processing steps.

### **Solvent Nature of CO<sub>2</sub>**

Molecular interactions play a critical role in processes involving CO<sub>2</sub>. This dissertation will examine the interactions between CO<sub>2</sub> and the carboxylic acid functional group by Fourier transform infrared spectroscopy and nuclear magnetic resonance spectroscopy. These interactions are then used in a novel polymerization technique involving methacrylic acid. Imaging of the SAS process is also performed to give insight into how the interactions between CO<sub>2</sub> and certain organic solvents impact the process. This process is then combined with the ability of CO<sub>2</sub> to interact with amines in a new method for the production of Nylon 6. The ability of CO<sub>2</sub> to solvate branched, methylated tails of a carboxylic acid ligand allows CO<sub>2</sub> to stably disperse silver nanoparticles without fluorinated compounds. In all cases, the interactions of CO<sub>2</sub> are of primary importance.

Carbon Dioxide has long been a desirable solvent to use because of its highly tunable thermophysical properties, its non-toxic and non-flammable nature, its

inexpensiveness, and its environmentally benign nature. However, to use CO<sub>2</sub> as a process solvent, the materials you wish to dissolve must be soluble in it. Unfortunately, CO<sub>2</sub> is a poor solvent and does not dissolve most species. In order to make use of CO<sub>2</sub>, the interactions of CO<sub>2</sub> with those molecules that it does dissolve have been the subject of investigations for some time now. If the way CO<sub>2</sub> interacts with other molecules can be fully understood, then processes that could benefit from using CO<sub>2</sub> as a solvent could be better developed, particularly if these specific interactions could be exploited for design of separation, precipitation, and reaction processes.

Fluorinated compounds have been shown to exhibit much higher solubility in CO<sub>2</sub> than their hydrocarbon analogs (DeSimone et al., 1992). As an example, hydrocarbon-chain surfactants are relatively insoluble in CO<sub>2</sub>, but substituting fluorine atoms into the backbone can significantly enhance their solubility in CO<sub>2</sub> (Adamsky and Beckman, 1994). While substituting fluorine atoms can increase the solubility, these compounds are both environmentally persistent and expensive. Since two of the primary reasons for using CO<sub>2</sub> as a process solvent is its environmentally benign nature and its low cost, these aspects present significant drawbacks to their use in many processing applications. For these reasons, understanding interactions with different functional groups is essential to designing new molecules that may be soluble in CO<sub>2</sub>.

Interestingly, CO<sub>2</sub> has been proposed to participate in Lewis Acid-base interactions. Some of the work dealing with this type of interaction is discussed here. As far back as the mid 1980's, the ability of high-pressure liquid and supercritical CO<sub>2</sub> to participate in Lewis acid-base interactions was studied. Hyatt examined the polarizability of CO<sub>2</sub> by using several different polarity probes (Hyatt, 1984). He concluded that CO<sub>2</sub>

acted much the same as a solvent as did a hydrocarbon such as hexane, except that in some instances CO<sub>2</sub> could act as a very weak base. This pioneering work caused many people to design processes assuming CO<sub>2</sub> behaves like hexane, but, unfortunately, the solubility of hexane-soluble compounds can be significantly lower in dense CO<sub>2</sub>.

Sigman and co-workers (Sigman et al., 1985) measured  $\pi^*$  and  $\beta$  parameters by using many different solvatochromic indicators. These parameters give an indication of a solvent's ability to participate in specific interactions. These parameters indicated that CO<sub>2</sub> could act as a Lewis acid, but not as a Lewis base.

Phillips and Robey (Phillips and Robey, 1989) used non-polar chromatography to examine more definitively the differences between hexane and supercritical CO<sub>2</sub> as solvents. Unlike the very small ability of CO<sub>2</sub> to act as a Lewis base as observed by Hyatt (Hyatt, 1984), Phillips and Robey found that the ability of CO<sub>2</sub> to act as a Lewis base makes it a very different solvent from hexane, contrary to the prevailing opinion at the time.

Keith Johnston's group (O'Shea et al., 1991) used the equilibrium of 4-(Phenylazo)-1-naphthol to probe the ability of several solvents to act as a Lewis acid or Lewis base. They concluded that CO<sub>2</sub> acted as a Lewis acid because the more polar form of the tautomer was preferred in CO<sub>2</sub>. This conclusion resulted in a large amount of work designing molecules that would be soluble in CO<sub>2</sub> by incorporating Lewis base groups.

The group of Enick and Beckman (Hoeftling et al., 1993; Hoeftling et al., 1991; Potluri et al., 2002; Sarbu et al., 2000a; Sarbu et al., 2000b) sought to find compounds that would be soluble in CO<sub>2</sub> in the hopes of creating non-fluorinated compounds capable of acting as surfactants in order to make use of microemulsions in a solvent as desirable

to use as CO<sub>2</sub>. Under the assumption that CO<sub>2</sub> can act as a Lewis acid, they designed polymers with Lewis base functional groups in the chain to serve as model surfactants for CO<sub>2</sub>. While great strides have been made in improving solubility by incorporating Lewis base groups, the pressure required to make many of their compounds soluble is very high (greater than 200 psi for 1 wt% poly(epichlorohydrin) functionalized with 28% acetate groups with only 7 repeat units). Nonetheless, since fluorinated compounds are both very expensive and environmentally unfriendly, their work to design non-fluorinated compounds that are both soluble and capable of acting as surfactants in CO<sub>2</sub> has been of critical importance.

Johnston's group continued to look for more verification that CO<sub>2</sub> was capable of acting as a Lewis acid as a solvent. Meredith and co-workers (Meredith et al., 1996) looked at the  $\nu_2$  bending mode of CO<sub>2</sub> in the presence of three different Lewis bases using Fourier transform infrared (FTIR) spectroscopy. Although they observed only very weak interactions between CO<sub>2</sub> and some relatively strong Lewis bases, the strength of the interactions, as measured by equilibrium constant, increased with the strength of the Lewis base. This provided direct evidence that CO<sub>2</sub> was capable of acting as a Lewis acid.

Yamamoto and co-workers (Yamamoto et al., 1999) also used FTIR spectroscopy to probe the acid-base nature of CO<sub>2</sub>. They looked at the C=O stretching band for acetic acid and palmitic acid. By measuring the dimerization constant for these acids, they were able to probe the ability of CO<sub>2</sub> to interact with these molecules. They observed that as the pressure, or density, of CO<sub>2</sub> was increased, the equilibrium constant for the acids decreased. They explained this as a result of a competing interaction between the acid

interacting with itself and the weaker interaction of CO<sub>2</sub> interacting with the monomer. As the density of CO<sub>2</sub> is increased, then by LeChatlier's principle, the equilibrium has to shift toward more interaction between CO<sub>2</sub> and the acid, thereby reducing the interactions of the acid with itself. They attribute this to interactions of CO<sub>2</sub> with the basic carbonyl group of the acid, implicating that CO<sub>2</sub> acts as a Lewis acid.

Similar work with formic acid has also been performed by Park and co-workers (Park et al., 2002). The same trends were observed for formic acid as had been observed for acetic acid and palmitic acid. They formalize the density dependence of the equilibrium constant for dimerization by using the Modified Lattice Fluid Hydrogen-Bonding (MLFHB) theory. They also conclude that the interaction of the acid with the CO<sub>2</sub> is with the basic carbonyl oxygen. Though these conclusions by both groups would presume that CO<sub>2</sub> acts as a Lewis acid, the experimental evidence is not definitive and does not preclude the possibility that CO<sub>2</sub> could alternatively act as a Lewis base since the acids contain both an acid and a base functionality.

Recently, experimental evidence has shown that CO<sub>2</sub> is capable of acting as a Lewis base in the presence of Lewis acids. Melikova et al. (Melikova et al., 2002) used FTIR spectroscopy and *ab initio* calculations to study the interactions of fluoroform with liquid argon, nitrogen, carbon monoxide, and carbon dioxide. All of these molecules were shown to interact weakly with the acidic proton of fluoroform both by experiments and calculations. This interaction they showed to be between the hydrogen and the free electrons on each of the liquid molecules. The interaction with CO<sub>2</sub> was the strongest of the ones observed giving evidence as to the ability of CO<sub>2</sub> to act as a Lewis base.

The ability of CO<sub>2</sub> to act as a Lewis base was further examined by Hampe and Rudkevich (Hampe and Rudkevich, 2002). They used UV-vis, fluorescence, and NMR spectroscopy to examine the interaction of CO<sub>2</sub> with fluorescently active amines. Their results showed that the CO<sub>2</sub> interacted with the acidic amine proton strongly enough to react to form carbamic acids. These could then further react to form carbamate salts. These reactions are all reversible, but the importance is that CO<sub>2</sub> was once again shown to interact as a Lewis base with a Lewis acid.

Further evidence of this ability of CO<sub>2</sub> to act as a Lewis base was given by Fujii and co-workers (Fujii et al., 2002). They used advanced spectroscopic techniques to examine phenol-carbon monoxide clusters and phenol-carbon dioxide clusters. They looked at the OH stretching vibration for these clusters by using the infrared-ultraviolet double resonance technique. They also looked at the OH stretching vibration for the cationic ground state of the cluster by using infrared photodissociation spectroscopy. Both of these techniques showed that CO and CO<sub>2</sub> both acted as Lewis bases in these clusters. By comparing the shifts of these peaks with the shifts of phenol-argon and phenol-nitrogen clusters, they showed that the strength of the interaction was positively related to the proton affinity for each of the molecules acting as a base.

Raveendran and Wallen (Raveendran and Wallen, 2002) have performed *ab initio* calculations on systems of CO<sub>2</sub> and Lewis base containing compounds, including carboxylic acids. Unlike the previous studies, which generally concluded that CO<sub>2</sub> either acted as a Lewis acid or as a Lewis base, their calculations showed that the optimum state was for the CO<sub>2</sub> to interact in a Lewis acid manner with a Lewis base, a carbonyl oxygen, and simultaneously in a Lewis base manner with the slightly acidic proton of the  $\alpha$

carbon. This would create a ring-like structure with CO<sub>2</sub> acting as both a Lewis acid and a Lewis base in a cooperative manner to increase solubility. Wallen and co-workers then used a variety of spectroscopic techniques to give experimental support to their calculations (Blatchford et al., 2002, 2003). Their Raman, IR, and NMR spectroscopy results for acetaldehyde and methyl acetate all supported their calculations. These findings have caused a significant change in thought with regards to designing CO<sub>2</sub> soluble compounds, which may be very beneficial.

Raveendran and Wallen looked at the ability of CO<sub>2</sub> to act as either a Lewis acid or a Lewis base by performing *ab initio* calculations on the interactions between CO<sub>2</sub> and fluorinated methane molecules (Raveendran and Wallen, 2003b). They calculated the interaction energies between one CO<sub>2</sub> molecule and one methane molecule with 0, 1, 2, 3, or 4 fluorines. They found that there was no significant interaction energy difference between methane and perfluoromethane in CO<sub>2</sub>. They found that as the number of fluorine atoms changed, the partial charges on all of the atoms, including the hydrogen atoms changed. This resulted in the observation of a maximum interaction energy as a function of fluorine substitution. Their calculations showed that the CO<sub>2</sub> not only interacted with the fluorine atoms, but it also interacted with the slightly positively charged hydrogen atoms. They concluded from these findings that CO<sub>2</sub> was capable of acting as either a Lewis acid or a Lewis base.

Carboxylic acids can also be used to probe solvent interactions. Because the self-association, or in the dilute case, dimerization of these acids is an equilibrium that can be significantly affected by the choice of solvent, measurement of this equilibrium constant gives an indication of the strength of interactions between the acid group and the solvent.

FTIR spectroscopy has long been a very useful tool to examine the interactions of systems at a molecular level. Specifically, FTIR has been used to look both at interactions of solvent with solute and solute with solute. The following will detail some of the major FTIR work as it pertains to carboxylic acid dimerization, carbon dioxide as solvent, and supercritical solvents in general.

Murty and Pitzer examined the dimerization of trifluoroacetic acid (TFA), acetic acid, pentafluoropropionic acid (PFP), heptafluorobutyric acid (HFB), and pentafluorobenzoic acid (PFB) in various solvents using IR spectroscopy (Murty, 1971; Murty and Pitzer, 1969). In order to study the effect of solvent on the dimerization of the acid, they looked at the stretching bands for both the OH bond and the carbonyl bond of the acid. In all nonpolar solvents, the spectra showed evidence for only one type of dimer for each acid. However, in benzene, a slightly basic solvent, the perfluorinated acids, including TFA, showed three peaks, rather than two, in the carbonyl stretching region and two peaks, instead of one, in the free OH stretching region. They explained this as the result of the basic benzene solvent allowing the linear dimer to be stabilized as a result of the solvent interacting with the strongly acidic proton of the perfluorinated acids, like TFA. The third peak in the C=O stretching region was attributed to the linear dimer and the extra free O-H stretching peak also to the linear dimer. They both had shifts as the result of the interaction at the neighboring hydrogen bond on the same molecule.

In the same time period as Murty and Pitzer, Kirszenbaum and co-workers (Kirszenbaum et al., 1971) looked at the same dimerization of TFA in benzene using IR spectroscopy both in the O-H and C=O stretching regions of TFA. They did not observe the third peak for the C=O stretch or the second peak for the O-H stretch of TFA in

benzene. They argued that the results of Murty and Pitzer were incorrect as they did not compensate for the benzene solvent correctly. They instead claimed that TFA behaves like any other carboxylic acid and exists as an equilibrium between the monomer and cyclic dimer.

Christian and Stevens (Christian and Stevens, 1972) continued similar work with TFA. They quantified the equilibrium constants for the TFA dimerization, assuming only the cyclic dimer was formed, in several solvents. They found that the more reactive solvents interacted more strongly with the acid, thereby reducing the equilibrium constant. They also developed a method for determining the equilibrium constant for carboxylic acid dimerization in opaque solvents.

Hyatt (Hyatt, 1984) used IR spectroscopy in his work to characterize the solvent properties of CO<sub>2</sub>. By looking at the magnitude of the solvent shifts of target bonds in probe molecules, he compared the ability of CO<sub>2</sub> to act as a Lewis acid or Lewis base to other organic solvents. Based on his results, he concluded that CO<sub>2</sub> acts much like an alkane solvent in the presence of Lewis bases, but more like a basic solvent in the presence of a Lewis acid. This would suggest that molecules with Lewis acid groups would be more soluble in CO<sub>2</sub>.

Fujii and co-workers (Fujii et al., 1988) examined the dimerization of acetic acid in eight different solvents by looking at the carbonyl stretching band of the acid. They argued that the reason the dimerization constant of acetic acid decreased with increased concentration was the result of a competitive equilibrium with the linear dimer which was being neglected by the assumption that the acid existed in a simple monomer-cyclic dimer equilibrium. They verified this hypothesis by increasing the concentration of the

acetic acid by two orders of magnitude until they observed the band corresponding to the linear dimer. When they accounted for all three peaks, the observed dimerization constant did not change with concentration, as would be expected.

Fulton and co-workers (Fulton et al., 1991) examined the hydrogen-bonding of methyl alcohol-d in supercritical CO<sub>2</sub> and ethane and liquid heptane. Their choice of solvents allowed them to differentiate between the effects of pressure and solvent strength. They observed that in both of the supercritical fluids, the natural logarithm of the equilibrium constants for the formation of the tetramer of the alcohol increased linearly with pressure. This effect was attributed to entropic effects associated with compression which results in clustering of the dissolved species. However, the enthalpy associated with hydrogen-bonding in supercritical ethane was very similar to that of liquid heptane. The enthalpy in supercritical CO<sub>2</sub>, however, was significantly lower. This would suggest that the CO<sub>2</sub> solvent is capable of having some kind of weak interaction with the alcohol. They suggest that this is a quadrupole-dipole interaction.

This type of work was continued by Kazarian and co-workers (Kazarian et al., 1993) and Gupta and co-workers (Gupta et al., 1993). Kazarian and co-workers studied the hydrogen-bonding of perfluoro-*tert*-butyl alcohol (PFTB) and dimethyl ether (DME), while Gupta and co-workers looked at the hydrogen bonding between methanol and triethylamine, both in SF<sub>6</sub> from the gas-phase through the supercritical fluid state. They observed that as the solvent pressure, or density, was increased the equilibrium constant decreased as well. This is not inconsistent with the results of Fulton and co-workers (Fulton et al., 1991), who observed an increase in equilibrium constant with density. They explain this apparent discrepancy as a result of the standard free energy change of

dimerization for the alcohol being negative and that of the PTFB-DME bond being positive. They formalize the density dependence of the equilibrium constant with the modified lattice-fluid hydrogen bonding (MLFHB) model developed by Gupta and co-workers (Gupta et al., 1993; Gupta et al., 1992). In this model, the natural logarithm of the equilibrium constant is proportional to the negative of the product of the density and the standard free energy change of dimerization. So, the slope of the natural logarithm of the equilibrium constant with density then will switch sign if the standard free energy change of dimerization switches sign. This model gave a basis for understanding the density effects supercritical fluids have on dimerization.

Keith Johnston and co-workers (Clarke et al., 1997; Johnston et al., 1996) used FTIR spectroscopy to examine an even more complicated system in supercritical CO<sub>2</sub>. They wanted to use FTIR spectroscopy to show whether water partitioned into the core of reverse micelles formed in supercritical CO<sub>2</sub> or not. If a water phase could exist inside of a CO<sub>2</sub> phase, then many reactions that would normally take place in water could take place inside of a highly desirable solvent like CO<sub>2</sub>. They were able to observe three different absorptions due to water. One corresponded to water dissolved in the CO<sub>2</sub>, one to water bound to the head groups of the surfactants, and one to water in the core. The solvent shift associated with the water in the core was the same as that corresponding to free water. They observed that the absorbance for water in CO<sub>2</sub> increased as more water was added to the system until the solubility limit of water in CO<sub>2</sub> was reached. Further addition of water then saturated the surfactant head groups and then the bulk water peak increased while the others remained constant. This provided direct evidence for the formation of a pure water phase.

Meridith and co-workers (Meridith et al., 1996) used FTIR spectroscopy to measure the equilibrium constants between CO<sub>2</sub> and solutes containing Lewis bases in a quantitative manner. This work was different from previous work in that it tried to measure the CO<sub>2</sub> interaction directly. In order to measure this, they measured the  $\nu_2$  bending mode for carbon dioxide in the presence of three strong Lewis bases: triethylamine (TEA), pyridine (PYR), and tributyl phosphate (TBP). They dissolved both the CO<sub>2</sub> and the Lewis bases in pentane solvent. The equilibrium constants were determined for all three systems. The equilibrium constants were all relatively small for acid-base interactions, as were the enthalpies associated with the interaction. The enthalpy of interaction for the CO<sub>2</sub>-TBP complex was the largest at -4.7kcal/mol. While this is much smaller than that of a typical hydrogen bond, it is not negligible. The fact that TBP was the strongest base and had the largest interaction with CO<sub>2</sub> provides evidence that CO<sub>2</sub> can act as a Lewis acid.

Lu and co-workers (Lu et al., 1998) returned to the examination of carboxylic acids by studying lauric acid. They looked at the carbonyl stretching region of CO<sub>2</sub> and determined the equilibrium constants based on the areas of the peaks corresponding to the lauric acid monomer and dimer. They observed that as the solvent density is increased, the natural logarithm of the dimerization constant decreases linearly. They explained this trend as the result of solute clustering. As the density of the solvent was increased, the amount of clustering would decrease, thus decreasing the effective concentration and the apparent equilibrium constant.

Yamamoto and co-workers (Yamamoto et al., 1999) examined the dimerization of acetic acid and palmitic acid in CO<sub>2</sub> using FTIR spectroscopy to measure the C=O

stretching frequency of the acid. The behavior of these acids in pure CO<sub>2</sub> was similar to that observed by previous groups with the natural logarithm of the equilibrium constants for the acids decreasing with CO<sub>2</sub> density. They also explore the ability of ethanol to act as a co-solvent for supercritical CO<sub>2</sub> by measuring the extent of interaction between carboxylic acids and ethanol in CO<sub>2</sub> by measuring the carbonyl stretching frequency for the acids. They observe that as the concentration of ethanol is increased, the interaction between the acid and the ethanol increases. This provides evidence for the ability of ethanol to increase the solubility of some molecules in CO<sub>2</sub>.

Park and co-workers (Park et al., 2002), as previously discussed, continued the work on carboxylic acid dimerization in supercritical CO<sub>2</sub> by studying formic acid. While they observed the same trends of a decrease in dimerization constant with increased solvent density, they modeled this trend using the MLFHB model in the same manner as had earlier groups (Gupta et al., 1993; Kazarian et al., 1993) for hydrogen-bonding in a supercritical fluid solvent. By using this model and comparing the magnitude of the density dependence to that of formic acid in ethane, they were able to obtain a measure of the strength of interaction between CO<sub>2</sub> and formic acid.

### **Nuclear Magnetic Resonance Studies**

Nuclear Magnetic Resonance (NMR) spectroscopy is an extremely useful tool in chemistry and physics because of its ability to give detailed information about systems on an atom by atom basis. The ability of NMR to probe the electron density around specific atoms makes it an excellent means for probing both inter-molecular and intra-molecular interactions. This makes NMR an excellent choice for examining molecular interactions

in CO<sub>2</sub> on an atom-specific basis. In order to use such techniques to study systems under high pressure, such as systems under supercritical conditions, modifications to the NMR cell are required. While relatively few research groups have employed high-pressure NMR techniques, efforts to do so have been around for quite some time. Some of the major contributions are discussed here.

Previous work in this field has employed a variety of different methods to obtain a non-magnetic, high-pressure cell usable in an NMR. The first designs appeared in the literature in the early 1970's. These designs, by Tison and Hunt (Tison and Hunt, 1971) and by Yamada and co-workers (Yamada, 1974; Yamada et al., 1991), used capillary tubing which would be filled at a very cold temperature and then sealed. As the temperature would rise, so would the pressure in the glass cell. In the design of Tison and Hunt, the capillary is blown into two bulbs of similar volume and then filled. The design of Yamada, however, took standard pyrex tubing and drew it out to form capillaries on either end of the cell. This would allow for both filling and removal of the sample through a small volume, leaving the majority of the volume in the useful field in the NMR. These designs have drawbacks, however, in that the pressure control is very poor and there is a large risk of breakage in the capillary which could potentially be damaging to the NMR.

Another design was to use a single crystal sapphire tube (Bai et al., 1996; Horvath and Ponce, 1991; Roe, 1985). The first design of this kind that was usable in a commercial NMR was that of Roe (Roe, 1985) where he used a single sapphire tube and a relatively complicated nonmagnetic Ti-alloy valve assembly. This design was modified by Horvath and Ponce (Horvath and Ponce, 1991). They greatly simplified the titanium

valve assembly which allowed the cell to be constructed much more simply. A large improvement to the design was by Bai and coworkers (Bai et al., 1996). This design added a movable piston inside the cell and a pressure control device. This allowed the pressure in the cell to be controlled even after being filled. Their design also had more of the fluid in the detection coil region, which aided in spin relaxation studies. This is important for diffusion studies as well. The sapphire crystal approach is very attractive because it is now commercially available and has a relatively low risk of burst under pressure. The drawback of the sapphire crystal cell is that it is fairly expensive because of the sapphire.

High-pressure cell designs, led by Jiri Jonas, focused on using non-magnetic metals for use in the cell (Ballard et al., 1996; Ballard et al., 1998; Hoffmann and Conradi, 1997a, b, 1998; Jonas et al., 1998; Jonas et al., 1993). These high-pressure cells were not usable without additional modifications to the NMR probe and putting both the cell and probe inside a high-pressure vessel, making them somewhat less desirable. After some early work with some other non-magnetic metals (beryllium copper and stainless steel), all of the work discussed used titanium alloys as the major component of the cell body. Jonas and co-workers (Jonas et al., 1993) constructed cells, probes and radio-frequency (rf) feedthroughs for both a 180 MHz NMR and a 300 MHz NMR. While the cell was mostly made of titanium, other nonmagnetic materials, beryllium copper, and stainless steel were used in the seals. Teflon and Aluminum were also used in the 300 MHz cell. Ballard and co-workers (Ballard et al., 1996) improved the design for the 300 MHz NMR. They made several important changes including adding a thermocouple inside the cell for better temperature control, replacing the aluminum and Teflon spacers

with a beryllium copper plug to accommodate the thermocouple, changing the Bridgman seal to a C-seal flange to reduce the chance of leakage, changing the rf feedthrough to give it a better lifetime under pressure, and changing the probe to incorporate the new rf feedthrough. Hoffmann and Conradi (Hoffmann and Conradi, 1997a, 1998) modified the design to make it simpler and less expensive for a 186.6 MHz NMR. They used rubber O-rings for seals rather than the expensive specially machined seals and used an internal piston pressurized by argon gas, which both makes the pressure generation equipment simpler and decreases the risk of rupture. Ballard and co-workers (Ballard et al., 1998; Jonas et al., 1998) continued their high-pressure probe design to operate at higher resolution by constructing a cell and probe that could be operated at 500 MHz. While the major characteristics were the same as those for the 300 MHz probe, the RF sample coil was changed from a two-turn coil to a one-turn saddle coil with capacitors directly soldered on to the coil. This change increased the sensitivity of the probe drastically, by almost five times. These high-pressure nonmagnetic metal probe designs, while very reliable and able to withstand great pressures, are quite complex, including modifications to the NMR itself, and some of the materials required are quite expensive.

In the 1990's, the idea of using capillary tubing as a high-pressure NMR cell was revisited. Clem Yonker and co-workers (Pfund et al., 1994; Wallen et al., 1996; Yonker et al., 1998a; Yonker et al., 1998b; Yonker et al., 1995) developed a reliable, yet inexpensive cell design capable of reaching very high pressures. This design, much like the first high-pressure NMR cells, used fused silica capillary tubing. The differences between this design and the first designs are that the cell would not be sealed, which allows for better pressure control, and that the tubing would not be blown to make bulbs,

which would greatly decrease the chance of introducing a weak point capable of resulting in a catastrophic failure. In order to allow for a large enough volume of fluid in the region of the rf coil, the capillary tubing was bent over and over to make a series of loops which could fit inside of a standard NMR tube. The bends in the loop were then coated to help prevent weak points from forming in the bends. While this type of cell is very inexpensive and relatively safe, the bending of the tubes with a flame can be quite a difficult process.

Wallen and co-workers (Wallen et al., 2000) first presented a cell that was made out of poly(etherether ketone) (PEEK), a machinable, very high-tensile strength polymer capable of withstanding very high pressures (up to 400 bar). This cell had a three-piece design which employed an O-ring for sealing. This design was improved by Yonker (Yonker and Linehan, 2002) and Linehan and slightly modified by Tai and coworkers (Tai et al., 2002). The major changes from the initial design of Wallen was to switch the cell body from a three-piece design to a two-piece design, to replace the PEEK cap with a carbon-reinforced PEEK cap, and to replace the O-ring with a cone and taper high-pressure seal. The result of these changes was to simplify the design and make the cell much less likely to leak under pressure. This design is very practical because it is affordable, easily machined, able to withstand large pressures with little risk of leakage, and capable of being used in a commercial NMR without any modification to the instrument or to the probe.

High-pressure has recently been used to investigate interactions between solute and solvent in sub- and supercritical CO<sub>2</sub>. Dardin et al. (Dardin et al., 1998) used the high-pressure cell described by Yonker and co-workers (Pfund et al., 1994; Wallen et al.,

1996; Yonker et al., 1998a; Yonker et al., 1998b; Yonker et al., 1995) to observe the  $^1\text{H}$  and  $^{19}\text{F}$  chemical shifts of fluorocarbons dissolved in supercritical  $\text{CO}_2$ . They used the fact that the chemical shift is a direct indication of the local chemical environment resulting from local electric field effects on the local magnetic field (Jameson, 1991). The chemical shift has been shown to be well approximated by a linear function of solvent density for the density range covered by  $\text{CO}_2$ . For  $\text{CO}_2$ , the slope of this relation has been shown to be the sum of the bulk magnetic susceptibility and any solvent-solute interactions (Lim et al., 1993). They found that for *n*-hexane, the proton shifts were linear in density, implying they had no specific interactions with  $\text{CO}_2$ . When they looked at perfluoro-*n*-hexane, the fluorine nuclei shifts were far from linear, which they attributed to van der Waals forces between the fluorine atoms and  $\text{CO}_2$ . They also looked at the shifts for an ester with a hydrocarbon chain and a perfluorinated chain. For this molecule, they observed that there was a linear dependence on density for the protons while there was a nonlinear dependence for the fluorine nuclei. They used this information to conclude that there were specific interactions between  $\text{CO}_2$  and fluorine and that these interactions depended on the surface area of the site.

Clem Yonker further examined this interaction between fluorine nuclei and  $\text{CO}_2$ . He used relaxation time data for  $^{19}\text{F}$ ,  $^1\text{H}$ , and  $^2\text{H}$  for perfluorobenzene, benzene, and perdeuterobenzene, respectively, to examine whether any specific solvent-solute interactions exist for these molecules (Yonker, 2000). He examined each of these molecules in solution over a wide range of both temperature and pressure. He observed that at high densities, the relaxation rates for both the protons on benzene and fluorine nuclei on perfluorobenzene converged. He states that this indicates a general interaction

of both compounds with CO<sub>2</sub>, such as quadrupole - quadrupole interactions, but that there are no specific interactions of CO<sub>2</sub> with any nuclei. He also shows that at low temperatures, the relaxation times for the nuclei in CO<sub>2</sub> converge with the relaxation times for the nuclei in their pure liquid state, as would be expected in the absence of specific interactions.

Yonker and Palmer (Yonker and Palmer, 2001) continued to examine CO<sub>2</sub> interactions with fluorine by looking at the effects of nuclear shielding on chemical shifts of <sup>1</sup>H and <sup>19</sup>F nuclei of fluoromethane and trifluoromethane dissolved in CO<sub>2</sub>. They used the same kind of NMR tube and method as Dardin et al. (Dardin et al., 1998). They looked at low-pressure (less than 800 psi) CO<sub>2</sub> solutions. There was no variation of the chemical shifts for the fluorine atoms from the linear relationship with density expected resulting from the change in bulk magnetic susceptibility of the solvent. They did notice that the slope of the density dependence for the proton in trifluoromethane deviated from that expected. They attributed the slight deviation to multibody interactions. They also observed that at high-densities, the fluorine chemical shifts of fluoromethane deviated from the linear extrapolation from the low-density results. They attributed this deviation to multi-body effects as well.

Kanakubo et al. (Kanakubo et al., 2002) examined the chemical shifts of <sup>19</sup>F of 2, 3, 4, 5, 6-pentafluorotoluene, chloropentafluorobenzene and perfluoro(methylcyclohexane) dissolved in CO<sub>2</sub>. Instead of trying to attribute any deviations from the linear dependence of the solvent shifts on density to specific interactions, they attributed the deviation to excess local solvent densities, relative to the bulk density. They found that for each of the compounds, the solvent shifts for all of the fluorine nuclei deviated

from the linear dependence expected. They all showed a bulk density that corresponded to a maximum local density. For the aromatic compounds, the maximum deviation occurred in the ortho- position while the smallest deviation was in the para- position. For the perfluoro(methyl-cyclohexane) molecule, they found that the fluorine nuclei in the equatorial position, the excess solvent shift was larger than in the axial position. Their results showed both that the excess solvent shift went through a maximum with respect to the bulk density and that the local solvent density was strongly dependent on the geometrical arrangement of the molecules.

Wallen and co-workers have recently used a combination of spectroscopic techniques to probe the existence of cooperative hydrogen bonds between the oxygen of CO<sub>2</sub> with a proton in close proximity to a Lewis base group interaction with the carbon of CO<sub>2</sub> (Blatchford et al., 2003). Specifically, they examined acetaldehyde and methyl acetate dissolved in supercritical CO<sub>2</sub> by using high-pressure NMR chemical shift data for the protons on the two compounds. They found that all of the protons shifted more as a function of density than the linear change expected due to changes in the bulk magnetic susceptibility, which they observed when dissolving the solutes in helium. They also observed that the shifts were larger than those due to van der Waals interaction by comparing the shifts to those in nitrogen. Most importantly, they observed that the shifts changed different amounts depending on the position of the proton, in accordance with the strength of the interaction with the CO<sub>2</sub> oxygen predicted by their *ab initio* calculations.

## **Supercritical Fluid Particle Formation Studies**

The types of studies described above provided information on a molecular level of interactions in supercritical CO<sub>2</sub>. These interactions have a direct impact on the solubility of various compounds in CO<sub>2</sub>. Supercritical fluids have gained much attention because of their usefulness in producing microparticles by a variety of processes. One of these processes is called the rapid expansion of supercritical solvent (RESS) precipitation process. In this process, a compound, such as a polymer, is dissolved in a dense supercritical solvent. Then, the solvent is rapidly depressurized by spraying through a nozzle, which greatly reduces the solubility of the dissolved compound, resulting in precipitation. However, very few polymeric or high molecular weight organic compounds have significant solubility in supercritical CO<sub>2</sub>. An alternative method to produce microparticles is to use supercritical CO<sub>2</sub> as an antisolvent. In either case, the role of interactions with CO<sub>2</sub> has direct impacts on the ability of these processes to form microparticles by adjusting the solvent strength.

The precipitation with a compressed fluid antisolvent (PCA) process involves the spraying of a liquid organic solvent containing the desired compound into dense CO<sub>2</sub> (Dixon et al., 1993).. If the dense CO<sub>2</sub> is in the supercritical phase, the process is known as the supercritical fluid antisolvent (SAS) precipitation process. An organic solvent, e. g. toluene, is chosen so that it has reasonable solubility in CO<sub>2</sub>, while a solute molecule, e. g. polystyrene, is essentially insoluble. As the solution is sprayed, mass transfer between the liquid phase and the supercritical phase results in a high level of supersaturation for the solute molecule. This results in the precipitation of the solute into microparticles. Due to the complexity of the process, multiple mechanisms have been

proposed to explain this process. Dixon et al. (Dixon et al., 1993) proposed that for dilute polymer concentrations, atomization of the jet, breaking up into very small droplets, occurs soon after the solution exits the capillary nozzle because of low interfacial forces. These droplets then become solvent-depleted as mass transfer with the CO<sub>2</sub> occurs leading to precipitation of the dissolved solute in the droplet either to a single microparticle or to multiple microparticles. They observed that as the CO<sub>2</sub> density was increased, smaller particles were produced. They explained this as a result of smaller droplets being formed because of higher inertial forces. For higher polymer solute concentrations, they observed fiber formation, which they explained as the result of increased jet stability by higher viscosity. The mass transfer necessary for supersaturation then occurs more rapidly than atomization, leading to the precipitation of fibers.

Soon after, Randolph et al. (Randolph et al., 1993) used the same process to produce poly(L-lactic acid) (PLA) particles by spraying them in a methylene chloride solution into supercritical CO<sub>2</sub>. They also observed the formation of polymer microspheres, but they observed an opposite trend in the behavior of particle size with CO<sub>2</sub> density as did Dixon et al. (Dixon et al., 1993). They point out that the organic solvents used are different, and that the diffusion coefficients for the two solvents would be much different. They propose that for their system, the nucleation rate is more important than the initial droplet size. They point out that the diffusion constant for CO<sub>2</sub> in methylene chloride is higher at lower pressures meaning that the droplets will swell more rapidly. This will cause supersaturation faster and allow less time for the growth at nucleation sites. This mechanism would still explain the previous results because the

time for growth of nucleation sites would be much longer for the smaller diffusion constant of CO<sub>2</sub> in toluene.

Werling and Debenedetti (Werling and Debenedetti, 1999, 2000) have performed numerical modeling of mass transfer in the SAS process. They have performed calculations in both mixture subcritical conditions (Werling and Debenedetti, 1999) and mixture supercritical conditions (Werling and Debenedetti, 2000). Their calculations neglect any droplet movement, which can affect diffusion, and the presence of any dissolved compound, which can greatly alter surface tension, which in turn affects initial droplet sizes. However, the calculations are still quite insightful as to this portion of the overall process. In the mixture subcritical conditions, both a supercritical phase and a distinct liquid phase are present. The calculations showed that for a toluene droplet, the droplets always swelled initially even though toluene was evaporating into the CO<sub>2</sub> phase as well as CO<sub>2</sub> dissolving in the toluene phase. Because diffusion constants depend on the solvent, this observation does not imply that all solvents would swell with CO<sub>2</sub>. Also, they showed that while larger initial droplet sizes do imply longer droplet lifetimes, that does not imply that the larger droplets take longer to reach saturation. For the mixture supercritical conditions, the solvent is fully miscible with CO<sub>2</sub>, so an effective droplet radius is defined dividing the solvent-rich phase from the CO<sub>2</sub>-rich phase. Unlike the subcritical conditions, the toluene droplets do not always swell with CO<sub>2</sub>. Rather, the droplet size depends on the relative density of the two solvents. If the solvent is denser than the CO<sub>2</sub>, then the effective droplet will swell. Alternatively, if the CO<sub>2</sub> is denser than the solvent, the effective droplet will shrink. This is consistent with the system trying to achieve uniform density. The other major difference between the supercritical

mixture and the subcritical mixture is that the droplet lifetime is much shorter for the supercritical conditions.

Further numerical modeling was performed by Lengsfeld et al. (Lengsfeld et al., 2000) on the jet breakup of injected solvents in the SAS process. She modeled the injection of water, immiscible in CO<sub>2</sub>, 1-octanol, partially miscible in CO<sub>2</sub>, and methylene chloride, miscible in CO<sub>2</sub>, into dense CO<sub>2</sub> by using linear jet breakup theory. Water was used to verify that the linear jet breakup theory was applicable to liquids injected into near-critical and supercritical CO<sub>2</sub>. They then employed dynamic surface tension calculations for the partially miscible 1-octanol along with the linear jet breakup theory. They were able to get good agreement between observed and calculated jet breakup lengths. In the miscible system, they found that the jet breakup lengths measured greatly exceeded the time needed for the dynamic surface tension to essentially vanish. As a result of this analysis, they concluded that for the methylene system, the breakup would not result in droplets, and microparticles formed by injecting methylene chloride solutions into CO<sub>2</sub> would be formed by nucleation and growth in a gas-like plume rather than in droplets. One important observation is that, for simplicity, their analysis did not incorporate solute effects on the surface tension, which can greatly impact the time needed for the dynamic surface tension to become negligible.

Recently, Chavez et al. (Chavez et al., 2003) have used engineering correlations and linear jet breakup theory to estimate the time scales of various mechanisms in the SAS process. Their analysis used the injection of ethanol into supercritical CO<sub>2</sub> in the mixture subcritical regime. For the nucleation time calculations, paracetamol was used as a model compound. For this case, they found that the time required for jet breakup was

much less than that for mass transfer. This means that jet breakup occurs well before a significant amount of CO<sub>2</sub> has diffused into the liquid phase. The nucleation times calculated varied significantly with process conditions. This means that for the system they examined, the process could be limited either by diffusion or by nucleation. These different processes could lead to quite different products.

Several modifications of the SAS process have been made in order to overcome some of the diffusional limitations. Mawson et al. (Mawson et al., 1997) constructed a coaxial nozzle in which their organic solution was sprayed through a capillary nozzle inside of a larger stainless steel tube through which CO<sub>2</sub> flowed. By flowing the CO<sub>2</sub> at a fast rate, the relative velocity of the organic solution is reduced, resulting in larger initial droplets. The fast flow rate of the CO<sub>2</sub> then results in a well-mixed solution and faster diffusion rates. The end result of all these effects is that the resultant particle sizes are larger than those produced at slower flow rates.

Another modification to the SAS process is termed the solution-enhanced dispersion by supercritical fluids (SEDS) method. This method, developed by York and Hanna (York and Hanna, 1996), involved the delivery of an organic solution through a capillary tube and CO<sub>2</sub> through the annulus of a coaxial nozzle. The two fluids are then mixed in a premixing chamber before being sprayed through a small orifice into the high-pressure vessel. The spray is delivered at a high rate resulting in a turbulent flow. Because of both the premixing and the turbulent flow, the diffusion rates are greatly accelerated. Numerical modeling of the process time constants (Shekunov et al., 2001; Shekunov et al., 1999) shows that particle growth is the limiting rate for dense CO<sub>2</sub>. Additionally, they showed that at very high velocities, the particles exited the pressure

vessel before they had sufficient time to finish growing. They concluded that manipulating the flow velocity could produce a minimum particle size.

Another design modification to enhance the diffusion in the SAS process was to use sonic waves to decrease the droplet size by increasing atomization. The earliest use of this approach by Randolph et al. (Randolph et al., 1993) replaced the standard capillary tube with a nozzle that vibrated at 120 Hz. This produces a cylindrical spray that breaks up into small droplets. A similar idea was used by Said et al. (Said et al., 1997) in which a specialized nozzle allowed sonic waves to be focused at the interface of the spray and the supercritical antisolvent. This resulted in both smaller droplets and enhanced mass transfer between the two fluids. Instead of modifying the injection nozzle, Chattopadhyay and Gupta (Chattopadhyay and Gupta, 2001) used a sonicating horn. The spray was then directed onto the vibrating surface of the horn to atomize it. Because the sonic waves were present in the supercritical antisolvent as well, the mass transfer was accelerated. The result of these modifications resulted in very small and uniform particles.

### **Impact of CO<sub>2</sub> Interactions in Nanoparticle Synthesis and Dispersion**

One of the many applications of supercritical CO<sub>2</sub> is in nanoparticle synthesis and processing. To disperse nanoparticles or the reactants necessary for nanoparticle formation in CO<sub>2</sub>, molecular interactions with CO<sub>2</sub> have to be sufficiently large to solvate the reactants or particles. To process nanoparticles in CO<sub>2</sub>, the particles must first be dispersed in CO<sub>2</sub>. A common method to disperse particles in a given solvent is to coat the surface of nanoparticles with a ligand that prevents the agglomeration of particles and has tails that are well solvated by the dispersing solvent. Favorable interactions between

the solvent molecules and the ligand tails provide enough repulsive forces between particles to overcome the attractive Van der Waals forces that occur between particles in solution. (Kitchens and Roberts, 2004). Typically, metallic nanoparticles have been stably dispersed in pure liquid and supercritical CO<sub>2</sub> (Saunders et al., 2004; Shah et al., 2000) by using fluorinated ligands.

The tunable solvent properties of supercritical fluid solvents allow for the reversible dispersion and deposition of nanoparticles onto surfaces (Shah et al., 2002a). Shah et al. increased ethane solvent density to disperse increasingly larger silver and gold nanoparticles in the ethane media. By reducing the ethane density, the largest particles were precipitated first, followed by precipitation of smaller particles as the density was further reduced. By changing the solvent density, they effectively were changing the ability of the ethane to solvate the ligand tails.

One key feature of supercritical carbon dioxide in nanoparticle synthesis is that it has a vanishing surface tension (Shah et al., 2004), making it a desirable process solvent for nano-scale materials and devices. For example, McLeod et al. (McLeod et al., 2005) and Shah et al. (Shah et al., 2003) used this vanishing surface tension in CO<sub>2</sub> systems to make more uniform thin films of nanoparticles than could be made by solvent evaporation techniques. These techniques take advantage of the ability to control the dispersability of nanoparticles through the adjustable properties of CO<sub>2</sub> solvent systems. McLeod et al. (McLeod et al., 2005) formed the nanoparticle films by using CO<sub>2</sub> as an antisolvent in CO<sub>2</sub>-gas expanded liquids. Then, by further increasing the CO<sub>2</sub> pressure and the temperature, the CO<sub>2</sub>-solvent mixture was brought to the supercritical phase and removed. By removing the solvent in the supercritical phase, there was no surface

tension, avoiding film defects resulting from solvent dewetting instabilities present in liquid evaporation.

Unfortunately, CO<sub>2</sub> is a poor solvent for most commonly available ligands and surfactants. As a result, fluorinated ligands and surfactants have been required to stabilize nanoparticles in CO<sub>2</sub> or to form microemulsions for the synthesis of nanoparticles within CO<sub>2</sub>. Early studies showed the ability of these fluorinated surfactants to support water in CO<sub>2</sub> microemulsions (Clarke et al., 1997; Johnston et al., 1996) based on better surfactant tail – solvent interactions. These water in CO<sub>2</sub> microemulsion systems have since been used to form a variety of nanoparticles in CO<sub>2</sub> (Dong et al., 2002; Holmes et al., 1999; Ji et al., 1999; Liu et al., 2005; McLeod et al., 2003; Ohde et al., 2000; Zhang et al., 2003).

Theoretical modeling work by Kitchens (Kitchens and Roberts, 2004) on the stabilization of copper nanoparticles within the surfactant cores in liquid and supercritical fluids showed the importance of molecular interactions between the supercritical fluid medium and surfactant tails in dense fluid microemulsions. Using a force balance model, the maximum size of copper particles that could be stabilized by these systems was calculated as a function of either pressure or temperature. The density had a strong effect on the maximum particle size these systems could stabilize. The solvation of the surfactant tails by the solvent was a critical component of the force balance. Any attempt to use a specific compound as a surfactant in a supercritical fluid should consider the ability of the desired solvent to solvate the surfactant tails effectively.

CO<sub>2</sub> soluble fluorinated compounds suffer from the disadvantages of being both expensive and environmentally unfriendly (Dimitrov et al., 2004; Sarbu et al., 2000b).

Several research groups (Eastoe et al., 2003; Eastoe et al., 2001; Hoefling et al., 1993; Hoefling et al., 1991; Johnston et al., 2001; Lora et al., 1999; Potluri et al., 2002; Raveendran and Wallen, 2003a; Rindfleisch et al., 1996; Sarbu et al., 2000a; Sarbu et al., 2000b; Shen et al., 2003) have sought to find non-fluorinated compounds that would be soluble in CO<sub>2</sub> in the hopes of creating non-fluorinated polymers as well as surfactants where the latter could be used to form microemulsions in CO<sub>2</sub>. Research has shown that branched, methylated, and stubby surfactants can be used to form micelles in supercritical CO<sub>2</sub>, because of higher tail solvation and smaller tail-tail interactions (da Rocha et al., 2003; Eastoe et al., 2001; Stone et al., 2003; Stone et al., 2004).

Some success has been reported in forming fluorine-free microemulsions using hydrocarbon surfactants (Liu et al., 2001; Ryoo et al., 2003) and in making macroemulsions using silica nanoparticles (Dickson et al., 2004), ionic hydrocarbon surfactants (Dickson et al., 2005), or trisiloxane surfactants (da Rocha et al., 2003) in supercritical CO<sub>2</sub>. One group of hydrocarbon surfactants that showed significant solvation by supercritical CO<sub>2</sub> was those that had branched methylated tails. The high CO<sub>2</sub> solvation may be attributable to the highly methylated branched tails, in which the surface energy of the pendant methyl groups is much lower than that of the CH<sub>2</sub> groups of linear tails (O'Neill et al., 1998). The ability of CO<sub>2</sub> to interact effectively with these compounds is critical for forming an aqueous phase in which to synthesize nanoparticles within the bulk supercritical CO<sub>2</sub> phase. However, no reports to date have demonstrated the synthesis or dispersion of nanoparticles within these non-fluorinated surfactant systems.

The need for surfactants, and a separate water phase, in the synthesis of nanoparticles in supercritical CO<sub>2</sub> was eliminated by the synthesis and subsequent precipitation of nanoparticles in a single CO<sub>2</sub> phase (McLeod et al., 2004; Shah et al., 2001, 2002b). The idea of Shah and McLeod was to reduce CO<sub>2</sub>-soluble metallic precursors in a single CO<sub>2</sub> phase and to prevent agglomeration by capping the particles with CO<sub>2</sub>-soluble fluorinated ligands. The interactions of CO<sub>2</sub> with the metallic precursors and with the fluorinated ligands were critical in this process.

These examples of nanoparticle synthesis and processing have shown the importance of molecular interactions with CO<sub>2</sub> in these processes. Because of the expense and environmental problems associated with the fluorinated compounds that are commonly used in nanoparticle synthesis and processing in CO<sub>2</sub>, a fundamental understanding of the nature of CO<sub>2</sub> interactions can greatly aid in nanoparticle processes. Understanding these interactions lets us take advantage of both favorable and unfavorable interactions with CO<sub>2</sub>.

## **Conclusions**

This chapter has provided background information on the solvent characteristics of CO<sub>2</sub>, FTIR and NMR spectroscopy methods to examine high-pressure solutions and specific solvent-solute interactions and given motivation to further examine solute-solvent interactions in CO<sub>2</sub> and to apply this knowledge to various processes. It has also described the importance of solvent-solute interactions in CO<sub>2</sub> in microparticle formation processes such as SAS and nanoparticle formation and processing. Chapter 2 will discuss the utilization of FTIR spectroscopy to study the effect of CO<sub>2</sub> density on the dimerization of various carboxylic acids. This provides information about the interaction

of CO<sub>2</sub> with the carboxylic acid functional group. Chapter 3 will discuss NMR spectroscopy studies of the interaction between CO<sub>2</sub> and the carboxylic acid functional group. High-pressure NMR spectroscopy is discussed as it relates to probing the specific environment around the acidic proton of the carboxylic acid as a function of CO<sub>2</sub> density. Chapter 4 will discuss the visualization of the SAS process. This process takes advantage of the interactions of CO<sub>2</sub> with an injected solvent to cause mutual diffusion leading to the precipitation of an insoluble solute. Chapter 5 will discuss reactive polymerization methods that occur during the SAS process. Polymerizations in a reactive SAS process are discussed. The interaction of CO<sub>2</sub> with amine groups is used to form nylon 6 during the spray process. In a different process, the interaction of CO<sub>2</sub> with carboxylic acids is used to tune the molecular weight of polymethacrylic acid formed by manipulating the CO<sub>2</sub> density. Chapter 6 will discuss the first stable dispersions of silver nanoparticles using a nonfluorinated ligand. The ability of CO<sub>2</sub> to solvate the ligand tails is critical in forming a sterically stable dispersion. Chapter 7 will provide some overall conclusions regarding the nature of molecular interactions in supercritical CO<sub>2</sub> and the impact of these interactions in particle formation processes.

CHAPTER 2  
IR STUDIES OF CARBON DIOXIDE EFFECTS ON CARBOXYLIC ACID  
DIMERIZATION CONSTANTS

The equilibrium constants for dimerization of three different carboxylic acids in near and supercritical carbon dioxide and ethane at various temperatures and densities are presented. Fourier-Transform infrared spectroscopy was used to determine the equilibrium constants by examining the C=O stretching frequencies of the monomer and dimer of the acids in solution. The equilibrium constants for formic acid, propionic acid, and trifluoroacetic acid decrease with temperature for both ethane and CO<sub>2</sub> solvents, and strongly depend upon CO<sub>2</sub> solvent density. The modified lattice fluid hydrogen-bonding (MLFHB) model was used to interpret this density dependence of the equilibrium constants. The density dependence provides evidence for specific solvent-solute interactions between CO<sub>2</sub> and the carboxylic acid functional group, which is attributed to strong Lewis acid-Lewis base interactions. Since carboxylic acids contain both a Lewis acid and a Lewis base moiety, the examination of a strong acid such as trifluoroacetic acid provides insight as to whether CO<sub>2</sub> acts as a Lewis acid or as a Lewis base in these specific interactions. *Ab initio* computations are also presented and indicate that CO<sub>2</sub> interacts strongly with the carboxylic acids.

## Introduction

Carboxylic acids are of significant interest because of their importance in both industrial and in biological processes. Carboxylic acids are used extensively as raw materials for a wide array of products including those in the medical and foodstuff industries. Because of the importance of these acids to the human body, such as the role of formic acid in human metabolism (Ramon and Rios, 1999), a fundamental understanding of these molecules is needed. These molecules are also used both as solvents and as additives and co-solvents under a wide range of conditions. With a thorough understanding of how these molecules interact both with themselves and with other solvents, existing processes may be optimized and new processes may be developed. Because of the emphasis on green engineering and chemistry and because of the wide range of conditions which may be employed, the use of supercritical solvents such as carbon dioxide (CO<sub>2</sub>) in applications of carboxylic acids would be attractive. Researchers have investigated the self-association of carboxylic acids in a wide variety of solvents (Allen and Caldin, 1953; Christian and Stevens, 1972; Fujii et al., 1988; Hizagy and Taha, 1970; Murty, 1971; Murty and Pitzer, 1969; Park et al., 2002; Yamamoto et al., 1999). Although the general trend of these studies shows that the solute-solvent interactions increase as the solvent becomes more polar, no systematic description of how the acids interact with solvents has been given. Much attention has been given to the effect of solvent density on the equilibrium constants associated with hydrogen bonding (Fulton et al., 1991; Gupta et al., 1993; Kazarian et al., 1993; Park et al., 2002). The highly tunable density of CO<sub>2</sub> (McHugh and Krukoni, 1994) which can be used to examine these effects on such acids, along with its environmentally benign nature makes

CO<sub>2</sub> in the near- and super-critical states an attractive solvent to study. Moreover, recent research has focused on the design of molecules soluble in CO<sub>2</sub> (Hoefling et al., 1993; Sarbu et al., 2000), so understanding of interactions of these functional groups in carboxylic acids with CO<sub>2</sub> could aid in the design of new CO<sub>2</sub>-philic compounds. Although carboxylic acids have been shown to form dimers, trimers, tetramers and even higher order oligomers, the bulk of current literature (Christian and Stevens, 1972; Fujii et al., 1988; Hizagy and Taha, 1970; Murty, 1971; Murty and Pitzer, 1969; Park et al., 2002; Yamamoto et al., 1999) suggest that only the monomer and the cyclic dimer of carboxylic acids exist in any appreciable quantity at low concentrations in the gas phase. This simple single dimerization allows a direct correlation between the density of a solvent and its stabilization of the monomer form of the acid. This provides a quantifiable interaction between the acid and the solvent. With that said, under limited conditions, a linear dimer has been observed for certain acids in certain solvents. Fujii et al. (Fujii et al., 1988) observed a third species for acetic acid in CO<sub>2</sub> solutions with ethanol as a co-solvent. Additionally, Murty and Pitzer have reported that trifluoroacetic acid can exist as a linear dimer in slightly basic solvents, such as benzene (Murty, 1971; Murty and Pitzer, 1969). The explanation for both of these observations is that the solvents are capable of hydrogen-bonding with the linear dimer forms of the acids, thus decreasing the energy difference between the cyclic and linear dimer forms. Here we investigate the self-association of formic acid, propionic acid, and trifluoroacetic acid (TFA) in supercritical fluid (SCF) and near-critical CO<sub>2</sub> using Fourier-Transform infrared spectroscopy (FTIR). This allows the examination of the effects of carbon chain length on the dimerization constant as well as the adjustable physical properties of the SCF

solvent. Because of the high solubility of perfluorinated compounds in CO<sub>2</sub> (Hoefling et al., 1993), the use of TFA allows a means to study the influence of this functionality on the dimerization. The non-polar solvent ethane is also employed to provide a comparison of the effects of the solvent type on the acid dimerization of formic acid and propionic acid self-association. *Ab initio* computations are used to compare to the spectroscopic results. Additionally, the modified lattice-fluid hydrogen bonding (MLFHB) model is used to predict the dimerization constants and compare to those obtained spectroscopically. MLFHB parameters are then used to quantify the solvent-solute interactions.

## **Experimental Methods**

### Materials

Formic acid (98% purity, Sigma), propionic acid (99.5+% purity, Aldrich), trifluoroacetic acid (99% purity, Acros) and SFC grade carbon dioxide (99.999% purity, BOC) were used as received. Research grade ethane was purchased from BOC and dried using a gas drier (Alltech) to completely remove the water before use.

### Apparatus

Figure 2-1 shows the experimental apparatus used in the IR experiments. The major components, syringe pump, circulation pump, high pressure cell, and injection valve, are connected with 1/16" stainless steel tubing and high pressure needle valves (HIP, Inc.). A six port injection valve (Valco) is used to introduce a desired carboxylic acid through a 1/16" needle from a gas-tight syringe (Hamilton). The acid is then pumped through the circulating pump (Eldex Laboratories Inc., model no. B-100-S or Accuflow Series II Pump). The fluid then passes into a custom built high-pressure FTIR

cell. Attached to this cell are a digital pressure indicator (Heise model 901A) and a temperature controller (Omega 6071A controller with an RTD). The fluid then passes into an Isco 260D syringe pump which is used as both a mixing vessel and as a pressure controller. The syringe pump is equipped with a water jacket to control the temperature. The fluid then passes through the injection valve to complete the loop.

A cross-sectional view of the custom FTIR cell used is shown in Figure 2-2. The cell is made of 316 stainless steel, and has a flow-through volume of 1.4 mL and optical path length of 2.8 mm. The ZnSe windows (Harrick Scientific, 13 mm diameter and 6 mm thickness) were sealed by rings placed on either side of the windows made from indium foil from Aldrich. This formed a seal both with the window holder and with the cap. The ends of the cell were sealed with rings made from a 1/24" lead sheet (McMaster-Carr). Flexible heaters (Omega) were wrapped around the exterior of the cell to maintain a constant temperature within the cell.

### Procedure

Initially, the entire system was purged twice with CO<sub>2</sub> or three times with ethane, depending on which solvent was being employed, to remove any trace amounts of acid as well as any moisture which could contaminate the experiment. The syringe pump was then filled with a known amount of the desired solvent, CO<sub>2</sub> or ethane. The system pressure was then set and maintained by the syringe pump, while the temperature was controlled by a water jacket connected to a temperature controlled water bath and an Omega temperature controller with RTD probe on the FTIR cell. After allowing several hours for the system to reach steady-state, the total volume of CO<sub>2</sub> was recorded. The fluid was then circulated by a metering pump while the FTIR cell holder compartment

was flushed with dry nitrogen (BOC gases grade 5.0) for an hour. This ensured that both the system was at equilibrium and that the IR was not being adsorbed by ambient water vapors. The solution in the IR cell was maintained at constant temperature by the temperature controller equipped with an RTD temperature probe to within 0.1 °C. A background spectrum was then taken before the introduction of the acid. The acid was then added in fixed amounts by use of the six-port injection valve from an air-tight syringe. This method eliminated the risk of losing solution or contaminating the system with moisture. In all cases, except for formic acid in ethane solvent, 10 µL stepwise injections were made. For formic acid in ethane, 2 µL stepwise injections were made. The system was allowed to equilibrate for about 15 minutes. FTIR spectra for formic acid were then collected on a Perkin-Elmer Spectra 2000 FTIR spectrometer while spectra for propionic acid and TFA were collected on a Nicolet Avatar 360 FTIR. To insure that results from the two instruments were calibrated correctly, spectra for a standard polypropylene film were taken on each instrument and were found to differ by less than 1%. The spectra were collected with 100 averaged scans at 8 cm<sup>-1</sup> for formic acid and 64 averaged scans at 2 cm<sup>-1</sup> for propionic acid and TFA. These spectra were then analyzed as described later. This process was repeated for up to five injections at each temperature and pressure.

The experimental conditions examined in these experiments ranged in temperature from 25 – 50 °C and in pressure from 48 – 138 bar. These conditions cover both the sub- and supercritical regions for both CO<sub>2</sub> (T<sub>c</sub> = 31 °C, P<sub>c</sub> = 74 bar, ρ<sub>c</sub> = 0.49 g/mL) and ethane (T<sub>c</sub> = 32 °C, P<sub>c</sub> = 49 bar, ρ<sub>c</sub> = 0.20 g/mL). The concentrations of acid studied in these experiments ranged from 1.0 to 10.0 mM depending on the volume of

solvent used and the number of injections made. By having concentrations in this range, the total absorbance for the C=O stretching bands remained less than 2. Additionally, since the concentration of acid is so low, the mixture densities can be estimated as the pure solvent densities at the same conditions. The densities for the solvents at each condition were then calculated by using density data obtained from the literature. (Angus et al., 1976; Sychev et al., 1987)

#### Determination of Equilibrium Constants

Aliphatic carboxylic acids in low concentrations generally exist as an equilibrium between the acid monomer and the cyclic dimer form as shown in Figure 2-3. Neither C=O stretching bands of the higher order oligomers (Ramon and Rios, 1999; Stein and Sauer, 1997) nor a band at  $1644\text{ cm}^{-1}$  indicating water in the system (Schultz et al., 1996) were observed. So, the cyclic dimerization constant is given by

$$K = [(CA)_2] / [CA]^2 \quad (1)$$

Where  $[CA]$  is the concentration of the carboxylic acid monomer and  $[(CA)_2]$  is the concentration of the carboxylic acid cyclic dimer. The total concentration of carboxylic acid,  $C$ , is given as

$$C = [CA] + 2[(CA)_2] \quad (2)$$

In order to obtain the necessary concentrations, the method of Fujii and co-workers (Fujii et al., 1988) was used which was originally developed for acetic acid. This method assumes that the Lambert-Beer law applies for both carbonyl bands as shown in Figure 2-4 because of the very dilute conditions. Therefore, the peak areas,  $A_m$  for the monomer and  $A_d$  for the dimer, are given by

$$A_m = e_m * l * [CA] \quad (3)$$

$$A_d = e_d * l * [(CA)_2] \quad (4)$$

Where  $l$  is the cell path length and  $e_m$  and  $e_d$  are the molar extinction coefficients of the monomer and dimer peaks, respectively. The peak areas from the spectral data were obtained by curve-fitting the data using PeakSolve (Galactic Industries Corp.) A combination of Gaussian and Lorentzian peak shapes was used to optimize the fit for each set of data. In order to compute the concentrations, the  $e$  values for each peak are required. By rearranging eqs 2-4

$$C/A_m = 1/(e_m * l) + (2/(e_d * l))(A_d/A_m) \quad (5)$$

and plotting  $C/A_m$  vs  $A_d/A_m$ , the slope and intercept yield the  $e$  values allowing direct calculation of  $K$ . When plotting the ratio of the peak areas against the total concentration over the area of the monomer peak, the resultant graph was quite linear for all three acids studied, with an  $R^2$  value generally greater than 0.98, providing validity to the assumptions made in deriving this equation.

### Modeling

While several hydrogen-bonding theories are available (Economou and Donahue, 1991; Gupta and Brinkley, 1998; Gupta et al., 1992; Heidemann and Prausnitz, 1976; Huang and Radosz, 1990, 1993; Huyskens, 1992; Panayiotou and Sanchez, 1991), we have used the modified lattice-fluid hydrogen bonding (MLFHB) theory (Gupta and Brinkley, 1998; Gupta et al., 1992; Panayiotou and Sanchez, 1991) because of its ability to model the effect of solvent density. The Helmholtz free energy change upon hydrogen bonding,  $F_{ij}$ , is density dependent, which is given by a Taylor series expansion about a standard density,  $\mathbf{r}^\circ = 1$ ,

$$F_{ij} = F_{ij}^\circ + (\mathbf{r}_r - \mathbf{r}^\circ) F_{ij}' + (\mathbf{r}_r - \mathbf{r}^\circ)^2 F_{ij}'' + \dots, \quad \text{where } F_{ij}' = (\delta F_{ij} / \delta \mathbf{r}_r)_{T, r^\circ} \quad (6)$$

Then, a first order approximation is made, keeping the  $F_{ij}'$  term and neglecting the higher order terms. This yields a linear density dependence. In dilute concentrations, with one hydrogen-bonding donor and one hydrogen-bonding acceptor on each molecule, the equilibrium constant,  $K$ , depends on the temperature,  $T$ , the pressure,  $P$ , and the reduced density,  $\mathbf{r}_r$  such that

$$RT \ln K = RT \ln v^* - E^o - PV^o + TS^o - \mathbf{r}_r F' \quad (7)$$

Where  $R$  is the gas constant,  $v^*$  is the lattice- fluid close-packed segment volume, and  $E^o$ ,  $V^o$ , and  $S^o$  are the standard enthalpy, volume, and entropy change upon hydrogen bond formation, respectively (Gupta et al., 1993). The close-packed segment volume,  $v^*$ , is related to the lattice-fluid characteristic pressure,  $P^*$ , and temperature,  $T^*$ , of the solvent according to the relationship  $v^* = RT^*/P^*$ . The final term in this equation accounts for the dependence of the equilibrium constant on the solvent density. Because of differences in solvent-solutes interactions, at similar densities, values of  $F'$  depend upon type of hydrogen-bonding and components. A detailed derivation of this equation from the lattice-fluid hydrogen-bonding theory is presented elsewhere (Gupta et al., 1992). Gas phase values for the hydrogen bonding parameters,  $E^o$  and  $S^o$ , are widely available in the literature (Christian and Stevens, 1972; Coolidge, 1928; Jentschura and Lippert, 1971; Mikhailova et al., 1981; Miyamoto et al., 1999; Winkler and Hess, 1994). By using these along with the lattice-fluid parameters,  $P^*$  and  $T^*$ , obtained from the literature (Gupta et al., 1993) and fixing  $V^o$  to  $-10 \text{ cm}^3/\text{mol}$ , which is typical for hydrogen-bonding species, values for  $F'$  were regressed from the data by finding a best fit for  $\ln K$  versus density for each solvent. The lattice-fluid hydrogen-bonding scaling parameters for various solvents are shown in Table 2-1. The LFHB parameters obtained from the literature used for the

various acids are given in Table 2-2. The reason for the parameters being different for propionic acid in the two solvents is because the parameters that best fit the data were used and the values that best fit each solvent were obtained by different methods.

## **Results and Discussion**

### Formic Acid

Solvent effects on the formic acid dimerization in SCF ethane and CO<sub>2</sub> are discussed elsewhere (Park et al., 2002). These results are briefly summarized here to allow comparison with the propionic acid and trifluoroacetic acid systems in the two solvents. The experimental error for all experiments was typically 10 to 20 percent. The results for formic acid are shown in Figure 2-5 clearly show that the self-association of formic acid decreases significantly as the temperature is increased. The equilibrium constant,  $K$ , remains approximately constant at the gas phase value, 1585 L/mol at 30 °C or 936 L/mol at 37 °C, as the ethane density is increased while the  $K$  values are an order of magnitude lower in CO<sub>2</sub> (at matched densities) and decrease strongly as the density of carbon dioxide solvent is increased for a given isotherm. These trends have also been reported in other systems where a hydrogen bonding species interacts with the solvent, and the solvation becomes more important as the solvent density is increased. (Kazarian et al., 1993) In order to examine this solvent-solute interaction, we have modeled this carboxylic acid dimerization in both the solvents using MLFHB to obtain theoretical values of the dimerization constants at each condition. The best fit results for the modeling are also shown in Figure 2-5. The correlated equilibrium constants from the modeling agree well with the experimental data. The modeling results match the ethane results and the carbon dioxide results at high density almost exactly. The largest

deviation occurs at low CO<sub>2</sub> densities, where the experimental error is expected to be large. Deviations at low densities are expected because of the assumptions in the model. First, the Taylor series expansion for the Helmholtz free energy,  $F$ , is done about a standard density of 1, so the deviations are expected to be larger farther from this point (low density), than close to the point of expansion (high density). Furthermore, the expansion is truncated after the linear term, so when the data is not linear, the model will not fit as well as if more terms in the expansion were used. Both experimental data and model show  $\ln K$  linearly decreases with an increase in CO<sub>2</sub> density. The value of  $F'$  for formic acid in CO<sub>2</sub> is much larger than the  $F'$  value for formic acid in ethane (Table 2-3). This reflects that the CO<sub>2</sub> has much stronger interactions with formic acid than ethane has with formic acid. Furthermore, this value is significantly larger than the value for the PFTB / DME hydrogen bonding in SF<sub>6</sub> (Kazarian et al., 1993). These results suggest that the CO<sub>2</sub> solvent is capable of strong interactions with the acid, which can stabilize the monomer form. This behavior can be attributed to Lewis acid-Lewis base type interactions between CO<sub>2</sub> and formic acid (Kazarian et al., 1996; Meridith et al., 1996; Nelson and Borkman, 1998; Raveendran and Wallen, 2002). As the CO<sub>2</sub> density increases, these interactions become stronger as a result of the closer proximity of solvent and solute molecules, stabilizing the monomer. Since ethane cannot interact with the acid in a similar manner, an increase in density has little effect on the equilibrium.

### Propionic Acid

The spectral data for propionic acid consisted of two distinct peaks: one for the monomer located at 1764 cm<sup>-1</sup> and the other for the cyclic dimer located at 1724 cm<sup>-1</sup>. There was no spectral evidence for the presence of a linear dimer or of any higher

oligomers which would have resulted in peaks at lower wavenumbers. The absence of water contamination was confirmed spectroscopically by observing no peak near  $1640\text{ cm}^{-1}$  (Schultz et al., 1996). The equilibrium constants obtained are summarized in Figure 2-6. These results have the same qualitative form as those for formic acid. The equilibrium constants in ethane change very little with solvent density and remain approximately equal to the gas-phase  $K$  value, while in  $\text{CO}_2$ ,  $\ln K$  decreases dramatically in an almost linear fashion with an increase in solvent density. The major difference between the two acids is that the equilibrium constants for propionic acids are about an order of magnitude larger than those for formic acid. Although the reported gas-phase equilibrium constants for propionic acid vary widely, this observation is in direct agreement with the value reported by Miyamoto et al. (Miyamoto et al., 1999). They report gas-phase equilibrium values at similar temperatures for both formic acid and propionic acid, which differ by about an order of magnitude. In order to account for the solvation energy in these systems, MLFHB modeling has been done for both solvents to obtain theoretical values for the equilibrium constants. The best fit results for the data are shown as the solid lines in Figure 2-6. For the most part, the model agrees well with the experimental data, as the average error between the experimental data and the modeling is less than one percent. The largest deviation from the experimental results comes at the low-density data at the highest temperature. Although these deviations appear to be quite large, the experimental error associated with these points is substantial, where the variation between experimental measurements was as large as 37 percent. Because of the experimental uncertainty, as well as the expected deviations due to the model assumptions of a linear dependence of the free energy on density and that the expansion

is about a standard density of 1, the model is fit to the high density data. Table 2-2 presents the gas-phase MLFHB parameters for each solvent. Because of the large range of reported values for the gas-phase equilibrium constant of propionic acid, the set of parameters which modeled the system best were chosen for each solvent. Both parameter sets used had been optimized in the temperature range of interest. The parameters which best fit the high-density CO<sub>2</sub> data used parameters that were based on gas-phase equilibrium constant lower than those observed in ethane. Using these values for ethane yielded a negative value for  $F'$  in the ethane system, which is not physically realistic. In order to avoid this problem, each set of data was individually optimized yielding positive values of  $F'$  for both systems as shown in Table 2-3. The free energy change upon hydrogen bonding in CO<sub>2</sub> for the two acids is almost identical. This suggests that the increased carbon number has little effect on the strength of the specific interactions of CO<sub>2</sub> with the functional group. This implies that there is no steric effect of the carbon backbone with its increase from formic acid to propionic acid on solvent-solute interactions and that the CO<sub>2</sub> interacts with the functional group. As mentioned previously, these interactions could be the result of Lewis acid-base type interactions between the CO<sub>2</sub> and the carboxylic acid functionality. The optimized value of  $F'$  for propionic acid in ethane is higher than for that of formic acid in ethane, but is an order of magnitude smaller than that for the propionic acid in CO<sub>2</sub>. This confirms the assertion that ethane does not have specific interactions with the carboxylic acid functional group.

### Trifluoroacetic Acid (TFA)

Unlike the other acid systems studied which only had two distinct peaks associated with the monomer and cyclic dimer forms, TFA was observed to have three distinct peaks under certain conditions. An example of this is shown in Figure 2-7. This third peak only exists at the lowest temperature studied. As either the pressure, and consequently density, or temperature of the system is raised, the third spectral band essentially disappears as shown in Figure 2-8. This example is given at higher density, though spectra at a higher temperature look very similar as well. *Ab initio* simulations were performed on several geometrical configurations to determine which species could be responsible for this absorbance. Because of the broadness of the peak, we expected that the species had to have an interaction much weaker than the cyclic dimer. Acid-water complexes, acid-CO<sub>2</sub> complexes, and the linear dimer were simulated. The peak locations for the TFA monomer and cyclic dimer were also simulated to determine the magnitude of the solvent shift. The peak location for the linear dimer matched the experimental location once the solvent shift was taken into account. Furthermore, the strength of this interaction according to these simulations is much less than the cyclic dimer interaction. This accounts for the relative breadth of the peak. Therefore the peak, near 1760 cm<sup>-1</sup> is assigned to the linear dimer. It is well known that CO<sub>2</sub> can act as a Lewis acid (Kazarian et al., 1996; Meridith et al., 1996; Reilly et al., 1995). We previously suggested that acid-base type interactions can occur with the free electrons on the carbonyl oxygen or with the hydroxyl oxygen, thus stabilizing the monomer. Studies of compounds containing carbonyl groups using *ab initio* computations (Nelson and Borkman, 1998), experimental observations (Fink et al., 1999; Rindfleisch et al., 1996),

and FTIR spectroscopy (Kazarian et al., 1996) all supported this idea. In each case, the enhanced solubility of compounds containing carbonyl groups in carbon dioxide was attributed to the free electrons on the carbonyl oxygen interacting with the slightly acidic carbon of CO<sub>2</sub> in a Lewis acid - Lewis Base type interaction. However, our current studies have led us to believe that CO<sub>2</sub> can act as a Lewis base and interact with the acidic proton. It is therefore possible that either one or a combination of both of these factors is responsible for the solvent-solute interactions in CO<sub>2</sub>. Recently, Raveendran and Wallen have used *ab initio* computations to study interactions of sugar acetates containing Lewis base groups with CO<sub>2</sub>. This study suggested that a ring like structure can be formed between the sugar and a CO<sub>2</sub> solvent molecule with two hydrogen bonds: one between the carbonyl oxygen and the carbon of CO<sub>2</sub> and the other between an oxygen on the CO<sub>2</sub> and a proton on the methyl group of the acetate (Raveendran and Wallen, 2002), indicating that CO<sub>2</sub> can act both as an electron donor and as an electron acceptor. However, the interaction with carbon dioxide acting as the Lewis acid is stronger. In our studies, the stabilization of the linear dimer of TFA is consistent with the fact that CO<sub>2</sub> is capable of acting as a Lewis base. As observed by Murty et. al., (Murty, 1971; Murty and Pitzer, 1969) basic solvents, such as benzene, can stabilize the linear dimer form of the TFA self-association. This existence of the linear form is possible because the free electrons on a Lewis base solvent, such as CO<sub>2</sub> can interact favorably with the highly acidic proton on the acid. The fact that this dimeric form does not exist for the other acids in CO<sub>2</sub> is explained by observing that the proton on TFA is much more acidic, a pKa of 0.23, (Cai and Li, 1999) than those of the non-fluorinated carboxylic acids, a pKa of 3.77 for formic acid and a pKa of 4.88 for propionic acid. (Schuurmann et

al., 1998) The presence of the highly electronegative fluorine atoms on the perfluorinated acetic acid results in the electron density shifting toward the fluorines and away from the hydrogen. This effect results in the high acidity which strengthens the solute-solvent interactions, thereby acting to stabilize the linear dimer relative to the cyclic form. The disappearance of this peak as conditions are changed can be rationalized. As the temperature is increased, the hydrogen-bond will be broken due to thermal energy. This accounts for the essential disappearance of the peak with temperature. As the pressure is increased, the linear dimer will convert to the cyclic dimer. For TFA dimerization in CO<sub>2</sub>, there is an enormous decrease in the values of the equilibrium constant going from gas phase to carbon dioxide solvent shown in Figure 2-9. For instance, at 298 K, the equilibrium constant is approximately 5000 L/mol in gas phase, while all values in CO<sub>2</sub> are less than 50 L/mol. This is a two order of magnitude decrease and is much more significant than the decreases of formic acid or propionic acid. This very large decline indicates a much stronger interaction than those for the weaker acids. This result along with the stabilization of the linear dimer of TFA leads us to believe that it is the interaction of the highly acidic proton of TFA with an oxygen of CO<sub>2</sub> that is the dominant stabilizing interaction. This means that CO<sub>2</sub> in the role of a Lewis base is more significant in this case than the role of CO<sub>2</sub> as a Lewis acid.

#### Ab initio Computations

The objectives of the *ab initio* computations are to substantiate the experimental observations and to develop trends in the enthalpy of hydrogen-bond formation for formic acid, propionic acid and trifluoroacetic acid. This is done for the acids in gas phase, in CO<sub>2</sub> and in a non-polar solvent, ethane. Gaussian98 (Foresman and Frisch,

1996; Frisch et al., 2001) program was used for performing the *ab initio* computations. H-bonding energies were calculated by evaluating the energy of the H-bonded complexes and subtracting the energies of the individual molecules from that of the complex. These energies were corrected for basis set superposition error (BSSE) using counterpoise correction method by Boys and Bernardi (Boys and Bernardi, 1970). The procedure used for carrying out these calculations is also outlined by Wolbach and Sandler (Wolbach and Sandler, 1997).

The optimized structures of dimers in gas-phase, in CO<sub>2</sub>, and in ethane are shown in Figure 2-10, Figure 2-11, and Figure 2-12 respectively. Four solvent molecules were incorporated around the acid dimer to specifically study the interaction of the solvent molecules, CO<sub>2</sub> or the non-polar ethane with the acids. This allows computation of the enthalpy of dimer formation of formic acid, propionic acid and trifluoroacetic acid on a molecular level. Another possibility could have been to use the Self-consistent Reaction Field (SCRF) (Frisch and Frisch, 1999; Wong et al., 1991) theory with which the dielectric constant can be changed to that of the solvent. However, doing that alone incorporates only the solvent effect, but does not incorporate the specific molecular interactions between the acids and the solvents. Therefore, SCRF was not used for these computations. Table 2-4 shows that the hydrogen-bond formation enthalpy decreases significantly in the presence of CO<sub>2</sub> as compared to the gas phase energy. This implies that CO<sub>2</sub> specifically stabilizes the monomer relative to the cyclic dimer shifting the monomer-dimer equilibrium to the monomer side.

However, ethane, being a non-polar solvent, interacts with the acids to a lesser extent than CO<sub>2</sub>. Hence, there is very little acid monomer stabilization in the ethane

solvent. Therefore, the enthalpies of hydrogen-bond formation are very close to the gas phase values. In the cases of all the acids, there is a small decrease in the enthalpies of hydrogen-bond formation moving from gas phase to ethane solvent, while there is a relatively large decrease when the solvent is changed to CO<sub>2</sub>.

The enthalpies of hydrogen-bond formation were observed to decrease in succession from formic acid to propionic acid to trifluoroacetic acid (cyclic) to trifluoroacetic acid (linear) in gas phase computations using HF as a basis function. However, the experimentally observed dimerization energies for trifluoroacetic acid (cyclic) are larger than those of formic acid and propionic acid. This incorrect trend is attributed to the fact that HF does not take into account the electronic correlations which play a major role in hydrogen-bonding. For this reason, calculations were repeated using MP2 basis function to incorporate the electronic effects. The trend observed using MP2 agrees well with the experimental results as seen in Table 4-2. The dimerization energy calculations for the carboxylic acids in CO<sub>2</sub> and ethane phases are currently in progress.

#### Establishment of the presence of trifluoroacetic acid linear dimer in CO<sub>2</sub>

An unknown peak was observed in the FTIR spectrum of trifluoroacetic acid in CO<sub>2</sub> as solvent under certain conditions of density and temperature as shown in Figure 2-7. To establish what this peak represents, *ab initio* computations were performed to find the optimized geometry of several species. These species were the trifluoroacetic acid monomer, the cyclic trifluoroacetic acid dimer, the linear trifluoroacetic acid dimer, and a linear association of one molecule each of trifluoroacetic acid and CO<sub>2</sub>. This was followed by frequency analyses to identify the peak location of the C=O stretch vibrations. The differences between the peak locations of the monomer, cyclic dimer,

and linear dimer corresponded to our experimental differences, while those with the trifluoroacetic acid-CO<sub>2</sub> complex did not correspond. The absolute peak locations, however, do not match the experimental results because the *ab initio* computations were performed in vacuum and do not take into account the solvent shifts.

## Conclusions

Both formic acid and propionic acid hydrogen-bonding studies showed that the monomer form was much more stabilized in CO<sub>2</sub> than in ethane relative to the dimer. As the density of the CO<sub>2</sub> solvent increased, the equilibrium constant decreased strongly, due to the existence of a specific interaction between the acids and the CO<sub>2</sub> solvent.

Whereas, the equilibrium constant remained relatively constant as ethane density was increased. The density dependence for hydrogen-bonding was modeled using MLFHB theory, which suggested that both the acid monomers were stabilized by roughly the same amount relative to the acid dimers as the CO<sub>2</sub> density is increased. Therefore, the carbon number seems to have little effect on the specific interactions of CO<sub>2</sub> with the acid functional group, suggesting no difference in steric hindrance. TFA did not exist purely as a monomer / cyclic dimer equilibrium in all conditions. Studies showed the existence of a third peak in CO<sub>2</sub> at a low temperature (298 K) and high densities (0.781 - 0.816 g/cm<sup>3</sup>) which corresponded to the linear dimer of TFA. All of these results suggest that a combination of Lewis acid-Lewis base interactions between the carbon on CO<sub>2</sub> and the carbonyl oxygen on the acids and between an oxygen on CO<sub>2</sub> and the acidic proton on the acids act to stabilize the monomer. However, the interaction of the CO<sub>2</sub>, acting as a Lewis base, with the acidic proton seems to be the dominant solvent-solute interaction. As a result, the ability of CO<sub>2</sub> to act both as a Lewis base (this study) and as a Lewis acid

(Meridith et al., 1996) and to have significant interactions should be taken into account when designing CO<sub>2</sub>-soluble molecules.

**Table 2-1.** LFHB scaling parameters for pure fluids. (Gupta et al. 1993)

Fluid	$T^*$ (K)	$P^*$ (MPa)	$\rho^*$ (kg/m <sup>3</sup> )
Methanol	496	315	786
Ethanol	464	328	826
Water	518	475	853
Ethane	315	327	640
Carbon dioxide	305	574	1510

**Table 2-2.** LFHB parameters for carboxylic acid self-association.

Hydrogen-bonding Pair	$E^o$ (kJ/mol)	$S^o$ (J/mol/K)	$V^o$ (cm <sup>3</sup> /mol)
Formic acid---Formic Acid <sup>a</sup>	-58.8	-151	-10.0
Propionic acid---Propionic Acid (CO <sub>2</sub> ) <sup>b</sup>	-61.8	-146.1	-10.0
Propionic acid---Propionic Acid (C <sub>2</sub> H <sub>6</sub> ) <sup>c</sup>	-46.4	-87.1	-10.0
TFA---TFA <sup>d</sup>	-56.1	-116.3	-10.0

<sup>a</sup> From Coolidge (Coolidge 1928)

<sup>b</sup> From Miyamoto et. al. (Miyamoto et al. 1999)

<sup>c</sup> From Mikhailova, et. al. (Mikhailova et al. 1981)

<sup>d</sup> From Christian and Stevens (Christian and Stevens 1972)

**Table 2-3.** Comparison of estimated free energy change upon hydrogen-bonding in different systems.

Hydrogen-Bonding	Solvent	$F'$ (kJ/mol)
Formic acid / Formic Acid	CO <sub>2</sub>	11.5
Formic acid / Formic Acid	C <sub>2</sub> H <sub>6</sub>	0.5
Propionic acid / Propionic Acid	CO <sub>2</sub>	11.7
Propionic acid / Propionic Acid	C <sub>2</sub> H <sub>6</sub>	1.1
TFA / TFA	CO <sub>2</sub>	6.9
PFTB / DME	SF <sub>6</sub> <sup>a</sup>	3.0

<sup>a</sup> From Kazarian et. al. (Kazarian et al. 1993)

**Table 2-4.** Dimerization energies for carboxylic acids in gas phase, CO<sub>2</sub>, and ethane using different basis sets.

Basis set:	Dimerization Energies (per bond)					
	HF/6-31+G(d,p)			MP2/6-31+G(d,p)		
	Gas Phase	with CO <sub>2</sub>	With Ethane	Gas Phase	with CO <sub>2</sub>	with Ethane
Formic Acid---Formic Acid	-27.00	-20.42	-25.23	-26.83	-22.67	
Propionic Acid---Propionic Acid	-26.84	-21.40	-25.88	-27.80		
TFA---TFA (cyclic dimer)	-24.35	-16.05	-22.20	-29.52		
TFA---TFA (linear dimer)	-22.23	-14.74		-34.86		

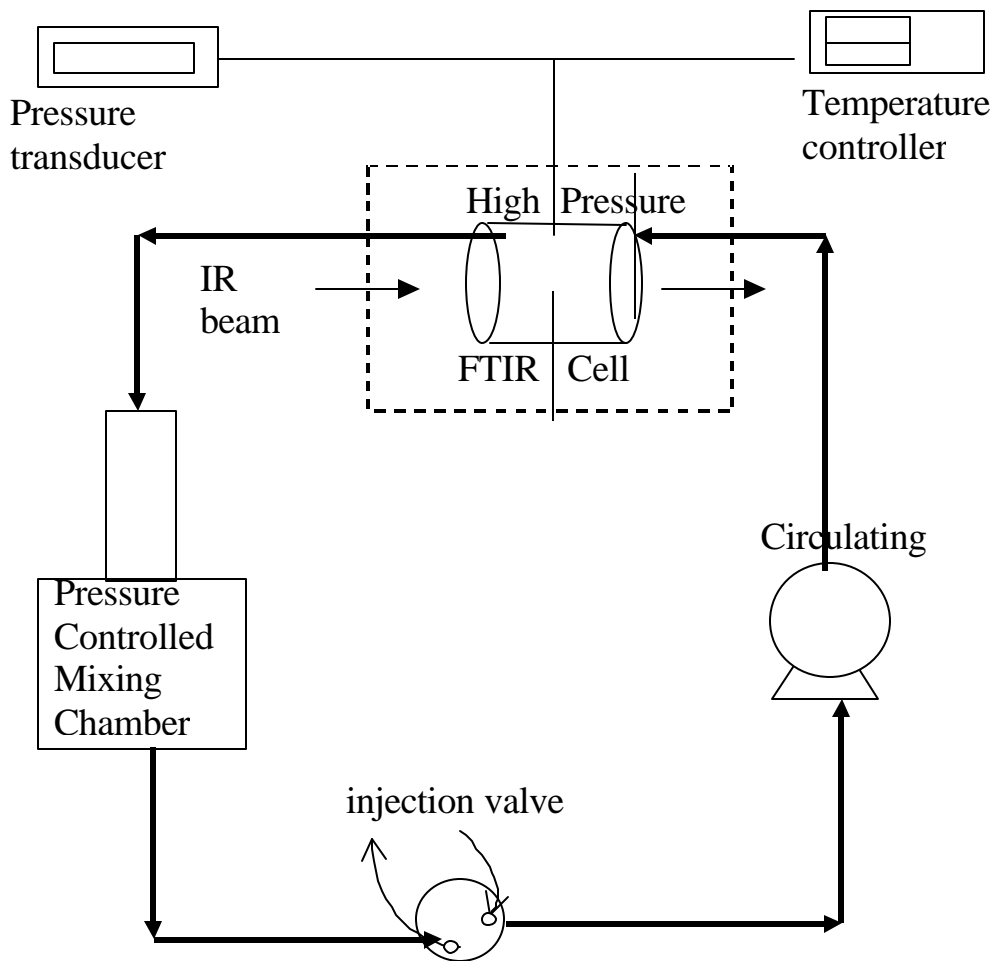


**Figure 2-1.** Experimental setup for high-pressure FTIR measurements.

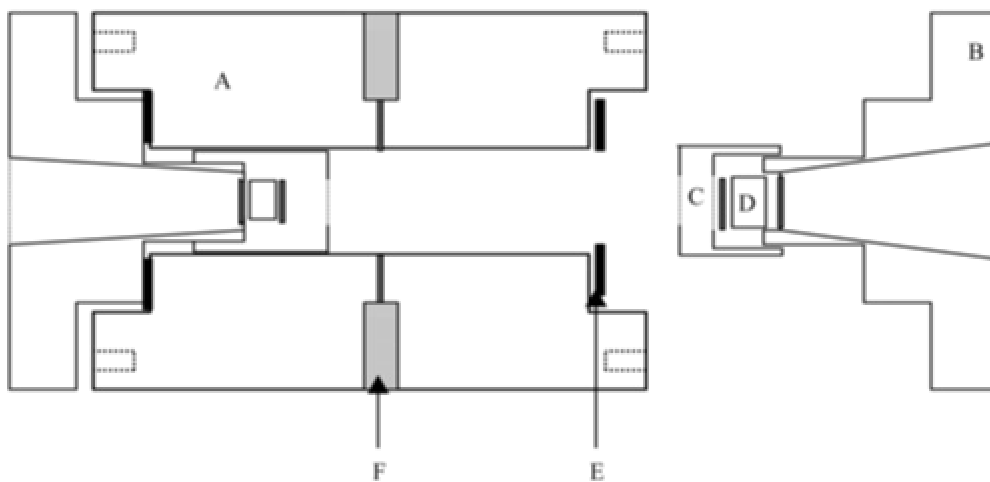


**Figure 2-2.** Schematic diagram of a high-pressure cell: A, housing; B, window holder; C, cap; D, ZnSe window; E, lead sheet; F, inlet, outlet temperature, and pressure port.

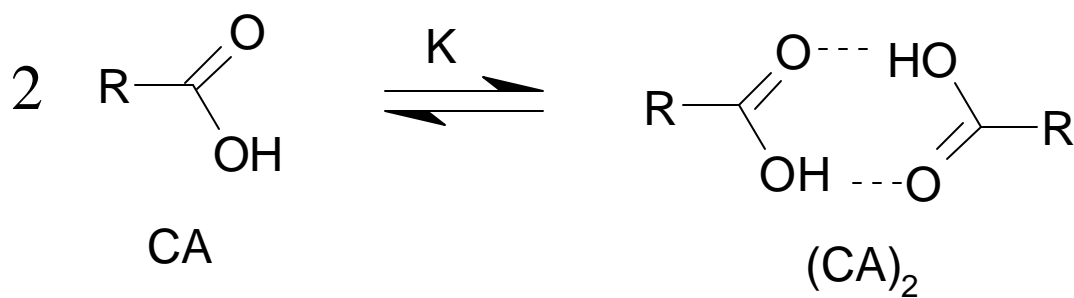


**Figure 2-3.** Generalized carboxylic acid dimerization equilibrium where  $K$  is the dimerization constant and R is a carbon chain.

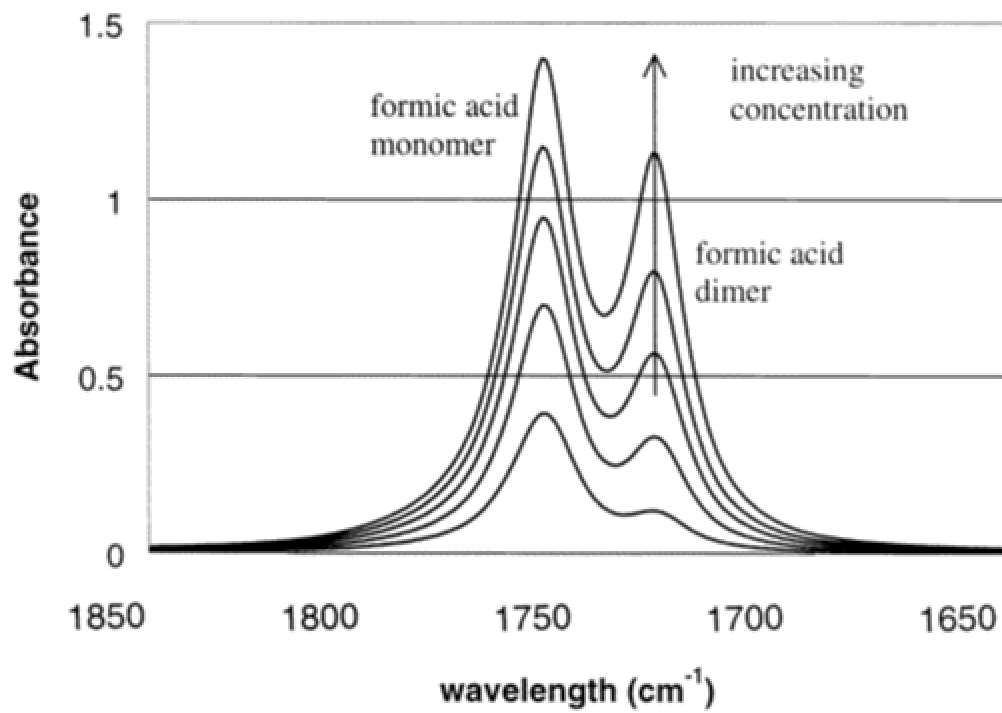


**Figure 2-4.** FTIR spectra of the C=O stretching band for formic acid in carbon dioxide at 303 K and 88 bar.

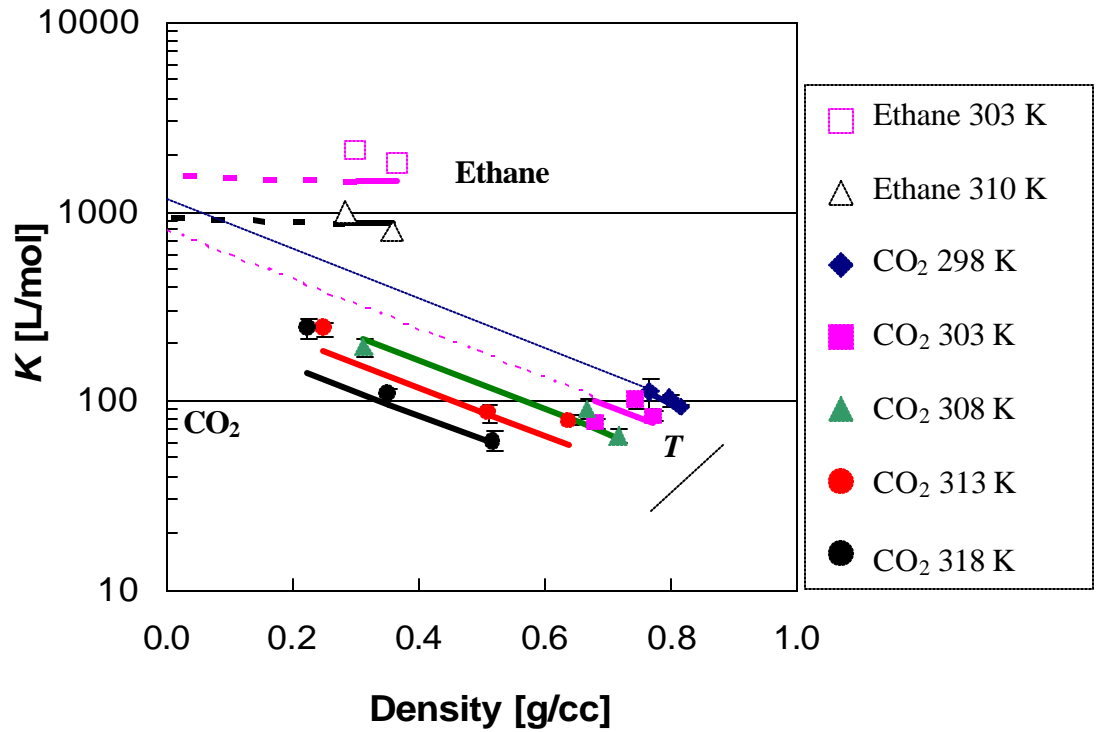


**Figure 2-5.** Variation of  $K$  for formic acid with density along different isotherms in carbon dioxide and ethane solvents. The solid lines indicate the MLFHB modeling results and the dashed lines represent linear extrapolations to the gas phase  $K$  values (Park et al. 2002).

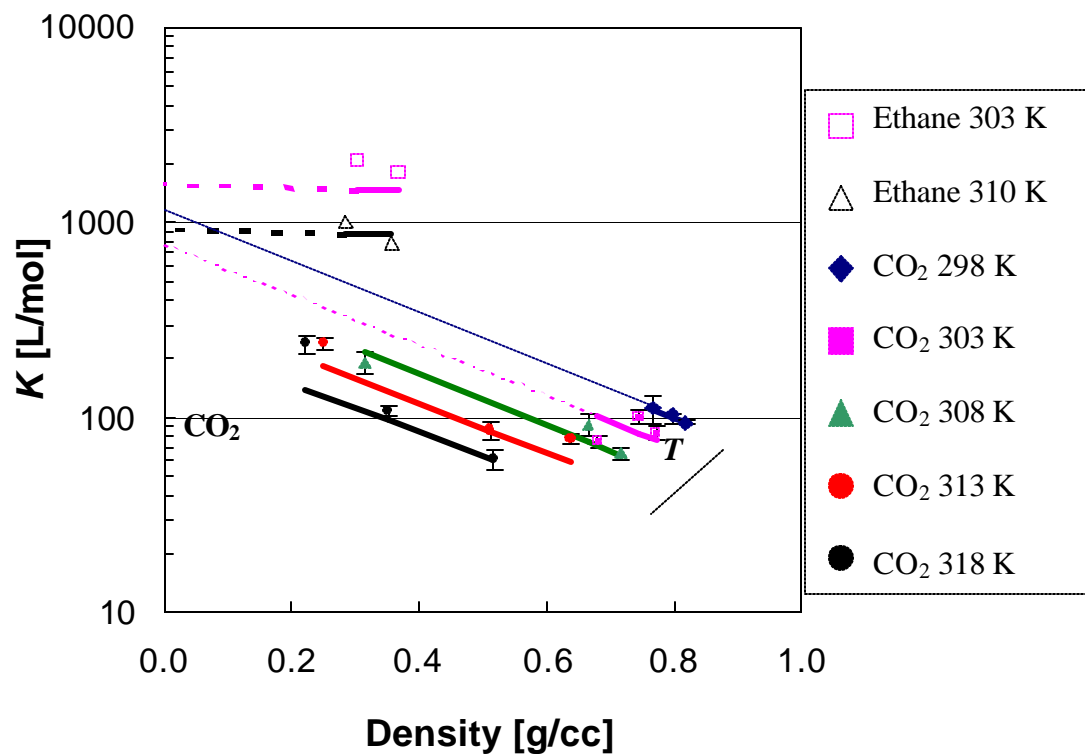


**Figure 2-6.** Variation of  $K$  for propionic acid with density along different isotherms in carbon dioxide and ethane solvents. The solid lines indicate the MLFHB modeling results.

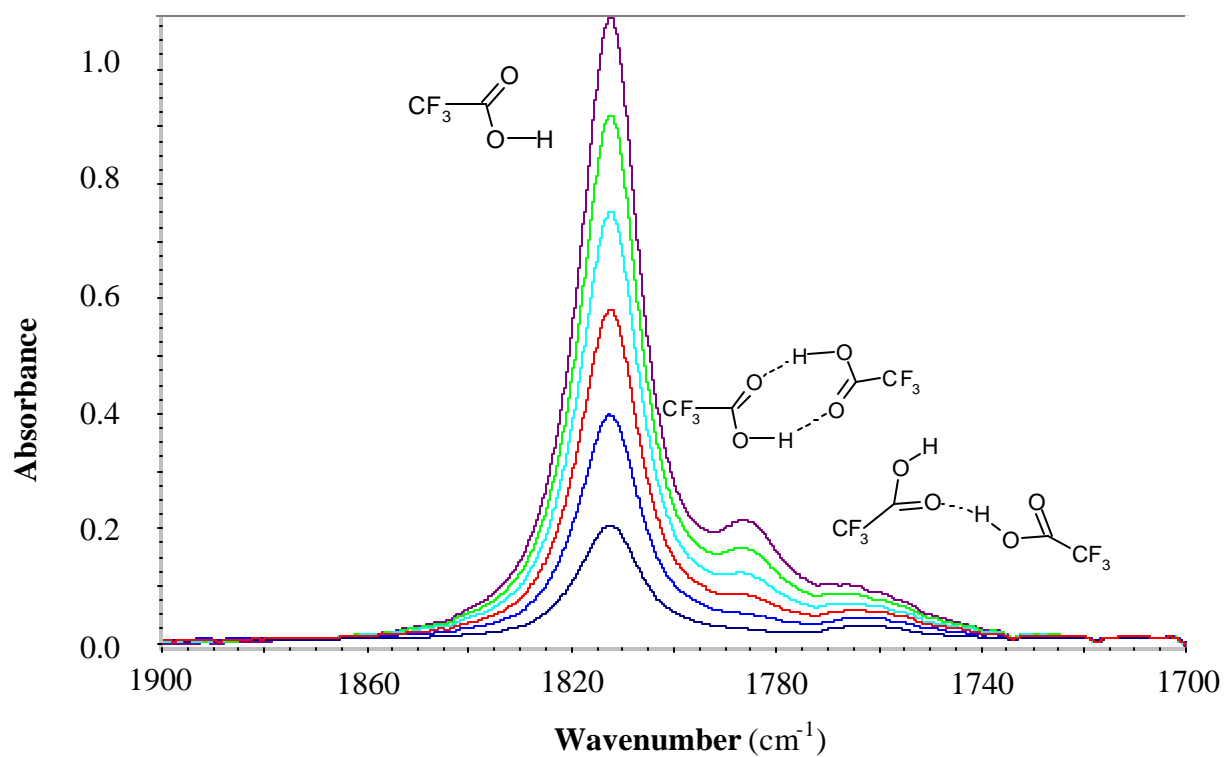


**Figure 2-7.** TFA spectra taken at 25 °C and 82.7 bar in CO<sub>2</sub>. The three peaks shown correspond to the monomer, cyclic dimer, and linear dimer of TFA in that order as the wavenumber decreases.

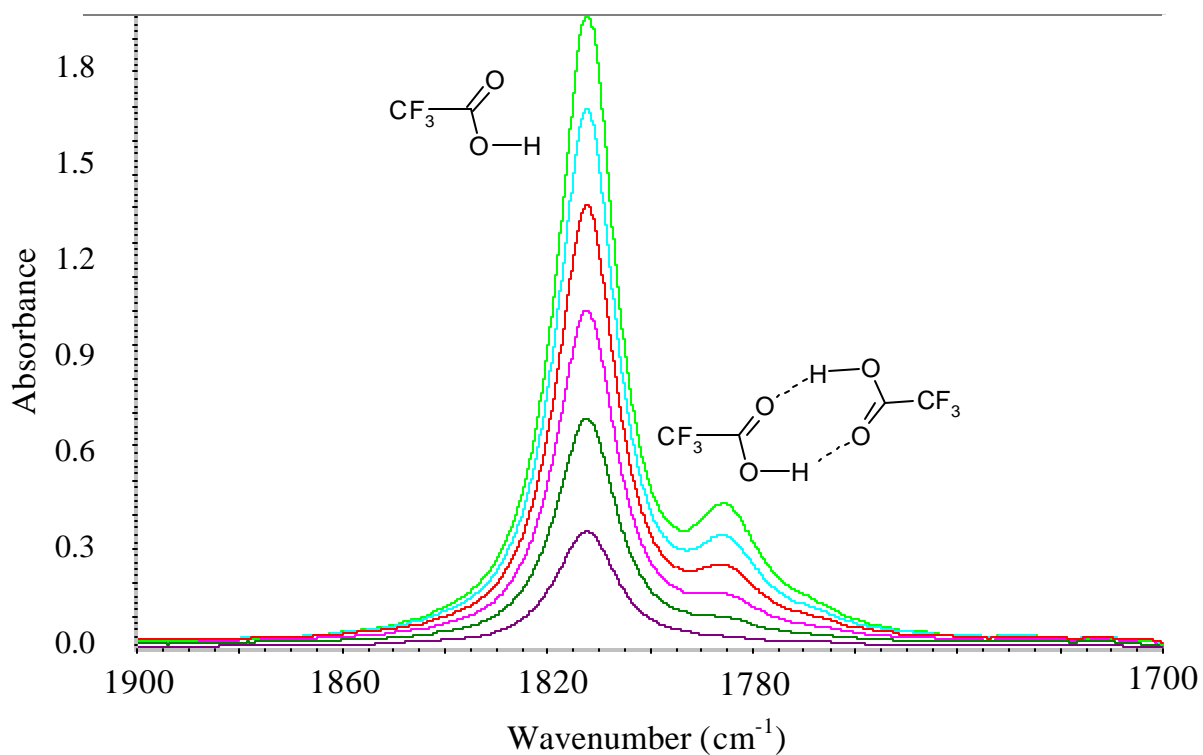


**Figure 2-8.** TFA spectra taken at 25 °C and 117 bar in CO<sub>2</sub>. At this density (0.841 g/cm<sup>3</sup>), only two distinct peaks, corresponding to the monomer and the cyclic dimer of TFA, are observed. The third peak, corresponding to the linear dimer of TFA, has essentially vanished.

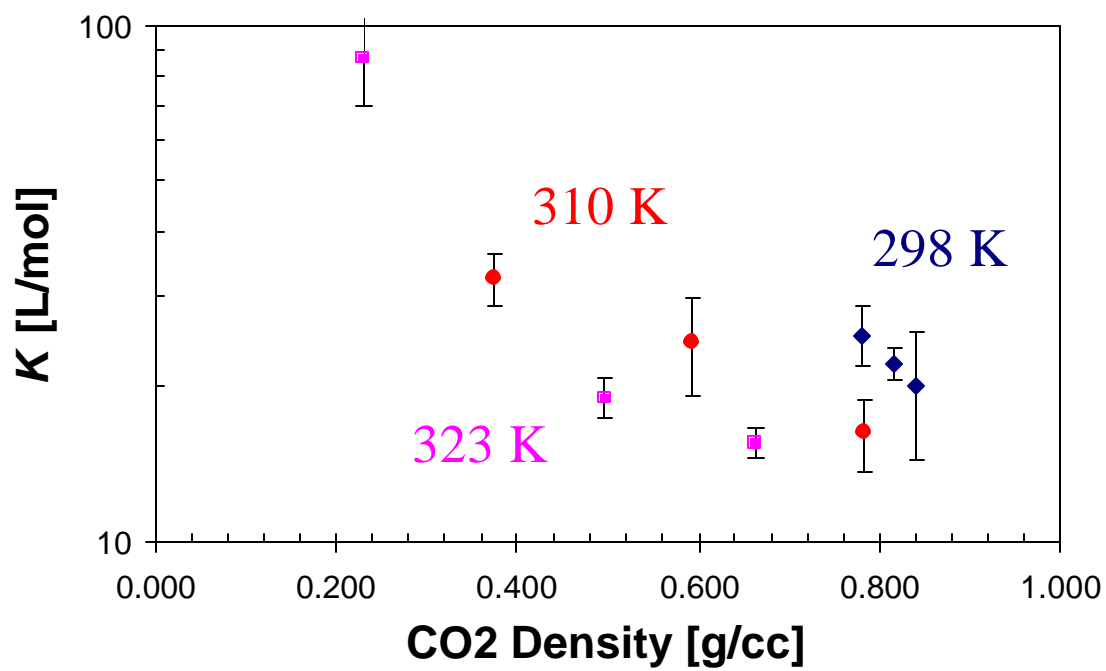
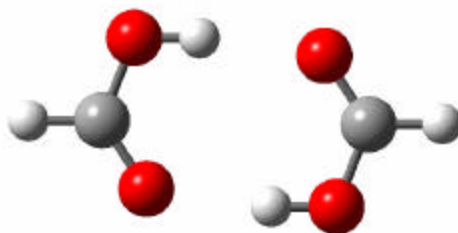
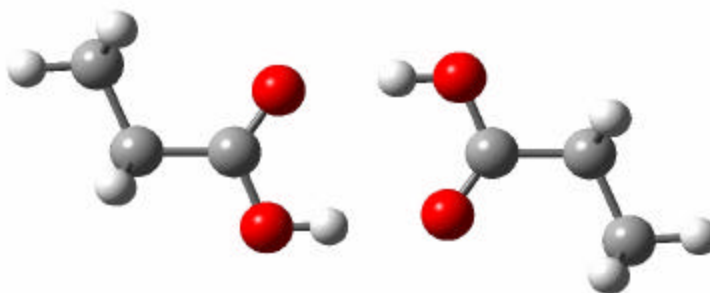


**Figure 2-9.** Variation of  $K$  for trifluoroacetic acid with density along different isotherms in carbon dioxide solvent.



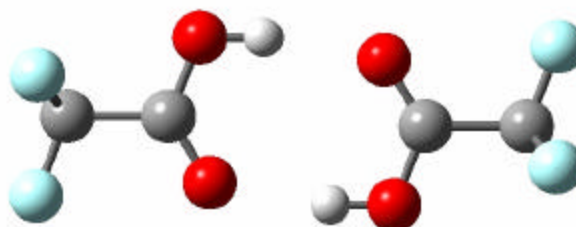
(a)

---



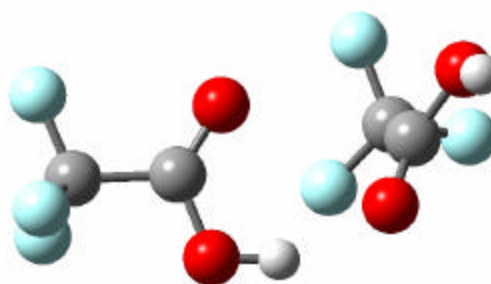
(b)

---



(c)

---



(d)

---

**Figure 2-10.** Acid Dimers: a) Formic Acid Dimer, b) Propionic Acid Dimer, c) Trifluoroacetic Acid Dimer (cyclic), d) Trifluoroacetic Acid Dimer (linear).

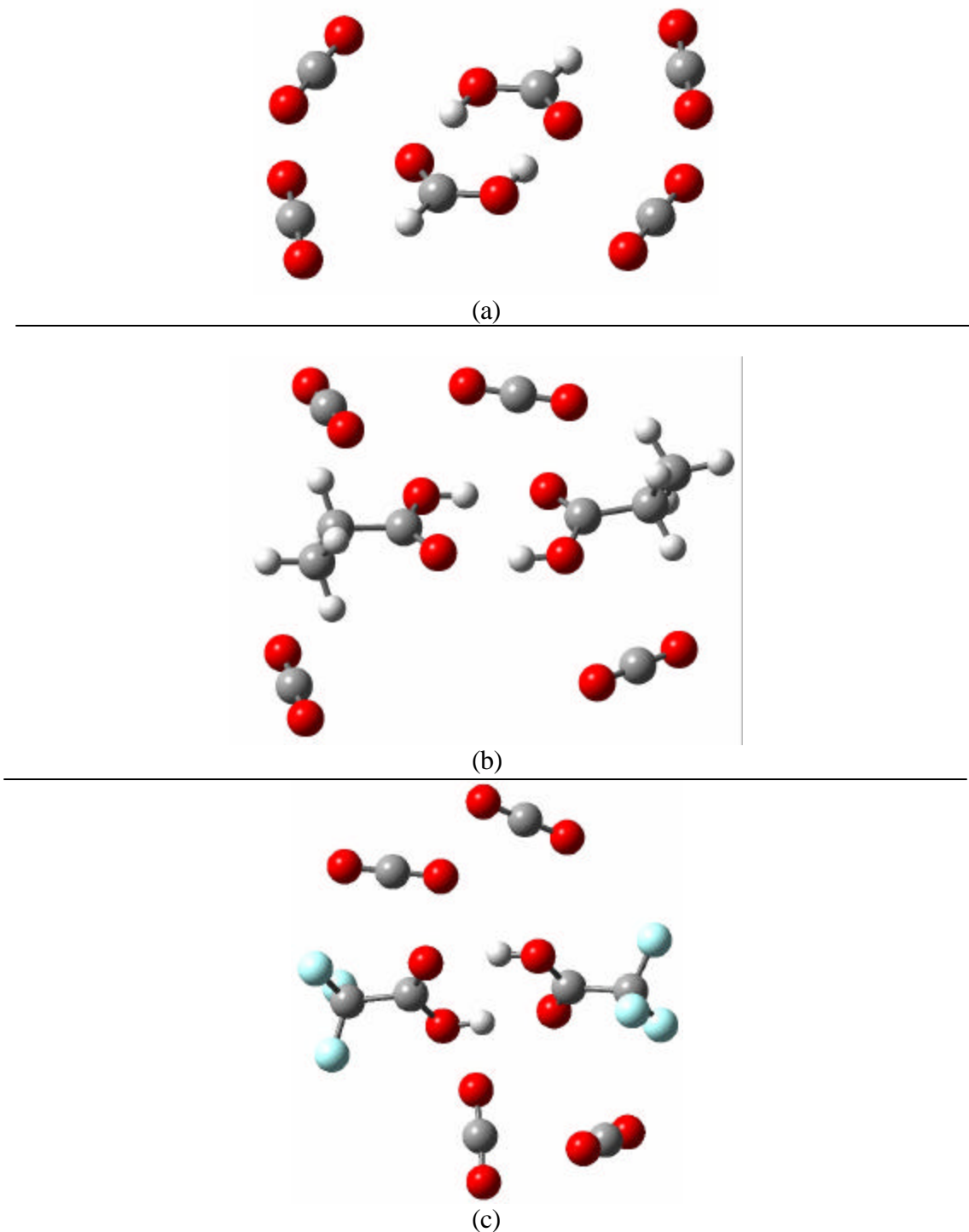
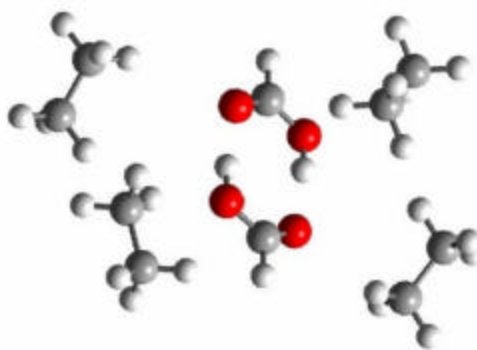
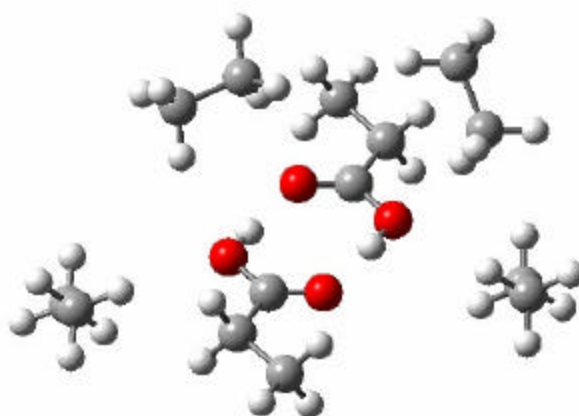


**Figure 2-11.** Optimized structures of Acid Dimers in the presence of CO<sub>2</sub>. a) Formic Acid Dimer, b) Propionic Acid Dimer, c) Trifluoroacetic Acid Dimer (cyclic).



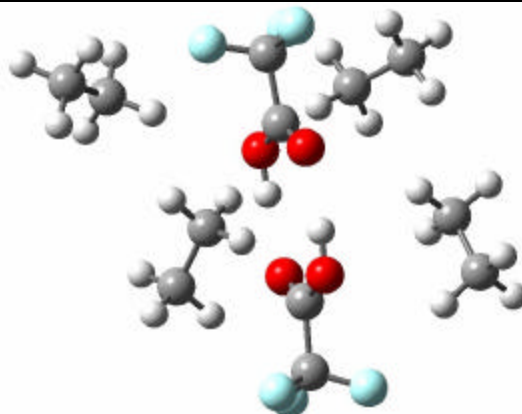
(a)

---



(b)

---



(c)

---

**Figure 2-12.** Optimized structures of Acid Dimers in the presence of Ethane. a) Formic Acid Dimer, b) Propionic Acid Dimer, c) Trifluoroacetic Acid Dimer (cyclic).

## CHAPTER 3

### NMR INVESTIGATIONS OF SPECIFIC INTERACTIONS BETWEEN CARBON DIOXIDE AND CARBOXYLIC ACIDS

#### **Abstract**

Infrared spectroscopy studies have indicated the existence of specific interactions between the carboxylic acid functional group and carbon dioxide. These studies suggested that these interactions arise from the interaction of carbon dioxide with the acidic proton of the carboxylic acids where  $\text{CO}_2$  acts as a Lewis base. The feasibility of using high pressure nuclear magnetic resonance spectroscopy to probe the existence of this interaction is investigated here. The density dependence of the acid proton chemical shift of formic acid reflects an electronic interaction. Unfortunately, the density dependent dimerization equilibrium and the inability to resolve the carboxylic acid monomer and dimer peaks masked any direct observation of these interactions. Based on these findings, strongly acidic compounds that do not self-associate should be chosen in future studies to probe the ability of carbon dioxide to act as a Lewis base.

## Introduction

Nuclear magnetic resonance (NMR) is a powerful tool, which can be used to address the nature of the interactions between CO<sub>2</sub> and carboxylic acids. The advantage of NMR over other methods is that NMR allows the observation of the electron density of individual atoms on the acid molecules. If an atom is involved in a hydrogen-bond or other electronic interaction, then the electron density is directly changed. By observing the chemical shift, related to the electron density, the magnitude of the change in electron density can be determined (Jameson, 1991). As discussed in Chapter 1, there have been numerous NMR cell designs to allow for NMR studies of pressurized fluids such as supercritical fluids. Several researchers have used these cells to study specific interactions of molecules with supercritical fluids (Blatchford et al., 2003; Dardin et al., 1998; Kanakubo et al., 2002; Yonker and Palmer, 2001). They were able to use the change of chemical shifts with solvent density to probe these interactions because the slope of this relation in CO<sub>2</sub> has been shown to be the sum of the bulk magnetic susceptibility and any solvent-solute interactions (Lim et al., 1993). The infrared, IR, spectroscopy studies in Chapter 2 showed that specific interactions exist between supercritical CO<sub>2</sub> and carboxylic acids. Specifically, the study of trifluoroacetic acid, TFA, suggested that an interaction existed between the acidic proton of TFA and the oxygen of CO<sub>2</sub>. If these interactions are electronic in nature, such as a weak hydrogen bond, then the local electron density of an atom involved in the interaction is changed. <sup>1</sup>H NMR can be used to probe the existence of a weak hydrogen bond between the acidic proton of carboxylic acids and the oxygen of CO<sub>2</sub>. The work of Dardin et al. (Dardin et al., 1998) showed that the <sup>1</sup>H chemical shift of alkanes have no electronic interactions

with CO<sub>2</sub>, and shift linearly with CO<sub>2</sub> density. If the chemical shift changes as a function of density relative to an alkane reference, ethane, then this investigation will show the existence of a density-dependent interaction. If the chemical shift does not change as a function of density, then the interaction between dense CO<sub>2</sub> and carboxylic acids must be through some other interaction or interactions.

## **Experimental**

To use NMR for high-pressure fluids, a high-pressure NMR cell was constructed with a polyetheretherketone (PEEK) polymer cell body with a carbon reinforced PEEK cap. This cell is based on the design of Wallen and co-workers (Wallen et al., 2000), and includes the modifications of Yonker and Linehan (Yonker and Linehan, 2002) and Tai et al. (Tai et al., 2002). A picture of the PEEK cell is shown in Figure 3-1. The instrument used was a Varian Mercury Vx magnet at 400 MHz with a 10mm broad band probe. The software used to obtain the NMR chemical shift data was Varian 6.1B. To prepare samples for the NMR, ethane was added by connecting an empty syringe pump (ISCO 260D) to a cylinder of ethane and opening the ethane tank valve to pressurize the dead volume of the syringe pump. The syringe pump was then filled with CO<sub>2</sub> and pressurized to the experimental pressure. The desired amount of formic acid (98% purity, Sigma) was then added by using a six-port injection valve (Valco) in a closed loop with the syringe pump and circulated using a metering pump (Eldex Laboratories Inc., model no. B-100-S). The system was equilibrated at room temperature using the metering pump for several hours to obtain a uniform system. The solution was charged to the high-pressure NMR cell by connecting the syringe pump directly to the PEEK cell by standard PEEK tubing and PEEK finger-tight fittings (McMaster-Carr). The pressure was maintained by

the computer-controlled syringe pump. The NMR cell was lowered into the magnet by the PEEK tubing until it rested properly in the 10 mm broadband probe. The PEEK tubing and fittings were chosen to ensure that no metal came near the magnet, but the tubing prevented the cell from spinning. This is a disadvantage, because the sample is normally spun around a central axis at a high rate to average out the small differences in magnetic field within the sample.

## Results

The chemical shift of ethane in CO<sub>2</sub> at 295 K with no acid present is plotted as a function of density in Figure 3-2. Because there are no specific interactions between ethane and CO<sub>2</sub>, there is a linear relationship between the <sup>1</sup>H chemical shift of ethane and the solvent density. Because of the lack of specific interactions between ethane and the solvent, CO<sub>2</sub>, and the solute, formic acid, ethane was chosen as an internal reference. The behavior of ethane at 310 K and 323 K was similarly linear. To examine the interaction of CO<sub>2</sub> with the carboxylic acid group, the simplest carboxylic acid, formic acid, was chosen. Formic acid has an aldehyde proton and an acid proton. The aldehyde proton should have no specific interactions with CO<sub>2</sub>, while the acid proton could participate in a weak Lewis acid – Lewis base interaction with CO<sub>2</sub>. The <sup>1</sup>H chemical shift as a function of CO<sub>2</sub> density at 295 K for the aldehyde proton is given in Figure 3-3. The chemical shifts shown are relative to the chemical shift of the internal standard, ethane. The chemical shift difference remains approximately constant, indicating that the absolute chemical shift varies linearly with CO<sub>2</sub> for the aldehyde proton. This is expected because of there being no specific interactions of the aldehyde proton with CO<sub>2</sub>. Figure 3-4 shows the chemical shift difference for the acid proton of formic acid as a

function of CO<sub>2</sub> density. The chemical shift difference is not a constant value, indicating that the acid chemical shift does not depend entirely on the change in bulk magnetic susceptibility. Unfortunately, the density range attainable at 295 K to remain in the liquid phase is quite small. To address this issue, the temperature was changed to 323 K, greatly increasing the attainable density range. Figure 3-5 and Figure 3-6 show the chemical shifts relative to ethane as a function of CO<sub>2</sub> density at 323 K for the aldehyde and acid protons, respectively. As was the case for 295 K, the aldehyde proton chemical shift difference remains relatively constant at 323 K, reflecting the absence of any specific electronic interactions between the aldehyde proton and CO<sub>2</sub>. Although the deviation from the ethane slope is in the opposite direction for the acid proton at 323 K, the change in slope over the broad density range confirms that there is an electronic interaction that affects the chemical shift of the acid proton.

## **Discussion**

The reported evidence of an electronic interaction involving the acid proton could be the result of an acid – base interaction with the CO<sub>2</sub> solvent. Unfortunately, there is the self-association of formic acid which confounds the problem. Ideally, there would be two distinct NMR resonance bands for the acid proton. One peak would be for the acid monomer and the other for the acid dimer. Since the acid monomer would be able to interact with the CO<sub>2</sub>, but not the acid dimer, the monomer peak should shift at a different rate with density than ethane, while the dimer peak should shift at the same rate as the ethane peak. Because the cell was not spun and the temperature was high to allow for a wide density range, the dimerization equilibrium was too fast to be distinguished at the NMR timescale used. This resulted in a broad hump rather than two distinct peaks that

changed with density. The average peak shift, as reported, can also not be used to determine if there is an interaction with CO<sub>2</sub> because the dimerization equilibrium is density dependent in CO<sub>2</sub>. As a result, the effects of specific interactions with CO<sub>2</sub> are indistinguishable from the change in equilibrium constant for the formic acid system. This problem is not unique to formic acid, but to carboxylic acids in general. To probe the ability of CO<sub>2</sub> to act as a Lewis base, a molecule with a relatively strong Lewis acid group that cannot hydrogen bond with itself should be used.

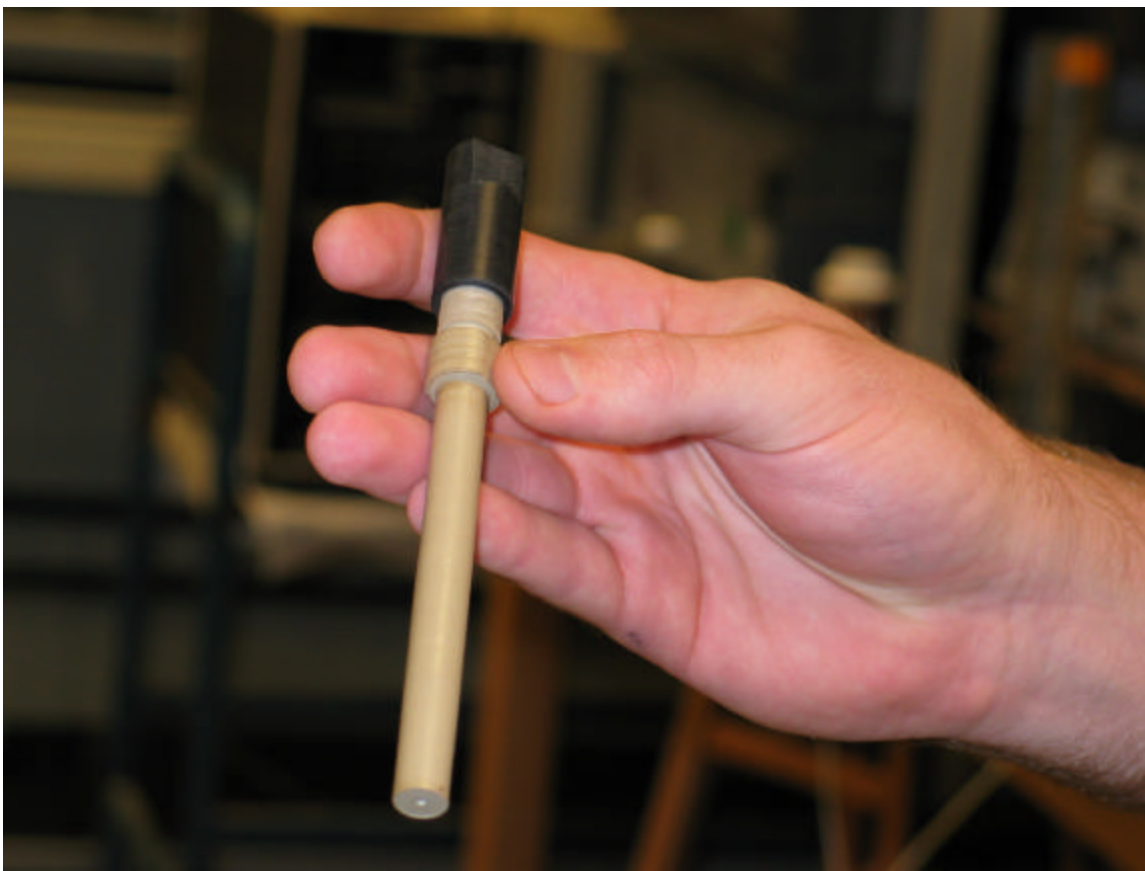


**Figure 3-1** PEEK NMR cell used in the NMR investigations of CO<sub>2</sub> interactions with carboxylic acids. The tan part is the PEEK cell body, and the black part is the carbon-reinforced PEEK cap.

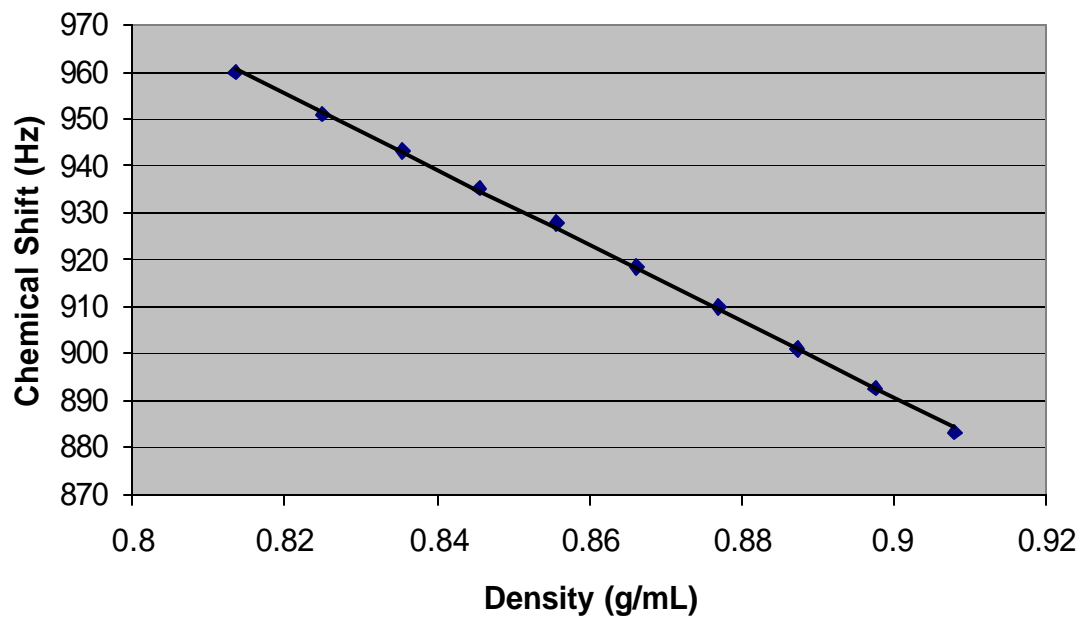


**Figure 3-2** Ethane  $^1\text{H}$  chemical shift as a function of  $\text{CO}_2$  density at 295 K.

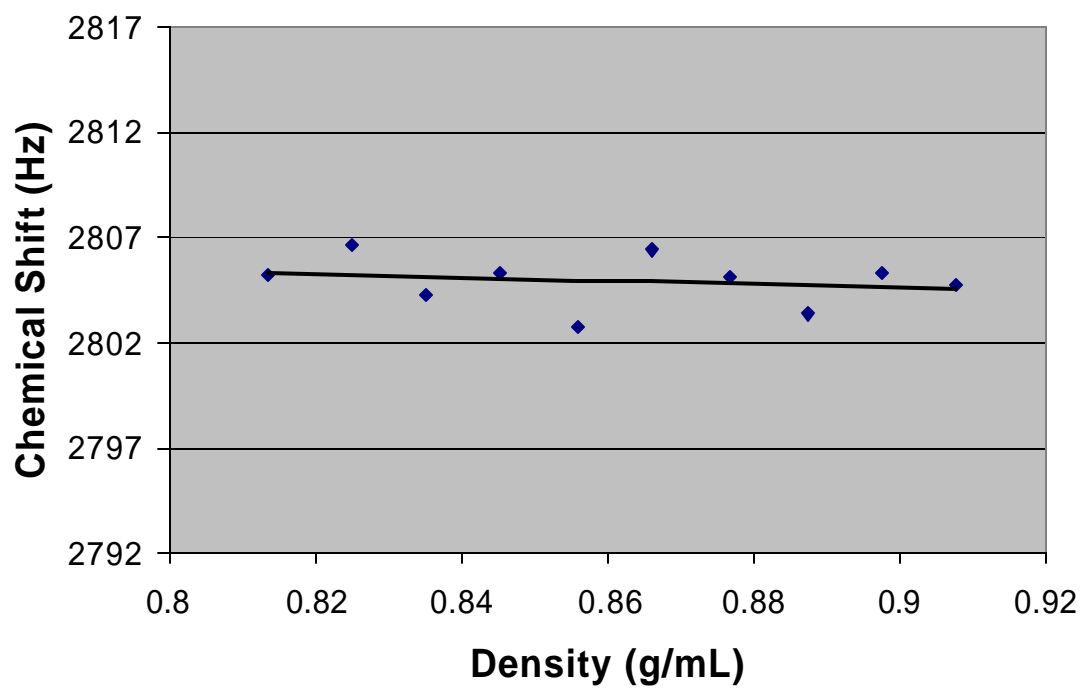


**Figure 3-3** The aldehyde  $^1\text{H}$  chemical shift of formic acid relative to ethane as a function of  $\text{CO}_2$  density at 295 K.

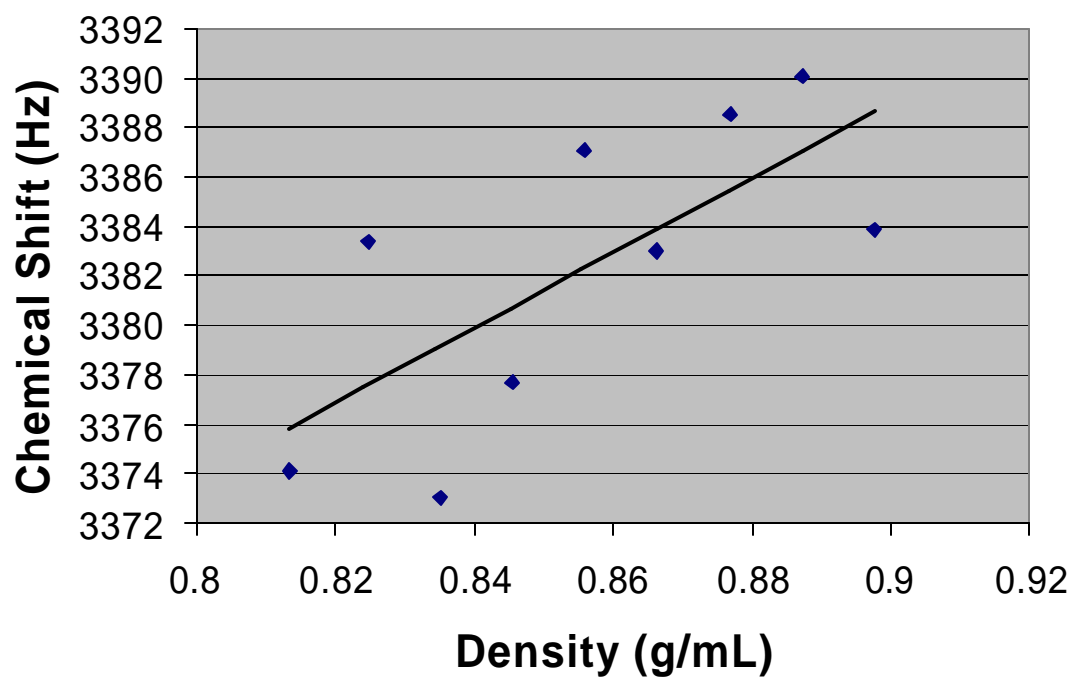


**Figure 3-4** The acid  $^1\text{H}$  chemical shift of formic acid relative to ethane as a function of  $\text{CO}_2$  density at 295 K.

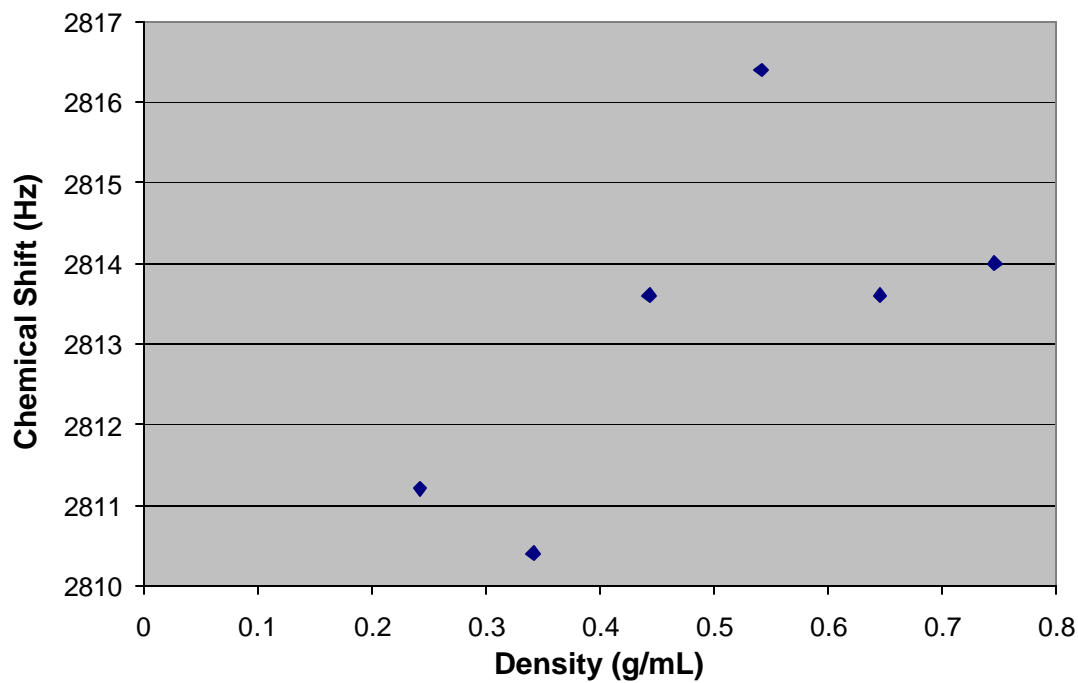


**Figure 3-5** The aldehyde  $^1\text{H}$  chemical shift of formic acid relative to ethane as a function of  $\text{CO}_2$  density at 323 K.

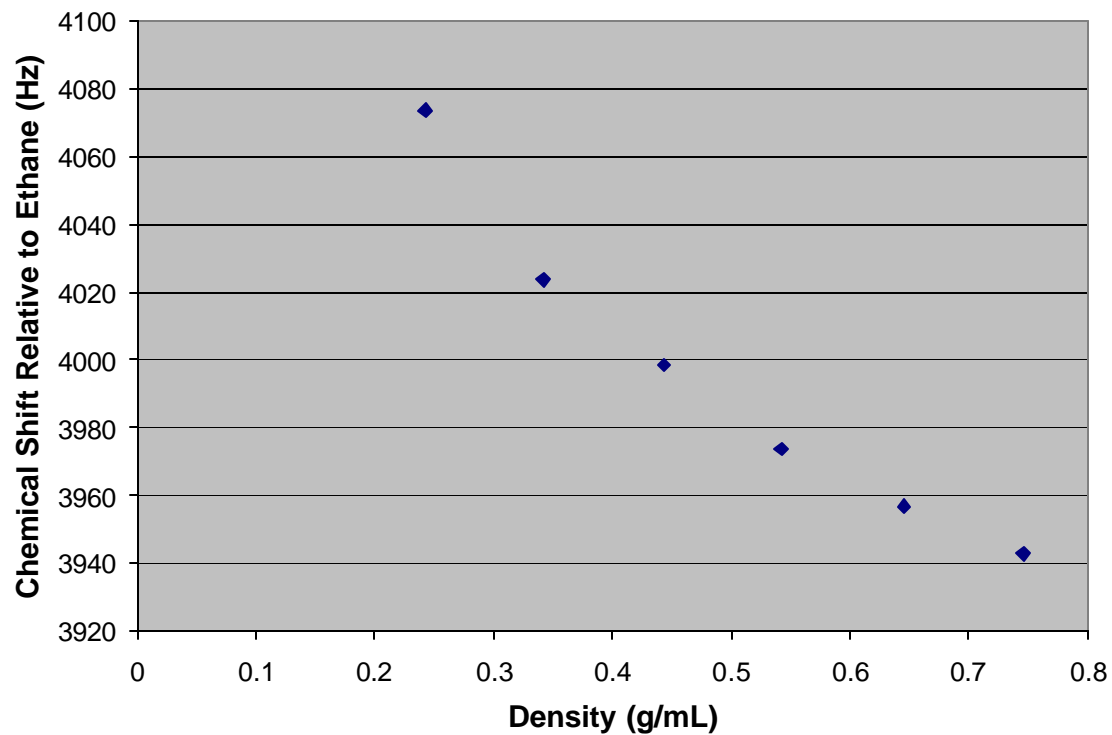


**Figure 3-6** The acid  $^1\text{H}$  chemical shift of formic acid relative to ethane as a function of  $\text{CO}_2$  density at 323 K.

## CHAPTER 4

# HIGH-RESOLUTION IMAGING OF THE SUPERCRITICAL ANTISOLVENT PROCESS

### **Abstract**

A high magnification and high resolution imaging technique was developed for the supercritical fluid antisolvent (SAS) precipitation process. Visualizations of the jet injection, flow patterns, droplets, and particles were obtained in a high pressure vessel for polylactic acid and budesonide precipitation in supercritical CO<sub>2</sub>. Results show two regimes for particle production: one where turbulent mixing occurs in gas-like plumes and another where distinct droplets were observed in the injection. Images are presented to demonstrate the capabilities of the method for examining particle formation theories and for understanding the underlying fluid mechanics, thermodynamics, and mass transport in the SAS process.

### **Introduction**

The supercritical fluid antisolvent (SAS) process is an important means of producing micron range particles and powders of a variety of polymer, pharmaceutical and other materials (Kompella and Koushik 2001, Reverchon and Della Porta 2001, Sun 2002). The use of near-critical and supercritical CO<sub>2</sub> as a processing solvent, or as an antisolvent, presents certain advantages over traditional solvents. In addition to its

adjustable thermophysical properties with changes in temperature and pressure in the near-critical and supercritical region, CO<sub>2</sub> is an attractive process solvent in that it is non-flammable, inexpensive, and nontoxic. Moreover, CO<sub>2</sub> has accessible critical conditions with a mild critical temperature of 31°C and critical pressure of 73.8 bar. However, CO<sub>2</sub> is a feeble solvent for many organic, inorganic, and polymeric materials. As such, it can be used as an effective antisolvent to induce nucleation and growth of a variety of particle materials from traditional solvents. In order to refine the production techniques of nanoparticles and microparticles using supercritical fluid technologies, it is vital to understand the underlying thermodynamics, mass transfer, momentum transfer, precipitation, and particle nucleation and growth mechanisms.

Supercritical fluid CO<sub>2</sub> based precipitations have gained significant attention as means of forming particles of various materials. As an example, Chattopadhyay and Gupta (2000) used the SAS process to form nanoparticles of fullerene with relatively uniform size. Chattopadhyay and Gupta (2003) also used the SAS process to form inorganic silica nanoparticles. In this they used the CO<sub>2</sub> both as an antisolvent to remove the organic solvent and as a reactant to react with the dissolved sodium silicate to form silica particles. However, CO<sub>2</sub> based precipitations are primarily used to form micro-particles of organic and polymeric compounds. Major advantages of these technologies include the tunable and benign nature of CO<sub>2</sub> resulting in single step processes with particularly clean products.

The supercritical antisolvent precipitation (SAS) process involves jet injection of a liquid solvent and dissolved solute, the dispersed phase, into a supercritical fluid, the continuous phase. Supercritical CO<sub>2</sub>, with its poor solvency for many organic, inorganic, and polymeric materials, can be used as a very effective antisolvent to induce controlled precipitation of a variety of materials from solvents in the form of microparticles as well

as other morphologies depending on the materials used and the operating conditions. Compounds that are highly insoluble in supercritical CO<sub>2</sub>, such as polylactic acid (PLA) and budesonide, can be first dissolved in a suitable solvent and then injected into the supercritical CO<sub>2</sub> antisolvent (SAS) through a injection nozzle, precipitating the compound as particles. Key underlying issues of the supercritical antisolvent precipitation process include jet breakup and atomization, mass transfer, nucleation and growth. Operating parameters that impact the particle characteristics include the physical properties of the solute and solvents, temperature, pressures (densities), nozzle diameter, pressure drop across the nozzle, and injection velocities. Variations in these operating parameters affect the thermodynamics, fluid flow properties (jet breakup), mass transfer rates of the solvent, solute, and antisolvent, as well as particle nucleation and growth.

### **Theory**

An understanding of the underlying mechanisms that govern the formation of microspheres in the SAS process is an area of significant interest necessary for further advancement of the technology. The SAS particle production process is a complex one involving the interaction of jet hydrodynamics, droplet formation, mass transfer into and out of the droplets, phase equilibrium, nucleation, and particle growth. To advance our understanding and control of the process, high magnification and high speed imaging of the system and these phenomena would be beneficial. Dixon et al. (1993) points out that imaging these systems is a challenging task using conventional high-pressure cells and imaging equipment.

Several studies have examined the mechanisms of particle formation in the SAS process under various operating conditions leading to regimes controlled by jet breakup

(including both nucleation and diffusion limited situations (Dixon et al.1993, Randolph et al. 1993, Mawson et al. 1996, Werling and Debenedetti 1999, Werling and Debenedetti 2000, and Chavez et al. 2003)) as well as those controlled by nucleation in gas-like plumes (Lengsfeld et al. 2000). Dixon et al. (1993) and Randolph et al. (1993) related the size of the droplets in the injection process to the Weber number ( $We = \rho_A V^2 D / \sigma$ ) which is a ratio of inertial forces to surface tension forces, where,  $\rho_A$  is antisolvent density,  $V$  is the relative velocity,  $D$  is the drop diameter, and  $\sigma$  is the interfacial tension. The interfacial tension between supercritical carbon dioxide and the liquid solvent, such as methylene chloride, quickly decreases upon injection of the liquid. However, Dixon et al. (1993) point out that the interfacial tension is affected by the presence of a dissolved solute and is composition dependent. A large Weber number indicates that jet and drop deforming external forces are large compared to the reforming surface forces, thus leading to drop breakup into smaller droplets. According to Dixon et al. (1993), Randolph et al. (1993) and Lengsfeld et al. (2000), smaller particles should be obtained at higher Weber number.

Dixon et al. (1993) found that for polystyrene precipitated from toluene, initial droplet size and particle size increased as the antisolvent density was decreased as predicted by Weber number analysis. They argued that the solute within a droplet evolves into a single particle because the organic solvent mixes with the supercritical fluid by diffusion. Based on this idea, Mawson et al. (1996) modified the SAS process and injected both the organic solution and the CO<sub>2</sub> antisolvent through a coaxial nozzle. The coaxial spray conditions decreased the Weber number and produced larger droplets and larger particles.

Yet, particle size is not consistently observed to increase with Weber number. Randolph et al. (1993) reported that particle sizes increased modestly with increasing upstream pressure for poly (L-lactic acid) particles precipitated from methylene chloride in SCF CO<sub>2</sub>. They suggest that particle nucleation and growth, rather than initial droplet size, are the major determining factors of particle size. In this theory, within each droplet formed from atomization of the solvent jet, rapid mass transfer of antisolvent and solvent results in high supersaturations for the solute. Lengsfeld et al. (2000) describes that high supersaturation causes rapid nucleation and growth of more than one particle per primary droplet. Because of differences in the solvents and operating conditions used, the Weber number correlation to initial droplet size is not the only determining factor of the resultant particle size.

However, most supercritical fluid studies have shown that only modest changes of particle size and particle size distribution are observed over a significant range of operating conditions. Griffith et al. (1999) and Park et al. (2002) observed little influence of large changes in operating conditions on the mean particle size and particle size distribution of nylon precipitated from formic acid in SCF CO<sub>2</sub>. Lengsfeld et al. (2000) used jet breakup length along with the dynamic surface tension to explain the limited dependence of the SAS process on various process parameters. They demonstrated that the surface tensions of miscible solvents in CO<sub>2</sub> diminished at very short distances from the nozzle outlet, resulting in the absence of distinct droplets. Consequently, no significant change in the average particle size and particle size distribution upon changing operating conditions was observed. Under these conditions microparticles are formed by mixing between gaseous shear layers that occur due to the rapid dissipation of surface

tension, without the formation of discrete droplets. The presence of a solute was neglected in order to simplify the calculations. However, a solute can significantly alter the surface tension.

The solution-enhanced dispersion by supercritical fluids (SEDS) process developed by York and Hannah (1996) uses a coaxial nozzle in which the solution and antisolvent are mixed turbulently prior to entering the high-pressure vessel. By using high flow rates to raise the Weber number and the Reynolds number, Shekunov et al. (1999, 2001) obtained macroscale images of the particle formation in the absence of distinct droplets. Their observations and calculations support the notion that the particles form by diffusion-enhanced turbulent mixing.

Werling and Debenedetti (1999, 2000) presented a mathematical model for the mass transfer between an isolated solvent droplet and an antisolvent continuum ranging from subcritical (1999) to supercritical (2000) mixture regimes. They investigated the effect of process conditions on the time scales for mass transfer showing that lower pressures and larger initial radii result in longer droplet lifetimes in two-way diffusion of solvent and antisolvent. For the subcritical mixture regime, the droplets swelled, but for the supercritical mixture regime, the effective droplet radius increased if the organic solvent density was greater or decrease if the antisolvent density was greater. The studies provided valuable insight into the environment to which a solute is exposed within the precipitation process.

Chavez et al. (2003) estimated the characteristic times of processes involved in SAS particle formation in the two-phase regime for a typical solvent (ethanol) and antisolvent (CO<sub>2</sub>) by using engineering correlations and a linear jet breakup model. Their

calculations suggest that for low jet velocities, the characteristic time for mass transfer of the antisolvent into the liquid droplet is two orders of magnitude larger than the characteristic time for the development of the hydrodynamic jet instability. Thus, only a small amount of the antisolvent is present in the solvent by the time the jet breaks up, supporting the assertions used by Werling and Debenedetti (1999, 2000). Nucleation times were shown to vary over a wide range and depend on the supersaturation, which is a function of process conditions. These studies provide valuable insight into the controlling mechanisms for the SAS process, but the ability to directly observe the jet structure, hydrodynamics, droplet and particle evolution would greatly aid the understanding of this process.

The presence of small particles and the desire to image them complicates an already difficult task of imaging an injection process. Many researchers have used imaging and visualization techniques to study jet flows, atomization, and droplets; a number of systems are reviewed by Lefebvre (1989), Chigier (1991), and Liu (2000). Imaging system components (cameras, lenses, and lighting) must be selected to handle length scales ranging from millimeters (jet lengths, spray widths) to micrometers (drop and particle sizes). Light sources, frame rates, and exposure times must capture drops and particles traveling at hundreds of meters per second. For SAS precipitation, microscopy-base imaging offers the advantage of examining the dynamic process that leads to particle formation, though a limitation is the inability to image particles that approach the nanometer scale.

Several studies used particle and droplet visualization in supercritical fluids. Kerst, Judat, and Schlunder (2000) imaged falling films and free jets in a high pressure

view cell with a camera with a 90mm macro lens to investigate the flow regimes. Mayer and Tamura (1996) used a shadowgraph setup to visualize injection, spray formation, and supercritical mixing for liquid oxygen/gaseous hydrogen propellants. Luo et al. (2001) visualized a liquid jet of acetone and ethanol injected into supercritical carbon dioxide. Shekunov et al. (2001) imaged particle formation in a jet to illustrate nucleation and growth of paracetamol crystals. Each of these techniques imaged the processes on a macro-scale and did not investigate individual particle or droplet formation at high magnification and high resolution. Fang and Kozinski (2001) used optical and infrared microscopy and digital image analysis to study phase changes of benzo(a)pyrene in supercritical water combustion. Marioth et al. (2000) used a three-wavelength-extinction technique to measure droplets and particles formed in supercritical carbon dioxide. Armellini and Tester (1994) conducted flow experiments simulating the rapid precipitation of salts during the supercritical water oxidation (SCWO) waste treatment process and used in situ laser transmission measurements. Extensive research has been done using SEM to evaluate size and morphology of particles formed under supercritical conditions (e.g. Randolph et al. (1993), Martin (2000), Dixon et al. (1993), Mawson et al. (1996), Bleich et al. (1993), Shekunov et al. (1999, 2001), Armellini and Tester (1994)). A limitation of SEM analysis is that it is applied to particles after they have been removed from the dynamic system. Chen and Basaran (2001) employed an ultra high speed imaging system to investigate formation dynamics of drops ejected from a drop-on-demand nozzle (associated with ink-jet printing). Notz et al. (2000) used an ultrafast digital imaging system to view drop formation from a tube. Wilkes et al. (1999) imaged

growth and detachment of drops from a capillary tube with a high speed imager, producing silhouette images of the drop.

While these visualization techniques provided information for the study of momentum transfer and properties of the jets, drops, and particles, other techniques are needed to provide information on solvent and solute concentration and mass transfer rates in these systems.

## **Description of experiments**

### SAS Apparatus

The experimental setup used for the SAS process was a modification of that used by Martin et al. (2000, 2002), which consists of a liquid solution vessel, a metering pump, a pulse dampener, an in-line pressure gauge, a rupture disk, a capillary tube inside of a 1/8" stainless shield tubing sheath, a precipitation chamber equipped with a temperature gauge, an RTD thermocouple connected to a temperature controller, and strip heaters. A schematic diagram of the system is given in Figure 4-1. Pure acetone, pure methylene chloride, or an organic solution consisting of either budesonide or PLA dissolved in methylene chloride flows into the top of the precipitation chamber (Jerguson, model 19TM40). The volume of the precipitation chamber (PC) is approximately 80 mL. The chamber has two acrylic windows allowing observation during the experiment. The chamber sits approximately 64 cm tall including the base and it is approximately 14.6 cm deep from front to back. The liquid solution was delivered into the top of the precipitation chamber at a constant flow rate using a metering pump (Acuflo Series II). A pulse dampener (Scientific Systems Inc., model 12-0625) was used in series to

minimize fluctuations in the upstream pressure. The solution entered the vessel via a tube injection nozzle. The inner tube of the injection nozzle was 100  $\mu$ m ID fused silica capillary tubing (Alltech, Part No. 1900331). The capillary tubing extended approximately 66 mm into the precipitation chamber further than the stainless steel outer tubing sheath. The capillary tubing was connected to stainless steel tubing (1/16" HIP rated to 1034 bar) using Valco adapters (Models EZRU21 and ZU1T). A metal collar was installed to prevent breakage of the exposed capillary tubing and to hold the adapters together. Graphite ferrules (Alltech, RF-100/0.4-G) were used as seals for the capillary tubing. A digitally controlled high pressure syringe pump (Isco, model 500D) delivered the carbon dioxide antisolvent to the chamber at the desired operating temperature and pressure. Two analog pressure gauges (McDaniel Controls) were used on the inlet line and on the vessel itself. A rupture disk was used as a safety precaution to prevent the pressure from exceeding 310 bar. An RTD probe was used inside the precipitation chamber to measure temperature. The precipitation chamber temperature was controlled using two 250 W strip heaters connected to a temperature controller (Omega CSC 32) to allow even heating of the chamber. The strip heaters were attached to the sides of the vessel using two C-clamps.

#### Imaging System Apparatus

Components of the imaging system are shown in Figure 4.1. A COHU 2122 industrial high resolution monochrome video camera (CCD) was used. The CCD has 768 x 494 pixels, with a pixel size of 8.4 x 9.8  $\mu\text{m}^2$ . The shutter speed was 60 frames per second and a Nova-Strobe DA Plus stroboscope set at 60 flashes per second was used for backlight illumination. A PC and Dazzle software were used for digital video capturing,

editing, and compression. CCD output was sent to a monitor for viewing. A Questar QM 100 MK III Long Distance Microscope Lens (Astro-Optics Division of Company Seven, [www.company7.com](http://www.company7.com)) was used. The lens working distance ranges from 8 to 35 cm allowing visualization in the high pressure SAS vessels. The lens Power Pak attachment (a 3 X Barlow lens and an aplanat lens) allows observation of sub-micron characteristics. The Questar is equipped with both motorized and manual focus. The camera and lens assembly is mounted on a vertical rail system and an X-Y stage to allow precise positioning.

### Materials

Poly (L-lactic acid) (PLA) with an average molecular weight of 100,000 was purchased from Birmingham Polymers. Budesonide (99 + %) was purchased from Sigma-Aldrich. Methylene chloride and acetone were used as received from Fischer Scientific without degassing. Carbon dioxide (SCF grade) was purchased from BOC Gases.

### Procedure

The precipitation chamber was filled with carbon dioxide using the ISCO syringe pump and time was allowed to reach the desired operating temperature and pressure. The organic solution was then injected through the nozzle with a pressure drop of 34 bar into the chamber for several minutes; however the injection process was usually fully developed within the first 60 seconds. After each injection, the contents of the vessel was vented into the fume hood, removing the residual solvent. The precipitation chamber was flushed with CO<sub>2</sub> to clean the vessel between experiments. Multiple sets of images from several processes were captured at four positions along the height of the precipitation chamber during the injection process. Figure 41 illustrates the field of views for

positions along the precipitation chamber at different distances from the injection nozzle. Position 1 is at the nozzle tip, position 2 is 13 mm down from the nozzle tip, position 3 is 23 mm down from the nozzle tip, and position 4 is 43 mm down from the nozzle tip. Experiments were performed by flowing pure acetone, pure methylene chloride, a 1 wt% solution of PLA in methylene chloride, a saturated solution of PLA in methylene chloride, and a 1 wt% solution of budesonide in methylene chloride into the carbon dioxide antisolvent. The experimental conditions used are summarized in Table 3-1. Three magnification levels were used. Most visualizations were obtained with a magnification of approximately 1.28  $\mu\text{m}$  per pixel. The horizontal field of view is 1.31 mm and the vertical field of view is approximately 0.98 mm. A higher magnification of the lens and camera for this system was 0.901  $\mu\text{m}$  per pixel. With this magnification the horizontal field of view was 921  $\mu\text{m}$  and the vertical field of view was 691  $\mu\text{m}$ . The highest magnification used was achieved with the Power Pak lens combination to the lens. While this addition greatly increased the magnification, the image clarity was reduced. The magnification using this combination was approximately 0.21  $\mu\text{m}$  per pixel. The horizontal field of view was approximately 214  $\mu\text{m}$  and the vertical field of view was approximately 160  $\mu\text{m}$ . The CCD recorded video images at 60 frames per second from just before the metering pump was started and the top valve in the precipitation chamber was opened. Jet width was determined from images by measuring a horizontal line across the jet. The jet breakup length was measured as the distance from where the jet emerges from the nozzle to the point where the jet begins to pinch and droplets begin to form. The jet pinch is the point where the straight jet edge begins to form ripples.

## Visualization Results

Approximately five minutes of video were obtained at high magnification at each of the four vessel positions for each of the six injection conditions listed in Table 3-1. Video files are available from the authors. Selected still images from the video are displayed in Figures 4-2 through 4-7. Still images for the injection of pure acetone into liquid carbon dioxide at the different positions in the chamber are shown in the first column in Figure 4-2. The magnification is approximately  $1.28\ \mu\text{m}$  per pixel. (A scale is shown at the bottom of each column of images.) No droplets were apparent during the injection of acetone into carbon dioxide under these high-density conditions. Streaky patterns that moved as waves were clearly visible in the vessel at positions below the nozzle. The second column of Figure 4-2 shows an image taken at position 4, 20 seconds after the injection of acetone in high-density supercritical carbon dioxide. There were no droplets, but waves were observed that are very similar to the injections in liquid  $\text{CO}_2$  at similar density.

Column three of Figure 4-2 shows images of pure methylene chloride injected into supercritical carbon dioxide. A stable jet was observed at position 1. It had a width of approximately  $78\ \mu\text{m}$  and a breakup length of  $0.64\ \text{mm}$ . Droplet formation was observed at all positions below the nozzle tip. The image at position 3 shows two spherical droplets with diameters of approximately  $70\ \mu\text{m}$ , which is near the measured value of the jet width. Position 4 has a wide range of droplet sizes.

A solution of 1 wt% PLA in methylene chloride was injected into supercritical carbon dioxide. Images of the precipitation process at each position in the vessel using  $1.28\ \mu\text{m}$  per pixel magnification are shown in the first column of Figure 4-3. At position

1, the jet width is approximately 111  $\mu\text{m}$ . The bright circles seen near the jet are drops that separated from the jet just below the nozzle exit. The separated drops were in a conical formation and they were all similar in size (35 to 65  $\mu\text{m}$  in diameter). At position 2, the bulk liquid disintegrated into droplets. Again, the drops were similar in size. Images at position 3 show non-spherical as well as spherical droplets of differing diameters. At position 4, there was a wide range of droplet sizes but there were also image features that had solid or granular characteristics. We believe these to be polymer microparticles. It is important to note that the high magnification results in a thin depth of field; drops and particles that are not in the focal plane are blurred.

The second column of Figure 4-3 shows images using the 0.9  $\mu\text{m}$  per pixel magnification for the injection of the 1 wt% PLA in methylene chloride into supercritical  $\text{CO}_2$ . At position 1, the width of the jet here was approximately 90  $\mu\text{m}$  and several droplets were seen separating from the jet. A slight decrease in image clarity is due to the increase in magnification. At position 2, there were spherical droplets with a wide range of diameters from 25 to 175  $\mu\text{m}$ . At position 3, we saw both spherical droplets and solid particles. The center portion of the image suggests particle agglomeration around a droplet. At position 4, two very large droplets were seen. No particles were visible as this frame was from very early in the injection.

The magnification was increased to view the solid particle formations and droplet formations more closely under the same conditions. The third column in Figure 4-3 shows images of the 1 wt% PLA in methylene chloride solution injected into supercritical  $\text{CO}_2$  using the 0.21  $\mu\text{m}$  per pixel magnification. The width of the jet at position 1 was approximately 83  $\mu\text{m}$ . Three small separated droplets (5 to 7  $\mu\text{m}$  in diameter) are seen on

the left side of the jet. The frame at position 2 contained partial images of large spherical droplets, on the far left and far right portions. A small spherical droplet was seen at the top middle portion of the image. The right portion of the image from position 3 shows a spherical droplet with a diameter of 95  $\mu\text{m}$ . Just below the droplet is a small spherical droplet approximately 18  $\mu\text{m}$  in diameter. Droplets larger than the field of view were also seen. This indicates that there is a very wide range of drop sizes present in this process. The image at position 4 shows a droplet with a diameter of 50  $\mu\text{m}$  in the lower right portion of the image. Above the droplet appears to be three particles with diameters around 3  $\mu\text{m}$ .

The effect of changing the solute concentration was examined by using a saturated solution of PLA in methylene chloride. Images at the 1.28  $\mu\text{m}$  per pixel magnification for the solution injected into  $\text{CO}_2$  are shown in Figure 4-4. At position 1, the width of the jet is approximately 89  $\mu\text{m}$ . Many fine droplets were seen immediately after the solution exits the nozzle tip. There were significantly more droplets at this point in the saturated solution than in the 1 wt % solution of PLA in methylene chloride. At position 2, we saw many non-uniform spherical droplets. They range in diameter from 50 to 223  $\mu\text{m}$ . These images are very similar to the 1 wt % solution images taken at position 4. The breakup of the jet is in a conical formation. The breakup occurred at a short distance from the nozzle discharge.

Images of the same process under high magnification are shown in the second column of Figure 4-4. The jet width at position 1 was approximately 88  $\mu\text{m}$ . Several spherical droplets, with diameters of approximately 20-30  $\mu\text{m}$  separated from the jet. At position 2, there are several spherical droplets with diameters ranging from 55 to 225  $\mu\text{m}$ .

There were also many fine solid particles that appear to be uniform in size. A spherical droplet surrounded by particle agglomerates is seen in the lower middle portion of the image.

To examine a different type of particle precipitation, a 1 wt% solution of the corticosteroid, budesonide, in methylene chloride was prepared. Budesonide, a low molecular weight organic pharmaceutical molecule, provides contrast to the high molecular weight PLA polymer material. Images from the injection of the 1 wt% budesonide in methylene chloride solution into supercritical CO<sub>2</sub> are shown in Figure 4-5. At position 1, the image shows a jet breakup length of 0.61 mm as well as an interesting swirl pattern behind the jet. At positions 2, there are several non-spherical droplet formations. Position 3 shows several spherical droplets of different diameters as well as a multitude of fine budesonide particles around them. The particles ranged in size from 3 to 12 μm in diameter. Position 4 shows large droplets still present along with an agglomeration of fine particles. Images of this process under high magnification are shown in the second column of Figure 4-5. At position 1, the width of the jet is approximately 95 μm. Several droplets were seen emerging from the jet on the left side of the image. At positions 2 and 3, a few spherical droplets were seen in focus. These droplets vary widely in size from 37 to 270 μm. At position 4, several solid particles and a larger formation which we attribute to agglomerated particles were observed. A spherical droplet with a diameter of approximately 90 μm is seen in the middle of the image.

## Discussion

The images of acetone injected into dense CO<sub>2</sub> showed streaks and waves, but no drops. This is evidence for miscible liquids that had not yet fully mixed, with the pure phases of each liquid differing slightly in refractive index. Others have shown similar patterns for jet flows and the waves have been used to indicate turbulence (Liu 2000). The flow patterns for the two acetone experiments, although the temperature and pressure were quite different, were similar because the CO<sub>2</sub> densities were very similar. These experiments indicate that SAS conditions exist such that no distinct droplet formation occurs.

Lengsfeld et al. (2000) describe that carbon dioxide is completely miscible with methylene chloride at 82.7 bar and 40 °C, resulting in a dynamic surface tension that decreases rapidly toward zero upon injection into CO<sub>2</sub>. Therefore, they indicate that the injection of methylene chloride into supercritical carbon dioxide behaves in a gas-like manner, and that distinct droplets never form. However, the spherical droplets observed in these experiments illustrated that under these conditions, distinct droplets formed despite the rapidly diminishing surface tensions. It is important to note that the injection conditions here are different than those used by Lengsfeld (2000). The spherical droplets at position 3 had approximately the same diameter as the jet width consistent with Rayleigh jet breakup where droplet diameters are approximately the same as the jet diameter. However, images at other lapse times and positions show drops with varying sizes.

Atomization in the form of a cone of separating drops as well as the bulk liquid disintegrating into droplets was clearly observed for the injection of 1 wt% PLA

dissolved in methylene chloride into supercritical CO<sub>2</sub>. The higher magnification images of the jet formation show separated drops much smaller than the jet width indicative of the early stages of atomization (Lefebvre 1989, Liu 2000). Conical jets were observed when injecting the saturated solution of PLA and when injecting the 1 wt% solution. Overall, there were no significant differences between the 1 wt % PLA solution and the saturated solution other than an increase in droplet formation at the beginning of the jet. The images for the experiment with saturated PLA dissolved in methylene chloride display PLA particle agglomerations resulting from the precipitation process. Similar agglomeration has been observed by SEM analysis of recovered products by Dixon et al. (1993). As would be expected due to the higher PLA concentration, there were many more particles visible for the saturated solution than for the 1 wt% solution.

Martin (2000, 2002) demonstrated that processing budesonide particles with this antisolvent technique significantly reduced particle agglomeration. Uniform particle size distributions with mean diameters of 1 to 2 μm were produced by Martin (2000, 2002) with the same operating conditions used in this study for budesonide in methylene chloride solutions injected into CO<sub>2</sub>. It is apparent from the images of the budesonide in methylene chloride experiments that the droplet size during formation is not uniform, ranging in diameters from 30 to 334 μm. Given the uniform budesonide particle size distribution obtained from this system (Martin 2000, 2002), this would indicate that the particle size is not controlled entirely by the size of the droplets.

Some qualitative dynamic information can be drawn by examining images from different times during an injection. Figure 4-6 shows the development of the flow pattern at the nozzle for a 1 wt% PLA solution injected into supercritical CO<sub>2</sub>. When the flow is

initiated, the pressure drop across the nozzle is larger than the steady-state pressure drop during the process. The top image shows the initial emergence of the jet from the nozzle. It is conical indicating the large exit velocity resulting from the high pressure drop. After 0.33 seconds, the second image shows a narrower, less intense cone and the emergence of a central jet core. By 1.0 seconds, the third image shows a stable jet flow. This indicates that images taken more than one second into the process are representative of a fully developed flow.

Figure 4-7 shows images of the injection of a 1 wt% solution of PLA in methylene chloride at various times during the process at position 4. The image at 0.25 seconds shows the first observed droplet. Waves are clearly visible in the background as is a streak pattern trailing the droplet. The second image from 7.6 seconds shows droplets of various sizes, but still no particles are observed. The last image from just over 20 seconds into the injection shows both very large and very small droplets as well as a large number of small particles.

To quantify injection characteristics, droplets were sized at each position away from the nozzle for a 1 wt% solution of PLA injected into supercritical CO<sub>2</sub>. The diameters of droplets in ten frames at each position were measured by using the magnification. The ten frames were selected to be 4.5 seconds into the flow. The mean and standard deviation of drop diameters at each position are listed in Table 3-2. For these conditions, the droplets increase in size as they move away from the nozzle tip. The standard deviations show a large distribution of droplet sizes at all positions, further indicating that the uniform particle distributions obtained in these systems may not be controlled by droplet size and distribution. The observation that the droplets increase in

size as they move away from the nozzle is in agreement with the theory proposed by Randolph et al (1993). Particles can be precipitated by CO<sub>2</sub> diffusion into the droplets thereby swelling the droplets and diminishing the solvent strength to the point of supersaturation. Interestingly, Werling and DeBenedetti (1999, 2000) show that, depending on the thermodynamics of the system, droplets can either swell or shrink as they move away from the nozzle. In either case, the solvent strength is decreased, leading to supersaturation.

### **Evaluation and Capabilities of Visualization Technique**

The optical technique provides the ability to visualize mixing occurring between two fluids with different refractive indices. Examples are the waves and streaks seen in the pure acetone injections and the swirling patterns trailing methylene chloride droplets. The images show that the optical system has the capability of visualizing fast moving droplets and particles at magnifications of less than one  $\mu\text{m}/\text{pixel}$ , though resolution and depth of field issues decrease image clarity at the maximum system magnification of 0.21  $\mu\text{m}/\text{pixel}$ .

The technique allowed the observation of droplets ranging from 2 to 350  $\mu\text{m}$ . Drops and particles smaller than two microns were indistinguishable because of system resolution. The ability to identify and characterize these small formations drives future system improvements including lighting enhancements, laser induced fluorescence, and higher spatial resolution CCD cameras.

Particles were observed in the precipitation processes, but we could not observe the crystallization for an individual particle or the dissolution of a droplet. We are currently imaging the precipitation process at 1000 frames per second to be able to track

individual droplets as they move through the field of view in an attempt to capture particle formation events.

Large variations of droplet sizes at all distances from the nozzle tip were observed. However, the particles formed in this process had a uniform size distribution. At this point, it is unclear exactly what this implies about the particle formation process except that there is not a direct correlation between droplet size and distribution and particle size and distribution.

## **Conclusions**

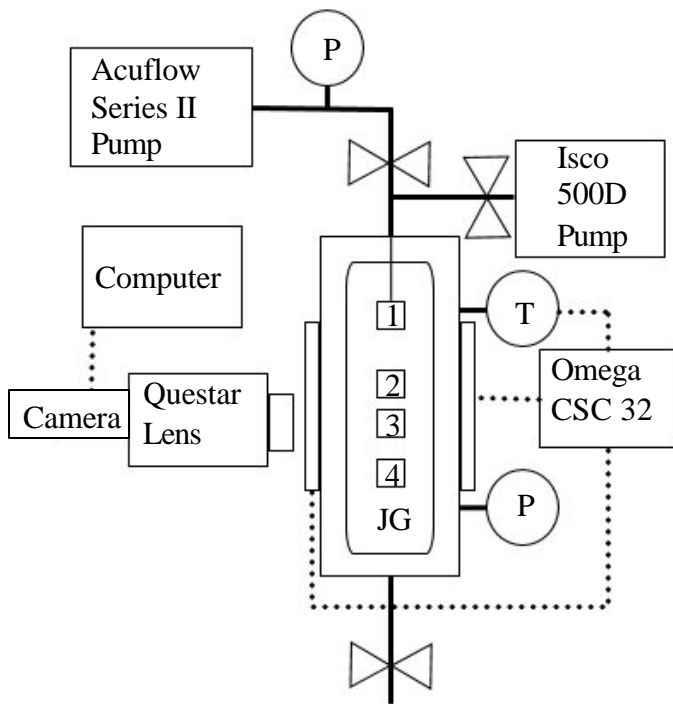
A technique for the visualization of particle formation processes in supercritical fluids was developed. Visualization of the PCA process with high magnification and high resolution allowed for the observation of particles and droplets. Images were captured that provided information on jet breakup, particles, particle agglomeration, droplet size and morphology, and jet flow phenomena. The jet breakup length was measured in several experiments, as were droplet and particle diameters. The system is capable of achieving magnifications (ranging from 1.28  $\mu\text{m}$  per pixel to 0.21  $\mu\text{m}$  per pixel) and resolutions for imaging high pressure particle production processes for study of the system dynamics.

Although image processing and further experiments are needed to make quantitative conclusions, there are several observations of importance. First, we observed conditions in which no droplets formed (high  $\text{CO}_2$  densities). Particles were formed in this kind of process, and therefore were the result of nucleation and growth within gas-like shear layers, as suggested by Lengsfeld (2000). At low  $\text{CO}_2$  densities, however, we observed droplet formation that occurred by atomization as predicted by Dixon et al.

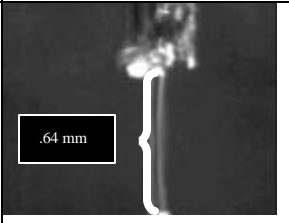
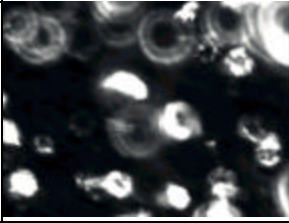
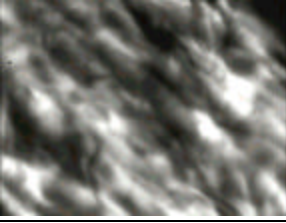
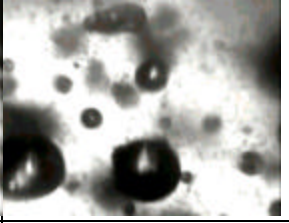
(1993) and Randolph et al. (1993). Although a relatively uniform particle size distribution was obtained for PLA, our images showed a wide range of droplet sizes at several positions in the jet injection. These results show that there is not a direct correlation between droplet size and distribution and particle size and distribution. In some cases, especially for budesonide solutions injected into CO<sub>2</sub>, non-spherical droplets were observed indicating the effect of viscous forces. The video (time sequence images) allowed us to observe that the flow developed very quickly. For the 1 weight percent solution of PLA, the injection was fully developed after 1 second. Our measurements of droplet sizes showed that droplets swelled as they moved away from the nozzle as predicted by Randolph et al (1993) and Werling and Debenedetti (1999). Again, a very large range of droplet sizes at each position was observed. This paper displayed the capabilities of this technique to examine the underlying fluid mechanics, mass transport and thermodynamics that control the SAS process.

### **Acknowledgements**

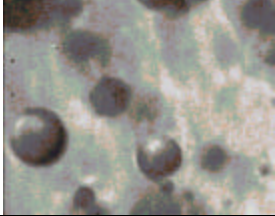
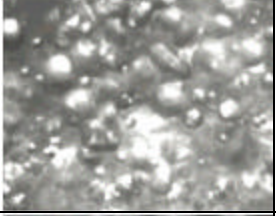
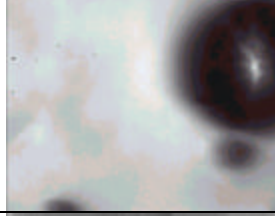
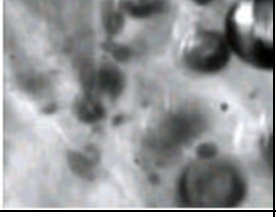
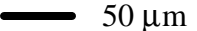
Financial support from the National Science Foundation (CTS-0207781) is gratefully acknowledged.



**Figure 4-1** SAS apparatus and imaging equipment used in precipitation experiments. JG is the Jerguson gauge high pressure view cell.

	Pure acetone into liquid CO <sub>2</sub>	Pure acetone into high pressure (P = 172 bar) supercritical CO <sub>2</sub>	Pure methylene chloride into supercritical CO <sub>2</sub>
Position 1 At nozzle tip Various times during injection			
Position 2 13 mm from nozzle tip Various times during injection			
Position 3 23 mm from nozzle tip Various times during injection			
Position 4 43 mm from nozzle tip Various times during injection			
Magnification Scale	— 100 μm	— 100 μm	— 250 μm

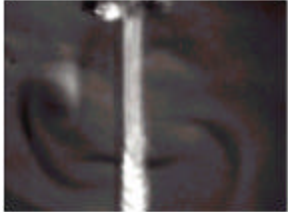
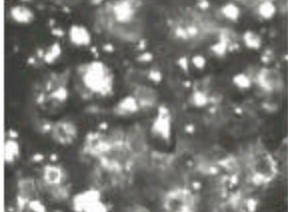
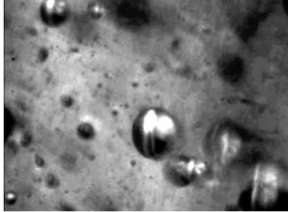
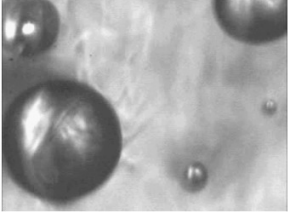
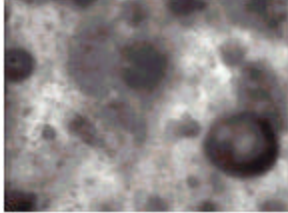
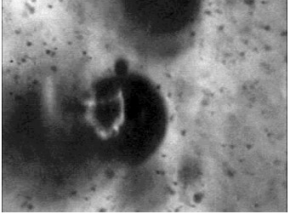
**Figure 4-2** Still images of the injection of pure liquid solvents, acetone and methylene chloride, into supercritical CO<sub>2</sub> at various times and positions.

	SAS - 1 wt% poly (L-lactic acid) in supercritical CO <sub>2</sub>	SAS - 1 wt% poly (L-lactic acid) in supercritical CO <sub>2</sub> at high magnification	SAS - 1 wt% poly (L-lactic acid) in supercritical CO <sub>2</sub> with Power Pak
Position 1 At nozzle tip Various times during injection			
Position 2 13 mm from nozzle tip Various times during injection			
Position 3 23 mm from nozzle tip Various times during injection			
Position 4 43 mm from nozzle tip Various times during injection			
Magnification Scale	 250 μm	 100 μm	 50 μm

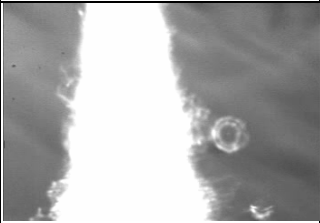
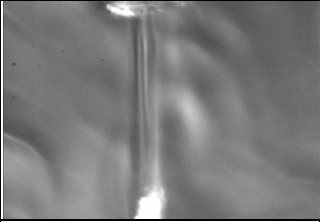
**Figure 4-3** Still images of the injection of 1 wt% PLA solution in methylene chloride into supercritical CO<sub>2</sub> at various times and positions using three different magnifications.

	SAS - Saturated poly (L-lactic acid) in supercritical CO <sub>2</sub>	SAS - Saturated poly (L-lactic acid) in supercritical CO <sub>2</sub> at high magnification
Position 1 At nozzle tip Various times during injection		
Position 2 13 mm from nozzle tip Various times during injection		
Magnification Scale	 250 μm	 100 μm

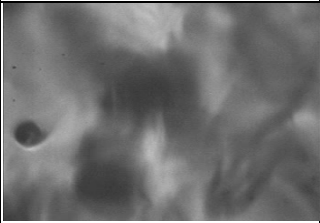
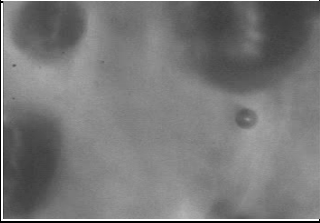
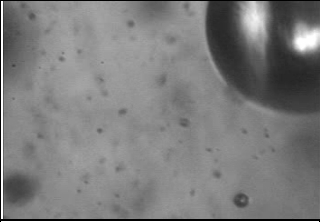
**Figure 4-4** Still images of the injection of a saturated PLA in methylene chloride solution at various times and positions using two different magnifications.

	SAS - 1 wt% budesonide in supercritical CO <sub>2</sub>	SAS - 1 wt% budesonide in supercritical CO <sub>2</sub> at high magnification
Position 1 At nozzle tip Various times during injection		
Position 2 13 mm from nozzle tip Various times during injection		
Position 3 23 mm from nozzle tip Various times during injection		
Position 4 43 mm from nozzle tip Various times during injection		
Magnification Scale	 250 μm	 100 μm

**Figure 4-5** Still images of the injection of 1 wt% budesonide in methylene chloride solution at various times and positions using two different magnifications.

	SAS - 1 wt% poly (L-lactic acid) in supercritical CO <sub>2</sub>
Position 1 At nozzle tip At t = 0 sec (when injection began)	
Position 1 At nozzle tip At t = 0.33 sec	
Position 1 At nozzle tip At 1 sec	
Magnification Scale	 250 μm

**Figure 4-6** Still images at three different times at the nozzle showing the injection development for a 1 wt% solution of PLA injected into supercritical CO<sub>2</sub>.

	SAS - 1 wt% poly (L-lactic acid) in supercritical CO <sub>2</sub>
Position 4 At t = 0.25 sec	
Position 4 At t = 7.60 sec	
Position 4 At t = 20.35 sec	
Magnification Scale	— 100 μm

**Figure 4-7** Still images at three different times at position 4 showing the development of droplets and particles observed with time.

Solution	Temperature (°C)	Pressure (bar)	Flowrate (mL/min)
Pure acetone	23	82.7	4.0
Pure acetone	40	172	4.0
Pure methylene chloride	40	82.7	4.0
1 wt% PLA in methylene chloride	40	82.7	1.6
Saturated PLA in methylene chloride	40	82.7	1.6
1 wt% budesonide in methylene chloride	40	82.7	1.6

**Table 4-1** Summary of experimental conditions used in the SAS visualization experiments.

Position	Average droplet size ( $\mu\text{m}$ )	Standard deviation ( $\mu\text{m}$ )	Number of droplets
Position 2	24	17	430
Position 3	30	24	124
Position 4	44	25	125

**Table 4-2** Droplet size distributions ( $\mu\text{m}$ ) for 1% PLA in methylene chloride at 4.5 sec at various positions.

CHAPTER 5  
POLYMERIZATION AND PRECIPITATION DURING THE SUPERCRITICAL  
ANTISOLVENT PRECIPITATION PROCESS

**Abstract**

Two novel one-step polymerization and separation techniques taking advantage of the unique solvent characteristics of supercritical carbon dioxide are discussed. The polymerization of caprolactam is initiated by reaction with CO<sub>2</sub> in the supercritical antisolvent precipitation process. A model for the mass transport in this polymerization process is also developed. A second polymerization is a sonication induced free radical polymerization of methacrylic acid in the supercritical antisolvent process with enhanced mass transport made possible by the solubility of methacrylic acid in CO<sub>2</sub>. Unfortunately, low product yields and reproducibility problems have limited the development of these two polymerization processes beyond these preliminary results. More experiments must be performed to more completely explore these processes.

**Introduction**

Polymerization of caprolactam is a common method for producing Nylon 6 (polycaprolactam). The method of initiation commonly used is a ring-opening step that occurs when water is added to the caprolactam (Agrawal et al., 2001). This reaction is shown in Figure 5-1. Once the ring is opened, the complex can react with caprolactam

molecules or with other ring-opened structures. An alternate method for opening the ring is reacting caprolactam with dense carbon dioxide (CO<sub>2</sub>). CO<sub>2</sub> is known to react with primary, secondary, and tertiary amines (Riley et al., 1994; Teramoto et al., 1997). Because caprolactam has a secondary amine group, CO<sub>2</sub> will react with caprolactam to form a reactive intermediate, either a zwitterions (Danckwerts, 1979) or a loosely-bound encounter complex (Crooks and Donnellan, 1989). These intermediates then react with other caprolactam molecules to begin the polymerization.

The combination of our improved understanding of specific interactions with CO<sub>2</sub> and the supercritical antisolvent (SAS) precipitation process has led to a method for both polymerizing and precipitating the formed polymers in one step without the need to further remove solvent from the polymer. This method involves the spraying of a polymer solution into a supercritical solvent, such as CO<sub>2</sub>, in which the sprayed solvent is soluble, but the dissolved polymer is insoluble (Dixon et al., 1993). Depending on the operating conditions, the sprayed solution breaks up into droplets. At the droplet interface, diffusion of the CO<sub>2</sub> into and diffusion of the organic solvent out of these droplets occurs until the polymer becomes insoluble and precipitates. By modifying the traditional SAS approach, a monomer may be introduced into CO<sub>2</sub> by first dissolving it in another solvent and then spraying it into the supercritical fluid. During the spray process, the monomer polymerizes and precipitates (Owens et al., 2002, 2003). While the work of Owens et al. uses photoinitiated polymerization, a reactive ring-opening polymerization, such as the formation of Nylon 6 is also possible. Caprolactam is slightly soluble in supercritical CO<sub>2</sub> (Laitinen and Jantti, 1996), while Nylon 6 is insoluble, making the polymer precipitate upon formation.

A second method of polymerization and precipitation during the SAS process involves the formation of polymethacrylic acid (PMAA) during the spray process. PMAA is made from a radical polymerization of the monomer, methacrylic acid (MAA). Because MAA is a liquid carboxylic acid, it exhibits some solubility in CO<sub>2</sub> and does not require an organic solution, but may be sprayed into the CO<sub>2</sub> directly. Instead of using an alternate method of initiation, such as a photoinitiator exposed to light, the free radical is formed by sonication in the solution. Sonication has been shown to be effective in producing free radicals both in liquid solution and in dense CO<sub>2</sub> (Kemmere et al., 2004; Kojima et al., 2001). Because the process uses sonication, this process is actually supercritical antisolvent precipitation process with enhanced mass transfer (SAS-EM) (Chattopadhyay and Gupta, 2001a; Chattopadhyay and Gupta, 2001b; Chattopadhyay and Gupta, 2002; Thote and Gupta, 2005). Polymerization in this process is completely new and shows promise for making solvent-free polymers with adjustable molecular weight dependent upon the CO<sub>2</sub> density. This chapter will discuss these two polymerizations which occur during the SAS process.

## **Experimental Methods**

### Materials

ε-caprolactam (Aldrich, 99+%), nylon 6 (Aldrich), dichloromethane (Fisher Scientific), titanium dioxide (Nanophase), methacrylic acid (Aldrich), and carbon dioxide (Airgas, 99.9%) were used as received.

## Apparatus

Figure 5-2 shows the experimental apparatus used in the polymerization experiments. P1 is a computer controlled syringe pump (ISCO 260D) which is maintained at constant temperature by a water bath. P1 delivers CO<sub>2</sub> to an 80 mL reaction vessel, R, immersed in a water bath to control the temperature. A second pump, P2, is a hand pump (HiP) used to deliver the monomer solution to the reaction vessel through a 25 cm capillary nozzle with a 100 μm diameter orifice. The system is continuously vented through a 0.2 μm PTFE filter (Millipore) connected to the exit to collect any polymerization product as it is formed. Also connected to the reaction vessel is an ultrasonic horn controlled by an external ultrasonic processor (Sonics and Materials Inc., 600 W), which is used in the polymerization of MAA in the SAS-EM process. All fluid connections were made with 1/16" stainless steel tubing and high pressure needle valves (HIP, Inc.).

## Procedure

For all polymerization experiments, the reaction vessel was filled with CO<sub>2</sub> from the syringe pump at 4000 psi and 313 K and equilibrated in the water bath at 313 K. The exit valve was adjusted so that the vessel was purged with fresh CO<sub>2</sub> at a rate of 1 mL/min. For the polymerization of caprolactam, the hand pump was then used to inject a 1 wt% solution of caprolactam in dichloromethane to the reaction vessel. For the polymerization of MAA, the ultrasonic horn was run at 10% while pure MAA was injected using the hand pump. After the injection is complete, the sonication is also stopped. For both polymerizations, the system is purged with 200 mL of fresh CO<sub>2</sub> to

remove any unreacted monomer or residual solvent and then slowly depressurized over several hours.

SEM analysis was performed using a Zeiss DSM 940 after sputter coating the samples with gold. Solid state FTIR spectra were collected on a Nicolet Avatar 360 FTIR. The spectra were collected with 64 averaged scans at a resolution of  $2\text{ cm}^{-1}$ . The solid samples were ground with KBr and compressed to form KBr pellets. DSC results were obtained on a TA Instruments DSC Q100.

## Results

A 1 wt % solution of  $\epsilon$ -caprolactam dissolved in dichloromethane was prepared. SEM images of the product formed from the injection of 9 mL of this solution into  $\text{CO}_2$  at 3000 psi and 313 K are shown in Figure 5-3. The first two images are at a magnification of 200. In the left-most image, the product appears as particulates, while in the middle image, the product is long fibers. The image on the right is a higher magnification,  $\times 2000$ , showing the fibers in more detail. A small amount of titanium dioxide,  $\text{TiO}_2$ , particles was added to the caprolactam solution. SEM images of the product formed from injecting 10 mL of this  $\text{TiO}_2$  modified solution into  $\text{CO}_2$  at 3000 psi and 313 K are shown in Figure 5-4. . The images from left to right are magnified 500, 3k, and 30k times, respectively. The addition of  $\text{TiO}_2$  particles to the caprolactam resulted in the formation of only particles, no evidence of fiber formation was observed. To test the purity of the product formed from the injection of caprolactam in the SAS process, Fourier transform infrared spectroscopy (FTIR) and differential scanning calorimetry (DSC) were performed on the product and compared to the reactant, caprolactam, and the desired product, nylon 6. Figure 5-5 shows FTIR spectra for the

reaction product, as well as pure caprolactam and nylon 6. Comparing the three spectra, the reaction product appears to have all the major peaks of both caprolactam and nylon 6. This suggests that the product is a mixture of unreacted caprolactam and nylon 6, with the possibility of having caprolactam oligomers as well. DSC results for the reaction product along with pure caprolactam and nylon 6 are given in Figure 5-6. The product has two major features. The peak at 63.83 °C matches well with the caprolactam melting point. The second major feature at 197.61 °C appears to be a combination of the nylon 6 melting point and second peak for the caprolactam. The size of the peak is too large to be only the result of caprolactam. The shift to lower temperature of this peak can be attributed to a lower degree of crystallinity in the reaction product. The molecular weight may be estimated by either viscometry or gel permeation chromatography (GPC). Unfortunately, large enough quantities of product were not attainable to employ either of these techniques. Because of the low yield, the use of these materials as non-particulate catalyst supports was not achievable.

A second method of polymerization and precipitation during the SAS process is the formation of PMAA during the spray process. 3 mL of MAA without initiator or inhibitor was injected into CO<sub>2</sub> at 2500 psi and 313 K at the tip of a sonicating horn operating at 10%. SEM images of the product formed in this process are shown in Figure 5-7 and Figure 5-8. The product was observed to be primarily micro-particles and agglomerated particles. Figure 5-7 shows the reaction product at magnification of 50, 500, and 2000 times from left to right. The particles are seen to primarily be loosely agglomerated particles. The first two images in Figure 5-8 are further magnifications of these agglomerates at 5k and 50k magnification. The image on the right is taken at 60

times magnification and shows a very long fiber, the only fiber observed. The agglomeration of the particles is believed to be partially due to locally high temperatures experienced by the particles due to sonication induced cavitation. These high temperatures could cause particle softening, promoting agglomeration. Because the reactant, MAA, is liquid and the product is solid, and no other chemicals were present, the product is believed to be pure PMAA. Unfortunately, no characterization was able to be performed, because the experiments were not successfully repeated.

### **Transport Model for Nylon 6 Formation**

Figure 5-9 shows an illustration of the caprolactam polymerization process at a given distance from the spray nozzle. The transport process of interest is that of the caprolactam out of the droplets, which are formed upon the spraying of a caprolactam in methylene chloride solution into supercritical CO<sub>2</sub>. This process is represented as  $n_A$ , and is shown by the arrows leaving the methylene chloride (MC) droplets. The rate of mass transfer across the interface depends on the bulk concentration of caprolactam in CO<sub>2</sub>, phase 4, and the concentration of caprolactam in the droplet, phase 2.

There are several important assumptions illustrated in this figure. First, the droplets are far enough apart that the surroundings are essentially the bulk CO<sub>2</sub>. If the droplets were close enough to one another that their boundary layers overlapped, the apparent bulk concentration of the caprolactam would be higher. This would reduce the rate of caprolactam transfer. Also, the droplets are far enough away from the growing polymer particles that their boundary layers do not overlap. If the boundary layers did overlap, the apparent bulk concentration would be lower, which would increase the rate of caprolactam transfer. Another assumption is that the region of interest is far enough

from the nozzle that caprolactam has diffused into the bulk and that the bulk concentration is uniform. If the caprolactam had not yet diffused into the bulk, then the rate of caprolactam transfer would be higher, as the driving force would be more. Another assumption is that the bulk phase does not contain methylene chloride. If the bulk did contain methylene chloride, then the rate of caprolactam transfer would be higher because the resistance to mass transfer would be decreased.

The concentration of caprolactam in the bulk is controlled by the solubility of caprolactam in CO<sub>2</sub> (Laitinen and Jantti, 1996), and by the rate of polymerization. The polymerization kinetics for both solid state polymerization (Xie, 2001) and solution polymerization (Agrawal et al., 2001) are known. The concentration of caprolactam in the droplet is controlled by the rates of mass transfer of CO<sub>2</sub> into phase 2 and methylene chloride into phase 4. This is based upon the assumption that these rates are much faster than the rate of mass transfer of caprolactam across the interface because the caprolactam solubility in phase 4 is much smaller than the miscible CO<sub>2</sub> and methylene chloride. If the mass transfer rate for caprolactam were on the same order of magnitude, then the concentration of caprolactam would decrease in the droplet with time, which would decrease the mass transfer rate. The mass transfer processes of methylene chloride and CO<sub>2</sub> in the SAS process have been modeled (Elvassore et al., 2004; Lora et al., 2000; Mukhopadhyay and Dalvi, 2004a; Werling and Debenedetti, 1999, 2000). Since these transport processes directly affect the concentration of caprolactam in phase 2, and as a result the mass transfer of caprolactam, these papers will be discussed in detail. Another important factor in the concentration of caprolactam in the droplets is the solubility of caprolactam in the CO<sub>2</sub>-methylene chloride. As more CO<sub>2</sub> diffuses into the droplets,

some of the caprolactam can precipitate out. This solid solubility behavior in CO<sub>2</sub>-solvent systems has also been analyzed (Mukhopadhyay and Dalvi, 2004b) and will be discussed.

If the system is assumed to be at steady state, then the overall mass balance for the system can be represented by:

$$V * r_A = A_s * \mathbf{n}_A$$

where  $V$  is the volume that does not include the droplets and  $A_s$  is the surface area of the droplets. This is a useful relation because  $\mathbf{n}_A$  can also be related to the concentrations of the caprolactam:

$$\mathbf{n}_A = {}^2K_{A4} * (\rho_{A4}^* - \rho_{A4})$$

where  ${}^2K_{A4}$  is the overall supercritical phase mass transfer coefficient,  $\rho_{A4}^*$  is an imaginary concentration of A in the supercritical phase in equilibrium with the liquid phase, and  $\rho_{A4}$  is the bulk concentration of A in the supercritical phase. For dilute solutions, the Henry's Law approximation:

$$\rho_{A4}^* = H_{\rho A} * \rho_{A2}$$

is valid. For high concentrations of A in the liquid phase,  $\rho_{A4}^*$  equals the solubility of caprolactam in the supercritical CO<sub>2</sub>. Laitinen and Jäntti (Laitinen and Jantti, 1996) measured the solubility of caprolactam in CO<sub>2</sub> using a variable volume view cell. They then modeled their results with the Peng-Robinson equation of state with fairly good agreement. For typical experimental conditions (314 K, 180 bar), caprolactam solubility is 0.048 mole percent.

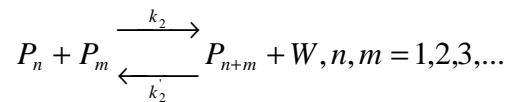
By using the two relations for  $\mathbf{n}_A$  and knowing the rate of reaction of caprolactam, the mass-transfer coefficient, and  $\rho_{A4}^*$ , allows the determination of the bulk concentration

of caprolactam in the CO<sub>2</sub> phase. Alternatively, if the bulk concentration is known, while the mass-transfer coefficient is not, the mass-transfer coefficient for this dynamic process may be estimated. For this reason, understanding of both the reaction kinetics and the liquid-phase concentration of caprolactam, which determines  $P_{A4}^*$ , is essential to modeling the mass-transfer of this system.

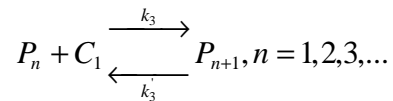
### Polymerization of Caprolactam

As mentioned earlier, the reaction kinetics of caprolactam polymerization are important in determining the bulk concentration of caprolactam. This concentration controls the mass transport of caprolactam out of the methylene chloride droplets. These reaction kinetics have been developed both for polymerization in solution and on a solid surface. Although both of these cases can and likely do occur in this modified SAS process, it will be assumed that only solution polymerization occurs and that the polymer particles are formed by aggregation of polymers. The basic kinetics for either case are the same:

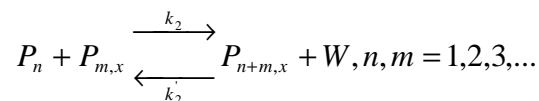
#### 1. Polycondensation



#### 2. Polyaddition



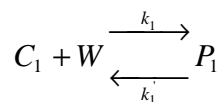
#### 3. Reaction with Monofunctional Acid



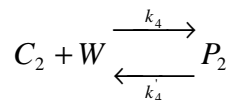
where  $P_n$ ,  $P_{n+1}$ ,  $P_m$  are polymer molecules of chain length  $n$ ,  $n+1$ ,  $m$ , and  $n+m$ .  $P_{m,x}$  and  $P_{n+m,x}$  are polymers with chain length  $m$  and  $n+m$  with an unreactive end group  $x$ .  $W$  is water and  $C_1$  is caprolactam (Agrawal et al., 2001; Xie, 2001). The last step is a termination step caused by the use of a monofunctional acid regulator. Since no regulator is used in the modified SAS process, this step need not be included in the kinetics.

The first step in the kinetic model also needs to be modified. Because the ring-opening occurs in  $CO_2$  and not water, the polycondensation step yields a  $CO_2$  molecule rather than a water molecule. In addition to these basic steps, Agrawal et al. (Agrawal et al., 2001) also included some other steps as well:

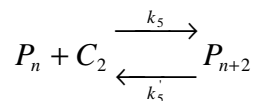
Ring-Opening



Ring Opening of Cyclic Dimer



Polyaddition of Cyclic Dimer



where  $C_2$  represents a cyclic caprolactam dimer. The two ring opening steps need modification for this process. As mentioned previously, the ring opening occurs by reaction of the amine group in caprolactam with  $CO_2$ , so the water molecule in each of these steps needs to be replaced with  $CO_2$ .

The kinetics for the reaction between CO<sub>2</sub> and amines have been modeled by both Danckwerts (Danckwerts, 1979) and Crooks and Donnellan (Crooks and Donnellan, 1989). The mechanism of Danckwerts for the reversible reaction of an amine, such as caprolactam, with CO<sub>2</sub> was first order in the concentration of both the amine and the CO<sub>2</sub>. He then had a second equilibrium reaction between this zwitterionic product and a base. This model included four rate constants that were adjustable dependant upon the amine and the base used. Crooks and Donnellan (Crooks and Donnellan, 1989) argued that this model could be fit to just about anything with four adjustable constants, but they showed that for certain amines and bases chosen, the model did not hold up. They proposed a new mechanism that included only two adjustable constants. More importantly, they showed that the kinetics were the sum of two terms. The first term was second order in the concentration of the amine, while the second term was first order in the concentration of the amine and first order in the concentration of the base. As Crooks and Donnellan pointed out, either kinetic form would be usable to fit the kinetics of a given reaction between CO<sub>2</sub> and an amine. Therefore, either of these kinetic models may be used to replace the two ring-opening steps in the overall kinetics of the polymerization. It is important to note that the zwitterion intermediate is actually the form that yields  $P_1$  and not the dissociated product. This adds to the complexity of the overall kinetics.

This overall kinetic model has significant impact upon the mass transport of caprolactam. As discussed earlier, the rate of reaction of caprolactam multiplied by the volume of reaction yields the mass flux out of the system by reaction. If the bulk concentration is assumed to be constant, then this is also equal to the mass flux of

caprolactam out of the droplets. Since the kinetics provide the rate of reaction of the caprolactam, and therefore the mass flux as well, this provides a method for determining the bulk concentration of caprolactam at steady state if the rate of mass flux from the droplet can be determined as well. Alternatively, if the bulk concentration can be measured, then the mass-transfer coefficient may be estimated.

#### Mass Transport in the Supercritical Antisolvent Process

The SAS process is very complicated from a fluid dynamics standpoint. There has not been a model developed that can account for all of the complexity of the process. To provide insight into the mass transport across the liquid-supercritical fluid interface, other processes such as jet breakup, droplet collisions, and droplets dividing or coalescing have been routinely neglected. Still, there are several publications which have significantly contributed toward understanding the mass transport across this interface.

Werling and Debenedetti (Werling and Debenedetti, 1999, 2000) presented a mathematical model for the mass transfer between an isolated solvent droplet and an antisolvent continuum ranging from subcritical (Werling and Debenedetti, 1999) to supercritical (Werling and Debenedetti, 2000) mixture regimes. Although the temperature and pressure may be high enough that a pure CO<sub>2</sub> phase would be supercritical, a mixture may still be subcritical if the temperature and pressure are not above the critical values for the mixture. Werling and Debenedetti investigated the effect of process conditions on the time scales for mass transfer showing that lower pressures and larger initial radii result in longer droplet lifetimes in two-way diffusion of solvent and antisolvent. For the subcritical mixture regime, the droplets swelled, but for the supercritical mixture regime, the effective droplet radius increased if the organic solvent

density was greater or decreased if the antisolvent density was greater. The studies of Werling and Debenedetti were performed for isothermal processes in which the solute, jet breakup processes, viscous forces, and the effect of Reynolds number on diffusivity were not included, yet they provided valuable insight into the environment to which a solute is exposed within the precipitation process. These studies directly look at the volume of the droplets. Since the amount of caprolactam is assumed constant, the liquid concentration is inversely proportional to the effective droplet volume.

Elvassore et al. (Elvassore et al., 2004) modeled the droplet evolution under mixture supercritical conditions as a function of time including the presence of a dissolved solute. They used the generalized Maxwell-Stefan diffusion equation to describe the diffusion of all three components inside the droplet. They defined the effective droplet radius with the equations of Werling and Debenedetti (Werling and Debenedetti, 2000). They also used the perturbed –hard-sphere-chain equation of state to represent the thermodynamics of the mixture. They used this information to describe the density profile within the droplets. By combining all these equations, they computed both the droplet radius and the radius of precipitation as a function of time for various solute concentrations, temperatures and pressures typical of the SAS process for a variety of solvent-antisolvent systems. One of the systems which they modeled was the methylene chloride-CO<sub>2</sub> system. The usefulness of this model is that the solute concentration is also known as a function of position in the droplet. As with Werling and Debenedetti, this model is for an isothermal process and for stagnant drops, so jet breakup processes, viscous forces, and the effect of Reynolds number on diffusivity were

not included. The model does still provide valuable information about the solute concentration distribution.

Lora et al. (Lora et al., 2000) also examined mass transport for an isothermal, isolated drop, but included motion into the calculations. Any effects of dissolved solute on mass transport and hydrodynamics were neglected, but the solute was included in thermodynamic calculations using the Peng-Robinson equation of state to determine supersaturation. Also, the initial droplet size was assumed. They developed a model for binary counter-diffusion at steady state. A correlation by Hughmark (Hughmark, 1967) was used to estimate the fluid film mass transfer coefficient for solvent vapor. By neglecting internal motions in the droplet, they used the same correlation to approximate the liquid film mass transfer coefficient of CO<sub>2</sub>. They use this model to compute the mole fraction of CO<sub>2</sub> in the droplets and the flow rate of liquid out of the droplet as a function of time at different operating conditions and for different liquid solvents. They also coupled this model with thermodynamic calculations to calculate the percent precipitation of naphthalene and phenanthrene from a toluene solution sprayed into CO<sub>2</sub> as a function of distance. Although the model was not used for caprolactam and methylene chloride, the equations used are still applicable.

Mukhopadhyay and Dalvi (Mukhopadhyay and Dalvi, 2004a) modeled the mass transfer of an isolated droplet falling through a CO<sub>2</sub> phase to simulate the environment in the SAS process. Although the modeling calculations are for an acetone droplet, the equations used to model the droplet are generic enough to cover any liquid droplet falling through CO<sub>2</sub>. Although this model still does not include the presence of solute or jet breakup processes, this model is a significant improvement because it includes heat

transport, flow rates, viscosity, surface tension, and the effect of Reynolds number on mass transfer coefficients and diffusivities. The initial droplet size was calculated based on correlations to the process conditions and solvent properties. The velocity was calculated based upon a force balance. The penetration theory was used to estimate the liquid film mass transfer coefficient of CO<sub>2</sub>, while a correlation by Hughmark (Hughmark, 1967) was used to estimate the fluid film mass transfer coefficient for solvent vapor. This model provides the mole fractions of CO<sub>2</sub> and solvent as a function of time. The droplet size is also found as a function of time. Mukhopadhyay and Dalvi show that the size of the droplet can increase, decrease, or both as a function of time (or distance) depending on what temperature, pressure, and flow rates are chosen as operating conditions. Although the specific dependence of size on operating conditions would be different for methylene chloride than acetone, the general behavior would remain the same. These results provide the basis for estimating caprolactam concentration at a given distance.

Mukhopadhyay and Dalvi (Mukhopadhyay and Dalvi, 2004b) also modeled the solubility of various solids in CO<sub>2</sub>-liquid mixtures. This model takes into account the partial molar volume fraction of the liquid solvent as well as solubility data for the solid in the liquid solvent. They calculate the partial molar volume fraction based upon the mole fraction of CO<sub>2</sub> in the liquid phase in the absence of solute. Since they have already modeled the mole fraction of CO<sub>2</sub> as a function of time (Owens et al., 2002) for the SAS process, this model may be used to calculate the solubility of a dissolved solute as a function of time during the SAS process. This information is important to verify that the concentration of caprolactam calculated based solely on the volume of the droplet does

not exceed the solubility of the solid in the mixture. If the calculated concentration is higher, then the solid will precipitate out, and the solubility of the solid in the mixture should instead be used as the concentration of caprolactam in the droplets.

### Overall Transport Model

The mass transfer rate of caprolactam into the CO<sub>2</sub> phase has been related to the polymerization kinetics and a concentration dependent driving force. The polymerization kinetics for the polymerization of caprolactam in CO<sub>2</sub> have been discussed. The rate of reaction equals the rate of mass transfer under steady state assumptions. Modeling of the concentration of caprolactam in the droplets, which is related to an imaginary concentration of A in the supercritical phase in equilibrium with the liquid phase, has also been discussed. If the mass transfer coefficient is known, then the bulk caprolactam concentration may be estimated. Although this mass transfer coefficient has not been measured, the mass transfer coefficient for liquids transferring to the supercritical fluid phase have been estimated by Mukhopadhyay and Dalvi (Mukhopadhyay and Dalvi, 2004a) by using a correlation by Hughmark (Hughmark, 1967). The methylene chloride mass transfer coefficient may be related to the mass transfer coefficient for caprolactam by:

$${}^2K_{A4} = {}^2K_{B4} \left( \frac{D_{A4}^{(l)}}{D_{B4}^{(l)}} \right)^{0.5}$$

where B represents methylene chloride,  $D^{(l)}$  represents laminar diffusivity, and 0.5 was chosen as exponent to be consistent with the use of penetration theory in the model. Alternatively, if the bulk concentration of caprolactam may be measured by some spectroscopic technique, then the mass transfer coefficient may be estimated. These

models provide a description of the mass transfer of caprolactam in the SAS process at a distance where droplets are well separated.

## **Conclusions**

Two new methods for polymerization have been developed. The reaction of caprolactam with CO<sub>2</sub> and polymerization followed by precipitation during the SAS process was explored. The resulting product was a mixture of particles and long fibers. The addition of TiO<sub>2</sub> particles caused the product to form spherical particles instead of a mixture of fibers and particles. The addition of TiO<sub>2</sub> particles caused the product to form spheres instead of spheres and particles. Product analysis suggested that the product was a mixture of the caprolactam and nylon 6. A second polymerization reaction involving the sonication induced free radical polymerization of MAA to PMAA during the SAS-EM process was also explored. The product is believed to be pure PMAA. These results produced limited quantities of product. Future experiments must be performed to advance the development of these novel processes. A mass transport model for the polymerization of caprolactam in the SAS process was also developed for a position in the spray well away from the spray entrance where the droplets are well separated. These processes are only possible because of the interactions of the monomers with the CO<sub>2</sub> to form the polymers. In the case of caprolactam, it is a reaction with CO<sub>2</sub>. The CO<sub>2</sub> dissolves MAA, due to interactions with the carboxylic acid group, allowing the polymerization to occur. In each case, the product is insoluble in CO<sub>2</sub>, making product recovery simple.

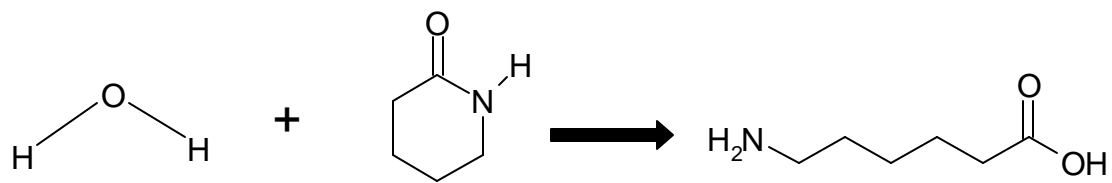


**Figure 5-1** Ring-opening reaction between water and caprolactam.

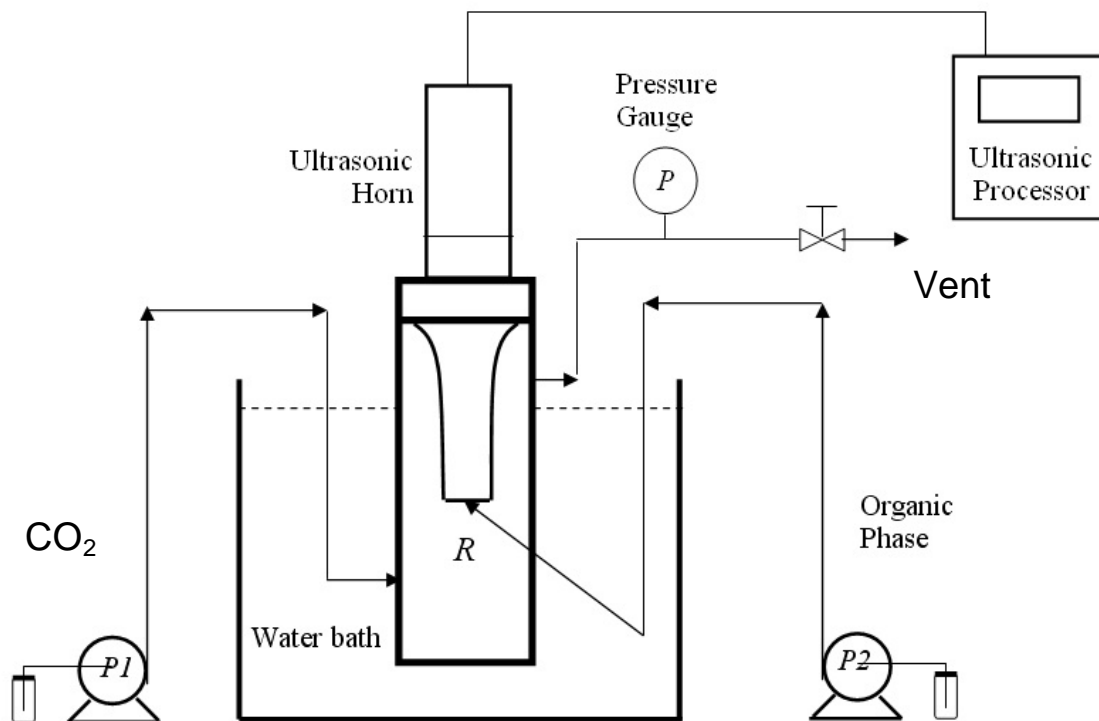


**Figure 5-2** Experimental apparatus used in the polymerization reactions during the supercritical antisolvent precipitation process. P1 is the pump used for introducing carbon dioxide, CO<sub>2</sub>, to the reaction vessel, R. P2 is the pump used to inject a liquid solution containing the monomer to be polymerized.

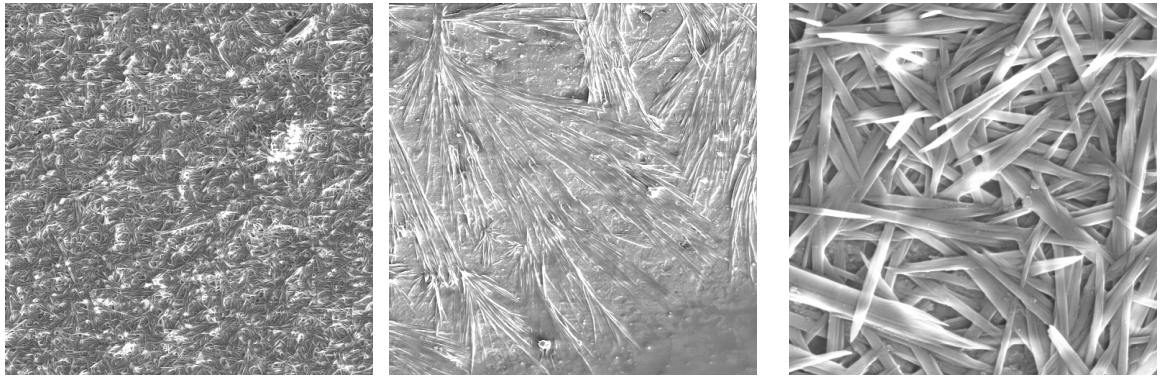


**Figure 5-3** Scanning electron microscopy images of Nylon 6 polymerized during the supercritical antisolvent precipitation process. The first two images are magnified 200 times and show both particulate and fiber-like Nylon 6. The image on the right is magnified 2000 times showing fibers in more detail.

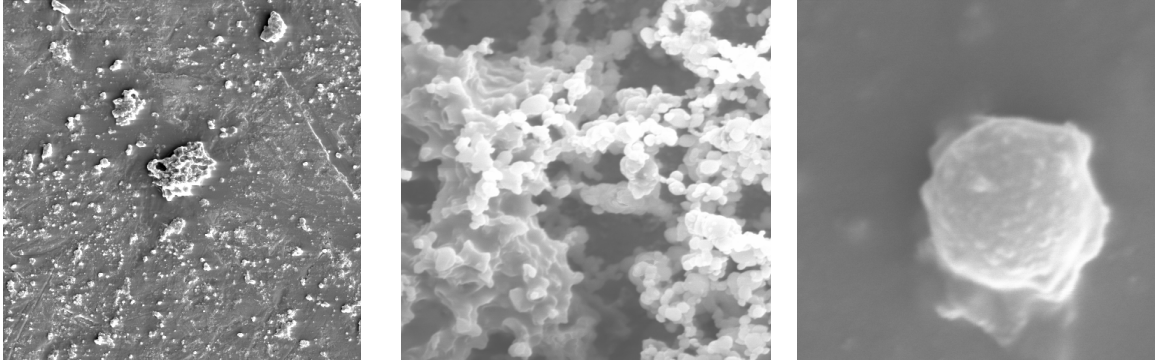


**Figure 5-4** Scanning electron microscopy images of Nylon 6 polymerized with  $\text{TiO}_2$  during the supercritical antisolvent precipitation process. The image on the left is magnified 500 times, the image in the center is magnified 3k, and the image on the right is magnified 30k.

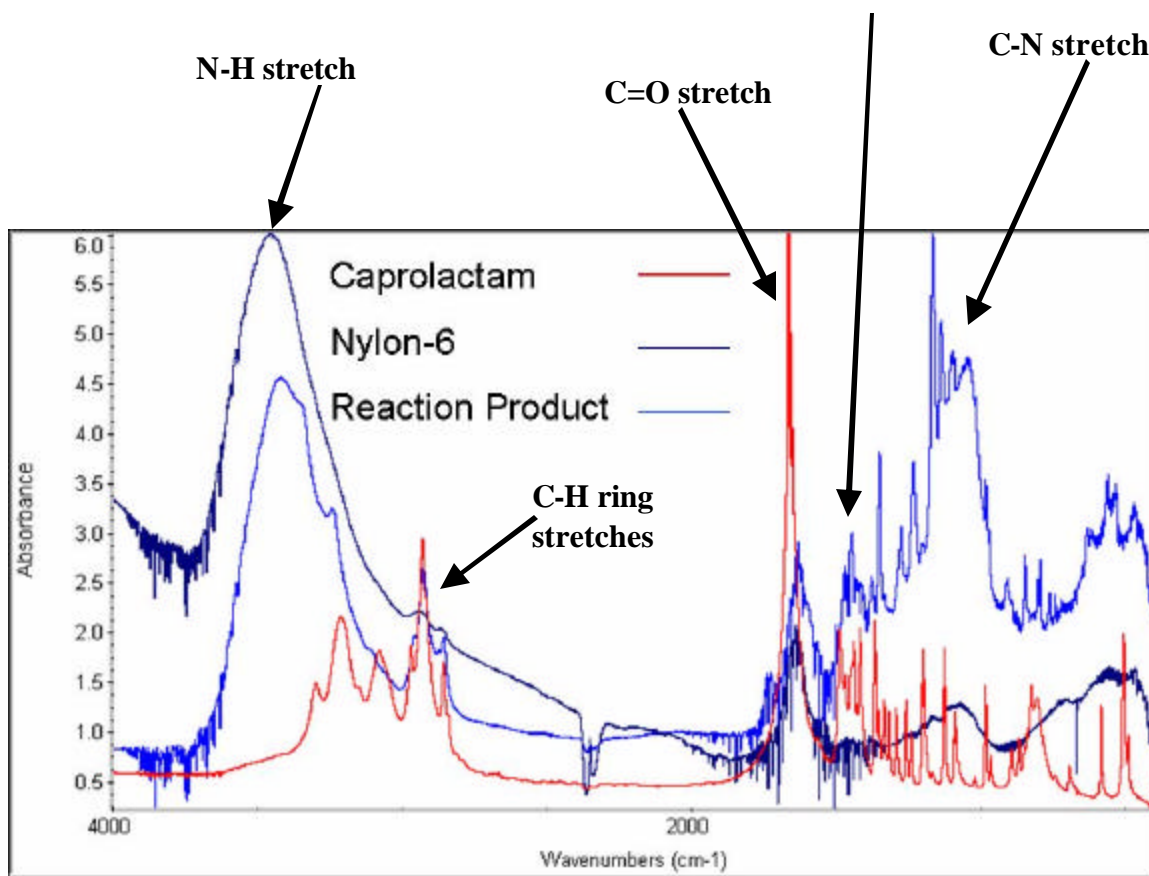


**Figure 5-5** Fourier transform infrared transform spectra of pure caprolactam (red), pure Nylon 6 (dark blue), and the caprolactam reaction product (light blue).

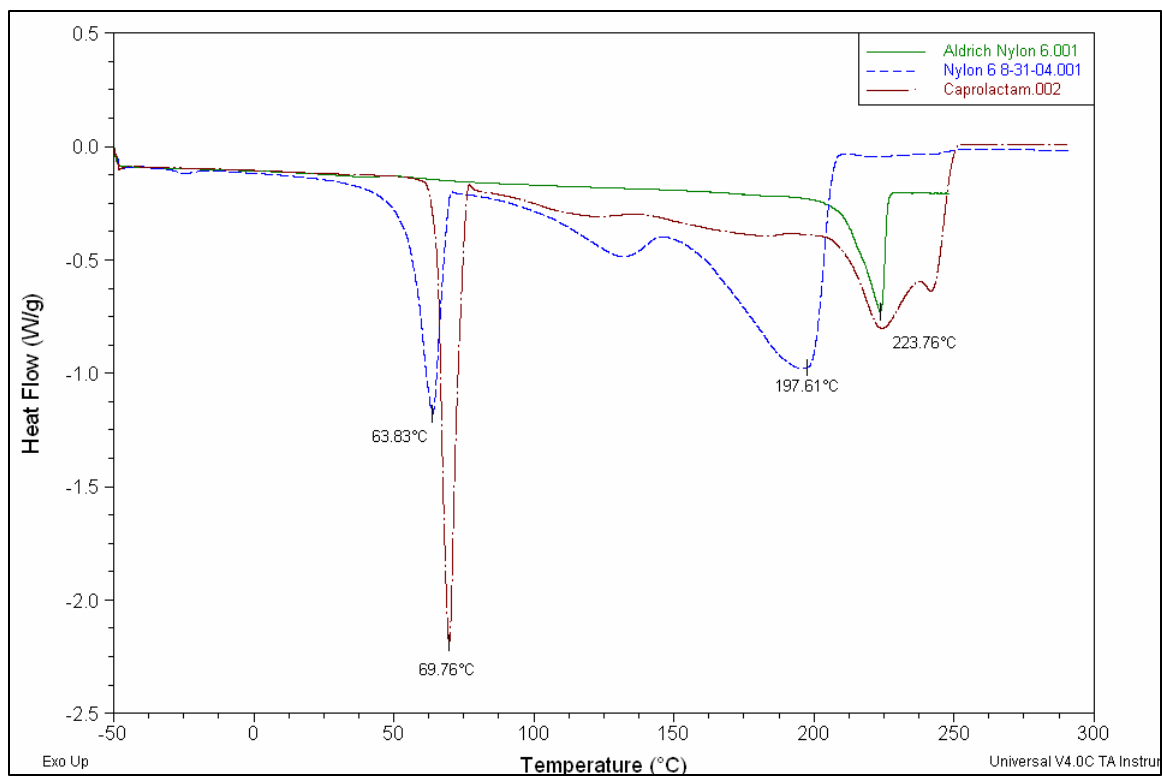


**Figure 5-6** Differential scanning calorimetry scans of pure Nylon 6 (green), the caprolactam reaction product (blue), and pure caprolactam (brown).

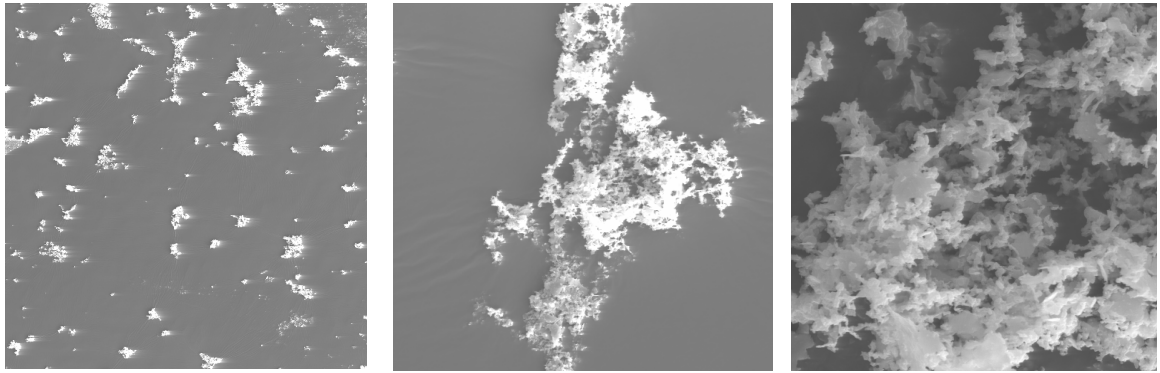


**Figure 5-7** Scanning electron microscopy images of polymethacrylic acid polymerized during the supercritical antisolvent precipitation process with enhanced mass transfer. From left to right, the images are magnified 50, 500, and 2000 times.

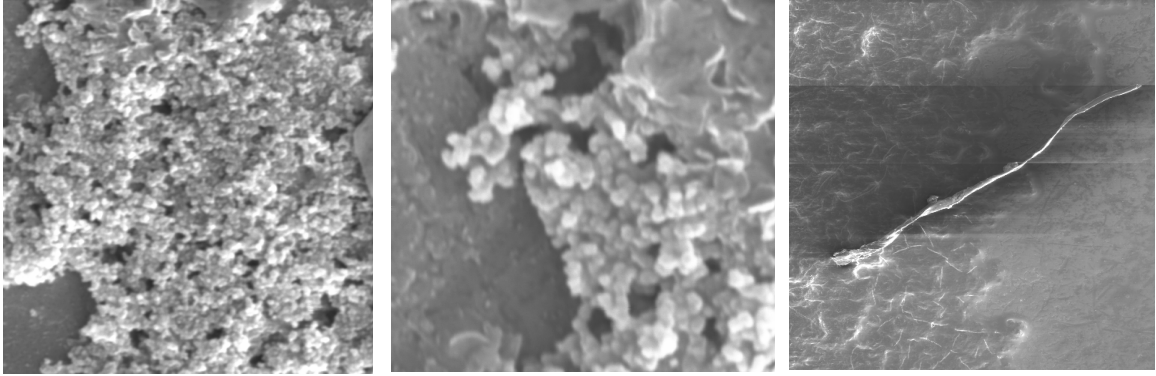


**Figure 5-8** Scanning electron microscopy images of polymethacrylic acid polymerized during the supercritical antisolvent precipitation process with enhanced mass transfer. From left to right, the images are magnified 5k, 50k, and 60 times.

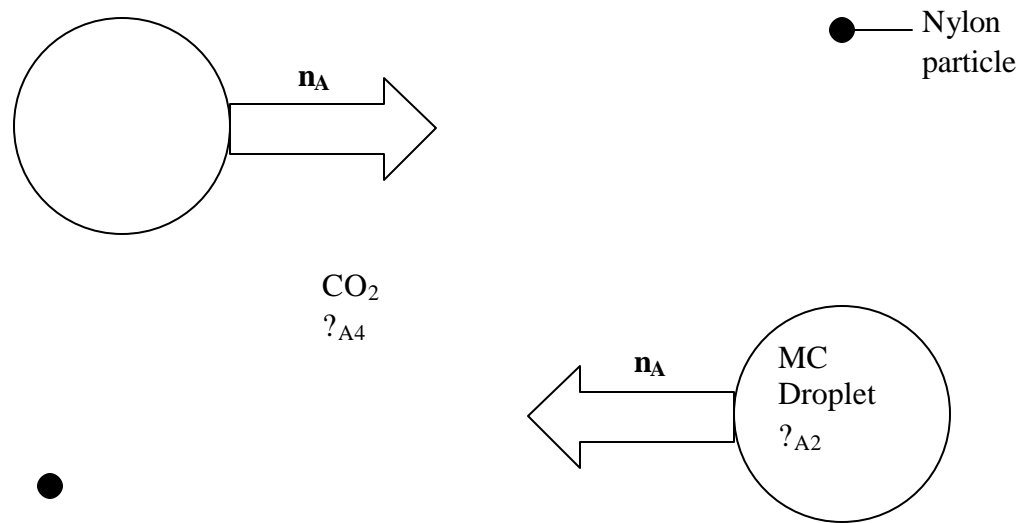


**Figure 5-9.** Illustration of caprolactam transport in the SAS process.  $n_A$  represents the flux of caprolactam, A.  $c_{A2}$  is the concentration of caprolactam in the methylene chloride, MC, phase.  $c_{A4}$  is the concentration of caprolactam in the  $\text{CO}_2$  bulk.

## CHAPTER 6

### STABLE DISPERSIONS OF SILVER NANOPARTICLES IN CARBON DIOXIDE WITH FLUORINE-FREE LIGANDS

#### **Abstract**

Iso-stearic acid, a short, stubby compound with branched, methylated tails has been shown to have high solubility in carbon dioxide. The solvation of the tails by carbon dioxide makes isostearic acid a good choice for use as a ligand to sterically stabilize metallic nanoparticles. Iso-stearic acid coated silver nanoparticles have been stably dispersed in carbon dioxide with hexane co-solvent. Neat carbon dioxide has successfully dispersed isostearic acid coated silver nanoparticles that had been deposited on either quartz or polystyrene surfaces. These results are the first reports of sterically stabilized nanoparticles in carbon dioxide without the use of any fluorinated compounds. The use of isostearic acid as a CO<sub>2</sub>-philic ligand was extended to the one-step synthesis and stabilization of silver nanoparticles in dense CO<sub>2</sub> without the use of organic solvents or fluorinated compounds. This is the first report of metallic nanoparticle synthesis and stabilization in dense CO<sub>2</sub> without any fluorinated compounds.

## Introduction

Carbon dioxide (CO<sub>2</sub>) is an inexpensive, nontoxic, and non-flammable solvent that has garnered recent attention in the area of nanoparticle processing (Holmes et al. 1999; Ji et al. 1999; Ohde et al. 2000; McLeod et al. 2003; Shah et al. 2004). Compressed and supercritical CO<sub>2</sub> has many characteristics which make it desirable for use as a solvent in these systems. Some of these characteristics are that the density, diffusivities, solubility parameter, heat transfer coefficients, and mass transfer coefficients, can be varied from those of the liquid phase to that of the vapor phase continuously (McHugh and Krukoniš 1994). The properties of these tunable supercritical fluid solvents can allow for the reversible dispersion and deposition of nanoparticles onto surfaces (Shah et al. 2002). Shah et al. increased ethane solvent density to disperse increasingly larger silver and gold nanoparticles in the ethane media. By reducing the ethane density, the largest particles were precipitated first, followed by precipitation of smaller particles as the density was further reduced. Another feature of supercritical carbon dioxide in nanoparticle synthesis is that it has a vanishing surface tension (Shah et al. 2004), making it a desirable process solvent for nano-scale materials and devices. For example, McLeod et al. (McLeod et al. 2005) and Shah et al. (Shah et al. 2003) used this vanishing surface tension in CO<sub>2</sub> systems to make more uniform thin films of nanoparticles than could be made by solvent evaporation techniques. These techniques take advantage of the ability to control dispersions of nanoparticles through the adjustable properties of CO<sub>2</sub> solvent systems.

In order to disperse particles in a given solvent, it is common to use ligands extending from the surface of the nanoparticles that can interact with the solvent

molecules. Favorable interactions between the solvent molecules and the ligand tails provide enough repulsive force between particles to overcome the attractive Van der Waals forces that occur between particles in solution. Unfortunately, CO<sub>2</sub> is a poor solvent for most commonly available ligands and surfactants. As a result, fluorinated surfactants have been required to stabilize nanoparticles in CO<sub>2</sub> or to form microemulsions for the synthesis of nanoparticles within CO<sub>2</sub>. Early studies showed the ability of these fluorinated compounds to support water in CO<sub>2</sub> microemulsions (Johnston et al. 1996; Clarke et al. 1997) based on better surfactant tail – solvent interactions. These water in CO<sub>2</sub> microemulsion systems have since been used to form a variety of nanoparticles in CO<sub>2</sub> (Holmes et al. 1999; Ji et al. 1999; Ohde et al. 2000; Dong et al. 2002; McLeod et al. 2003; Zhang et al. 2003; Liu et al. 2005). The need for surfactants, and a separate water phase, during synthesis of nanoparticles in CO<sub>2</sub> was eliminated by Shah et al. (Shah et al. 2001; Shah et al. 2002) and McLeod et al. (McLeod et al. 2004) where the synthesis and subsequent precipitation of nanoparticles was achieved in a single CO<sub>2</sub> phase. The approach in these studies was to reduce fluorinated CO<sub>2</sub>-soluble metallic precursors in a single CO<sub>2</sub> phase and to prevent agglomeration by capping the particles with CO<sub>2</sub>-soluble fluorinated ligands that provide for steric stabilization of the particles. Recently, Fan et al. (Fan et al. 2005) directly reduced a non-fluorinated precursor, Ag-AOT-TMH, in CO<sub>2</sub>, and stably dispersed the formed particles by using fluorinated thiol ligands. Unfortunately, these processes continue to require the use of fluorinated ligands to disperse the nanoparticles. These CO<sub>2</sub> soluble fluorinated compounds suffer from the disadvantages of being both expensive and environmentally unfriendly (Sarbu et al. 2000; Dimitrov et al. 2004). Several research groups (Hoefling et

al. 1991; Hoefling et al. 1993; Rindfleisch et al. 1996; Lora et al. 1999; Sarbu et al. 2000a; Sarbu et al. 2000b; Eastoe et al. 2001; Johnston et al. 2001; Potluri et al. 2002; Eastoe et al. 2003; Raveendran and Wallen 2003; Shen et al. 2003) have sought to find non-fluorinated compounds that would be soluble in CO<sub>2</sub> in the hopes of creating non-fluorinated polymers as well as surfactants where the latter could be used to form microemulsions in CO<sub>2</sub>. Research has shown that branched, methylated, and stubby surfactants can be used to form micelles in supercritical CO<sub>2</sub>, because of higher tail solvation and smaller tail-tail interactions (Eastoe et al. 2001; da Rocha et al. 2003; Stone et al. 2003; Stone et al. 2004). Although some success has been reported in forming fluorine-free microemulsions using hydrocarbon surfactants (Liu et al. 2001; Ryoo et al. 2003) and in making macroemulsions using silica nanoparticles (Dickson et al. 2004), ionic hydrocarbon surfactants (Dickson et al. 2005; Fan et al. 2005), or trisiloxane surfactants (da Rocha et al. 2003) in CO<sub>2</sub>, no reports to date have demonstrated the synthesis or dispersion of nanoparticles within these non-fluorinated surfactant systems in CO<sub>2</sub>. While metallic nanoparticles have been stably dispersed in pure liquid and supercritical CO<sub>2</sub> (Shah et al. 2000; Saunders et al. 2004), fluorinated ligands were required. To make full use of the advantages of supercritical CO<sub>2</sub>, a stable dispersion of fluorine-free nanoparticles in a single CO<sub>2</sub> phase would be ideal. The focus of this chapter is to illustrate the ability to stably disperse ligand coated metal nanoparticles in neat CO<sub>2</sub> without the need for fluorinated constituents. This has been accomplished by either redispersing particles synthesized in an organic solvent, or by doing a one-step synthesis and stabilization of silver nanoparticles in CO<sub>2</sub>. To the authors' knowledge, the

results here are the first report of stably dispersed nanoparticles in a single CO<sub>2</sub> phase without the presence of fluorinated compounds.

## **Experimental**

### Materials

The surfactant sodium bis(2-ethylhexyl) sulfosuccinate (AOT) and methanol (99.9%) were purchased from Fisher Scientific and silver nitrate (99.8%) was purchased from Acros. Iso-stearic acid was received from Nissan (100%). AOT-TMH was used as received from the University of Bristol. Isooctane (99.8%), hexane (99+%), and anhydrous hydrazine (98%) were obtained from Aldrich. Lauric Acid (99%) sodium borohydride (NaBH<sub>4</sub>) (ReagentPlus, 99%), and anhydrous ether (99+%) were acquired from Sigma. Ethanol (200 proof) was obtained from Florida Distillers. Deionized water was used in the particle synthesis. Carbon dioxide (SFC/SFE grade) was obtained from Airgas. All materials were used as received.

### Ag-AOT-TMH Synthesis

The CO<sub>2</sub>-soluble silver salt, silver bis(3,5,5-trimethyl-1-hexyl) sulfosuccinate (Ag-AOT-TMH) was synthesized by an ion-exchange of the sodium bis(3,5,5-trimethyl-1-hexyl) sulfosuccinate (AOT-TMH) compound. The AOT-TMH synthesis has been described elsewhere (Nave et al. 2000). The technique followed for the ion exchange was adapted from that given by Fan et al. (Fan et al. 2005). The procedure is briefly described here. 5.025 g AgNO<sub>3</sub> (29.58 mmol) was dissolved in 10 mL of deionized water. 0.8297 g AOT-TMH (1.8 mmol) was dissolved in 5 mL of ethanol. The two solutions were mixed for 6 hours. 6 mL of ether was added to form two phases. The two phases were separated and the upper phase containing Ag-AOT-TMH was dried in a

vacuum oven at room temperature. The remaining solid was re-dissolved in isooctane and centrifuged to remove any solid contaminants. The solid dissolved in isooctane was again dried in a vacuum oven at room temperature, resulting in a yellowish-brown solid, Ag-AOT-TMH.

### Phase Behavior Measurements

To measure the phase behavior of the iso-stearic acid/CO<sub>2</sub> mixture or the Ag-AOT-TMH/CO<sub>2</sub> mixture, a known amount of iso-stearic acid or Ag-AOT-TMH (e.g.,  $1.1560 \pm 0.0001$  g) was loaded into the sample volume of a high pressure, windowed, stirred, variable-volume view cell (DB Robinson & Assoc., 3.18 cm ID, ~120 mL working volume). In this cell, the sample volume is separated from the overburden fluid by a steel cylinder (floating piston) that retains an O-ring around its perimeter. The O-ring permits the cylinder to move while retaining a seal between the sample volume and the overburden fluid. After purging with carbon dioxide at 2 bar, the sample volume was minimized by displacing the floating piston to the highest possible position within the cell that did not result in the compaction of the iso-stearic acid. High pressure liquid carbon dioxide (295 K, 138 bar) was then introduced to the sample volume as the silicone oil overburden fluid was withdrawn at the equivalent flow rate using a dual-proportioning positive displacement pump (DB Robinson). This technique facilitated the isothermal, isobaric addition of a known volume of CO<sub>2</sub> (e.g.,  $11.93 \pm 0.01$  mL) into the sample volume. The mass of CO<sub>2</sub> introduced was determined from the displaced volume, temperature, and pressure using an accurate equation of state for carbon dioxide (Span and Wagner 1996). Based on the uncertainties associated with the measurement of temperature, pressure, volume, and the precision of the equation of state, compositions

are estimated to be accurate to within 1% of the specified value (e.g.,  $10 \pm 0.1$  wt%). The iso-stearic acid–CO<sub>2</sub> mixture or the Ag-AOT-TMH mixture was mixed thoroughly using a magnetic stirrer (DB Robinson, max. 2500 rpm) at 138 bar to reach a single transparent phase. Phase behaviors were determined by standard non-sampling techniques; the slow, isothermal expansion of the sample volume until a new phase appeared. Additional CO<sub>2</sub> was added to the system for the phase behavior measurement at lower concentrations. Pressures for each concentration were reproduced two or three times to within approximately  $\pm 5$  bar. Temperatures were measured with a type K thermocouple to an accuracy of  $\pm 0.2$  K.

### Nanoparticle Synthesis

Silver nanoparticles were initially formed via reduction reaction within the cores of AOT reverse micelles. Specifically, an appropriate amount of AOT was added to isooctane and stirred until dissolved. In a separate container, silver nitrate was added to deionized water. The two solutions were then mixed to form a microemulsion with overall concentrations of 0.1 M AOT and 0.001 M silver nitrate. The mixture had a water to surfactant molar ratio, W (Pileni et al. 1985), of 10. An excess of hydrazine (0.003 M) reducing agent was then added to the microemulsion and stirred for 1 day. An excess (0.2 M) of lauric acid or iso-stearic acid was then added and stirred for 2 days to replace the AOT as the capping agent on the surface of the particles. A 2:1 mixture of methanol and ethanol was then added as an antisolvent and the mixture was centrifuged (Fisher Centrifuge Model 228) to precipitate out the silver nanoparticles. The particles were then washed with ethanol and centrifuged again to remove any unbound ligands, lauric acid or iso-stearic acid, and residual AOT. The recovered particles were dispersed

in hexane using sonication (Fisher) and centrifuged to remove agglomerated particles. The remaining dispersion was used in all experiments.

### Particle Imaging

A Zeiss EM 10 TEM was used for TEM analysis. TEM grids were either prepared by allowing a droplet of the dispersed particles in hexane to evaporate on the grid or by the direct spraying of synthesized particles from a high pressure cell onto the TEM grid. Particle sizing of the silver nanoparticles from the TEM images was performed using ImageJ software, where each particle was bounded by a rectangle and the diameter was approximated by the average of the length and width.

### Infrared Spectroscopy

To determine whether iso-stearic acid ligands were attached to the silver particles, attenuated total reflectance Fourier transform infrared (ATR-FTIR) spectroscopy was performed using a Perkin-Elmer Spectrum 2000 FTIR spectrometer. The resolution used was  $2\text{ cm}^{-1}$  and the number of scans was 64. Samples were prepared by evaporating the hexane dispersion on the surface of the ATR cell.

### Particle Dispersions

In an initial set of experiments, isostearic acid coated silver particles were dispersed in  $\text{CO}_2$  with the aid of a non-fluorinated co-solvent (dispersions in neat  $\text{CO}_2$  without co-solvent are described below). To disperse silver particles in  $\text{CO}_2$  with a co-solvent, a nanoparticle dispersion in hexane was injected into pressurized  $\text{CO}_2$ . Initially, the vessel was pressurized with  $\text{CO}_2$  to 276 bar at 295 K using an ISCO syringe pump. Subsequently, 11 mL of a hexane dispersion of isostearic acid coated silver particles was injected, using an HiP high pressure hand operated syringe pump, into a 96 mL fixed

volume stainless steel vessel equipped with two quartz windows for UV-vis analysis. The pressure was controlled with the syringe pump. The introduction of the dispersion of nanoparticles into the CO<sub>2</sub> allowed the re-dispersion of the particles into the bulk CO<sub>2</sub>/hexane mixture (11% hexane by volume). The ultraviolet-visible (UV-vis) spectra of re-dispersed particles were collected on a Varian 300E spectrophotometer.

Figure 6-1 shows a diagram of the apparatus used to concentrate the particles. The main difference, other than the volume of the vessel, between this setup and that used in the initial injection experiments is the presence of a moveable piston. This allows for varying the volume of the vessel as well as a convenient method to deliver the CO<sub>2</sub> dispersion to the collection vessel. The major components of the system are an ISCO 260D syringe pump, a 6-port injection valve (Valco), a high-pressure needle valve (HiP), a high-pressure view cell equipped for UV-vis measurements, a hand operated syringe pump (HiP) with a movable piston, a second high pressure needle valve (HiP), and a collection vessel with 1 mL of hexane chilled by an ice bath to reduce evaporation. The connections are made with 1/16" stainless steel tubing (HiP). The 60 mL stainless steel view cell equipped with two opposing quartz windows for UV-vis analysis and a third perpendicular window that allows observation of the entire vessel contents was pressurized with CO<sub>2</sub> to 276 bar at 295 K using the ISCO syringe pump. The back end of this 60 mL view cell was connected to an HiP hand operated syringe pump modified to hold a movable piston and attach directly to the high pressure view cell. The pressure was maintained at 276 bar by increasing the volume of the cell assembly by adjusting the piston in the hand operated syringe pump while the hexane dispersion of isostearic acid coated silver particles was injected. One mL aliquots of the dispersion were added using

the six port injection valve. Each aliquot was delivered to the high pressure view cell by flowing CO<sub>2</sub> from the ISCO syringe pump as the piston in the hand operated pump was moved to increase the volume. This process was repeated 6 times to deliver a total of 6 mL of the hexane dispersion to the cell, resulting in a 10% hexane by volume mixture. After the system was equilibrated for two days, the contents were then bubbled over several hours into 1 mL of chilled hexane in the collection vessel. The contents were delivered to the collection vessel by reducing the volume to half the original volume using the hand pump to maintain the pressure inside the high pressure vessel. This insured that only those particles that had been successfully dispersed in the CO<sub>2</sub>/hexane mixture were delivered to the collection vessel by transferring only the liquid phase out of the variable volume cell. Any particles that had not been dispersed were given time to precipitate and adhere to the surface, so they were left in the variable volume high pressure cell assembly. The resulting hexane dispersion concentrated the recovered silver particles to 30 times that which had been dispersed in the hexane-CO<sub>2</sub> mixture.

For dispersion in neat CO<sub>2</sub>, a dispersion of silver nanoparticles in hexane was allowed to evaporate on a surface. Four surfaces were examined: quartz, glass, stainless steel, and polystyrene. The surface being examined was then placed inside the same stainless steel view cell that was used during the previously described co-solvent experiments. Care was taken to ensure that the surfaces used were below the level of the windows to avoid having the UV-vis beam source pass through the surface. The vessel was then pressurized to 276 bar at 295 K using an ISCO 260D high-pressure syringe pump. The pressure was monitored using a 68920-44 Psi-Tronix pressure gauge. The

particles were concentrated in isooctane in the same manner as described above without injecting hexane dispersions.

### One-Step Synthesis and Stabilization in CO<sub>2</sub>

Ag-AOT-TMH was directly reduced in dense CO<sub>2</sub> to produce silver nanoparticles and capped with isostearic acid ligands. These particles were dispersed in CO<sub>2</sub> in a one-step process. 0.0516 g Ag-AOT-TMH (0.06 mol%), 0.175 g isostearic acid (0.17 mol%), and 0, 2, or 10 mL cyclohexane were loaded into a 96 mL stainless steel vessel equipped with opposing quartz windows to allow passage of a UV-vis beam along with a Teflon coated magnetic stir bar. The contents of the vessel were then pressurized with CO<sub>2</sub> to 207 bar at 295 K. The contents were stirred for 1 hour to fully dissolve all solutes and achieve a single-phase mixture. 540  $\mu$ L of a 0.8 M NaBH<sub>4</sub> in ethanol solution was added using a 6 port injection valve. Additional CO<sub>2</sub> was used to force in the reducing agent, increasing the total pressure to 276 bar. The silver nanoparticles formed from the reduction were monitored by UV-vis spectroscopy.

### **Results and Discussion**

Isostearic acid, shown in Figure 6-2, was chosen as a ligand for dispersion of silver nanoparticles in CO<sub>2</sub> solvent. Figure 6-3 presents a pressure-composition diagram for the iso-stearic acid-CO<sub>2</sub> mixture obtained through phase behavior measurements as described above. These measurements demonstrate that iso-stearic acid is highly CO<sub>2</sub>-soluble. It is completely miscible with CO<sub>2</sub> at pressures above 138 bar at 295 K, as shown in Figure 6-3. No data was collected for the small VL1 two phase region at the CO<sub>2</sub>-rich end of the diagram. The high CO<sub>2</sub> solubility may be attributable to the highly methylated branched tails, in which the surface energy of the pendant methyl groups is

much lower than that of the CH<sub>2</sub> groups of linear tails (O'Neill et al. 1998). These interactions between the ligand tails and CO<sub>2</sub> are also what make iso-stearic acid a useful ligand for particle dispersions in CO<sub>2</sub>.

It has been shown that stubby surfactants can be used to form micelles in supercritical CO<sub>2</sub>, because of higher tail solvation and smaller tail-tail interactions (Eastoe et al. 2001; da Rocha et al. 2003; Stone et al. 2003; Stone et al. 2004). Combining this information with the high solubility of iso-stearic acid in CO<sub>2</sub>, the stubby iso-stearic acid seemed a good choice as a ligand for dispersion in CO<sub>2</sub>. Figure 6-4 shows a transmission electron microscope (TEM) image of iso-stearic acid coated silver nanoparticles prepared in the reverse micelle method previously described. The nanoparticles appear to be spherical and range from 3 to 10 nm in diameter with a mean diameter of 4.7 nm. Figure 6-5 shows a particle size distribution of the iso-stearic acid-coated particles where 299 particles were sized.

Figure 6-6 shows the ATR-FTIR spectrum of the unprocessed iso-stearic acid coated silver nanoparticles. The observed peaks correspond to the peaks of pure iso-stearic acid where the broad peak at 3100 cm<sup>-1</sup> corresponds to the O-H stretch, the peak at 2870 cm<sup>-1</sup> corresponds to the O-H stretches, the peak at 1700 cm<sup>-1</sup> corresponds to the C=O stretch, and the peak at 1467 cm<sup>-1</sup> corresponds to the C-O stretch. Because the iso-stearic acid ligands are bound to the silver nanoparticles, the interactions of the ligand tails with CO<sub>2</sub> allow the silver particles to be dispersed in a CO<sub>2</sub> phase.

Depending upon the size, shape, and local environment, silver nanoparticles exhibit a plasmon absorbance band centered between 384 and 430 nm (Petit et al. 1993; Zhang et al. 2000). UV-vis absorbance measurements were made on the silver particles

particles dispersed in CO<sub>2</sub> with hexane co-solvent. The measured UV-vis absorbance spectrum for the iso-stearic acid coated silver particles in CO<sub>2</sub> with hexane co-solvent is shown in Figure 6-7 where there is a distinct peak centered at 424 nm indicating the presence of dispersed silver particles in the CO<sub>2</sub>/hexane bulk phase. Petit et al. (Petit et al. 1993) attribute broad peaks in this region to small silver particles having strong interactions with the surrounding environment. While this absorption band centered at 424 nm indicates the successful dispersion of silver nanoparticles, the relatively small absorbance value also indicates that the concentration of dispersed particles remains low. Because of this small absorbance value, the co-solvent experiments were repeated to allow the CO<sub>2</sub> dispersed particles to be concentrated.

Figure 6-8 shows a UV-vis absorbance spectrum of the concentrated particles collected in the hexane collection vessel confirming that the peak observed in the high pressure vessel was indicative of dispersed silver particles. Figure 6-9 shows a TEM image of the particles precipitated from the concentrated hexane dispersion, confirming the successful dispersion of silver particles in the CO<sub>2</sub>-hexane mixture. These results are the first demonstration of the dispersion of metallic nanoparticles in CO<sub>2</sub> with a co-solvent without the use of fluorinated ligands. Alternatively, the UV-vis spectra of lauric acid and AOT coated silver nanoparticles in an identical hexane-CO<sub>2</sub> mixture show no evidence of dispersed silver nanoparticles. These results show that the interactions of the ligand tail with CO<sub>2</sub> play a critical role in the dispersion of nanoparticles. While the AOT and lauric acid tails do not interact strongly enough, the interaction of CO<sub>2</sub> with the highly branched tails of iso-stearic acid is strong enough to disperse silver nanoparticles.

To suspend the silver particles in neat CO<sub>2</sub>, the co-solvent needed to be removed. Figure 6-10 shows the UV-vis spectrum of iso-stearic acid coated silver nanoparticles dispersed in CO<sub>2</sub> from a quartz surface. The peak observed at 424 nm indicates the presence of dispersed silver particles as has been previously shown (Ershov and Henglein 1998; McLeod et al. 2003). The spectrum was taken 17 hours after pressurization with CO<sub>2</sub>, indicating that the dispersion is stable for long periods of time. The contents were then bubbled into isooctane at atmospheric pressure by reducing the volume using the hand operated pump to maintain the pressure inside the high pressure view cell, thereby retaining the stable dispersion while the contents were bubbled through the isooctane. Figure 6-11 shows a TEM image of the particles precipitated from the isooctane dispersion, confirming the successful dispersion of silver particles in neat CO<sub>2</sub>. This is the first report of metallic nanoparticles dispersed in pure CO<sub>2</sub> without the use of fluorinated ligands. While there have been several reports of stably dispersed metal nanoparticles without fluorinated ligands in water in CO<sub>2</sub> microemulsions (Holmes et al. 1999; Ji et al. 1999; McLeod et al. 2003), the studies required a second phase, water, and still used fluorinated surfactants. The current study is unique in that it allowed the elimination of all fluorinated compounds and required only one continuous phase. The reason the particles are able to be dispersed is because of the ability of CO<sub>2</sub> to interact with the highly branched tails of iso-stearic acid. To remove the particles from a surface, the solvation of the tails by CO<sub>2</sub> molecules must be sufficient to overcome the attractive forces between the surface and the metallic particles. A peak for the re-dispersion of the iso-stearic acid coated silver particles from a polystyrene surface was observed after 3 days. This again shows the stability of the dispersion. Interestingly, the UV-vis

spectrum for the re-dispersion of the iso-stearic acid coated silver particles from a glass surface showed no observable peak for silver particles even after long periods of time. In addition, the silver particles could not be dispersed from a stainless steel surface. This provides an indication that the relative strength of these interactions between the ligand tails and the CO<sub>2</sub> solvent are important in this redispersion process. Changes in the surface material from quartz to polystyrene to glass clearly impact the ability of CO<sub>2</sub> to disperse these metal nanoparticles. The CO<sub>2</sub>-ligand tail interaction is barely sufficient to disperse silver nanoparticles from quartz, as is demonstrated by the small particle sizes dispersed. The presence of impurities in glass results in a subtle enhancement in the ability of glass to interact with the ligand tails over quartz, which prevents the CO<sub>2</sub>-ligand tail interactions from re-dispersing the particles. In the case of the stainless steel surface, the Van der Waals forces between the metal nanoparticles and the metal are too large to be overcome by the CO<sub>2</sub> solvation of the ligand tails.

Instead of simply dispersing particles in CO<sub>2</sub> that had been synthesized in an organic solvent, the favorable interactions between CO<sub>2</sub> and the isostearic acid ligand tails were used to accomplish a one-step synthesis and stabilization of silver nanoparticles without any fluorinated compounds. The CO<sub>2</sub>-soluble salt, Ag-AOT-TMH (Eastoe et al. 2001, Johnston et al. 2001, Fan et al. 2005), was chosen as the silver nanoparticle precursor. Its structure is shown in Figure 6-12. The molecule is a branched compound with methylated tails. As discussed for the case of isostearic acid, these branched methylated tails lead to higher CO<sub>2</sub>-tail solvation and smaller tail-tail interactions. These effects lead to higher solubility in CO<sub>2</sub>. The phase behavior for Ag-AOT-TMH was performed by Fan et al. (Fan et al. 2005), and is shown in Figure 6-13 for reference. The

only difference between the AOT-TMH and the Ag-AOT-TMH is a change in the cation, so the similarity between the solubility of the two compounds is expected. Because of the branched methylated tails, the cloud point pressure for these compounds at low weight percentages is low, reflecting their high solubility in dense CO<sub>2</sub>. This phase behavior data was collected at 313 K, while our experiments were conducted at 295 K. Less than 100 bar is needed to dissolve the 0.06 wt% Ag-AOT-TMH that was used in our experiments at 313 K. To dissolve the solids the vessel was pressurized to 206 bar at 295 K. No solid was observed in the vessel after mixing and silver nanoparticles were formed, indicating that the Ag-AOT-TMH was sufficiently soluble in CO<sub>2</sub> at the experimental conditions used. Because of its relatively high solubility in CO<sub>2</sub>, Ag-AOT-TMH was chosen as a non-fluorinated precursor for the formation of silver nanoparticles in CO<sub>2</sub>.

The one-step synthesis and stabilization of silver nanoparticles in pure CO<sub>2</sub> as described above took advantage of the solubility of Ag-AOT-TMH and isostearic acid in CO<sub>2</sub>. The UV-vis absorbance spectra for silver nanoparticles synthesized in CO<sub>2</sub> with 10% cyclohexane co-solvent by volume are shown in Figure 6-14. The absorbance corresponding to the presence of silver nanoparticles decreases with time. This decrease we attribute to the growth of particles in size with time. Any particles not completely capped by isostearic acid can agglomerate to form larger particles. When the particles become too large to be supported by the CO<sub>2</sub>/cyclohexane mixture, the particles settle and precipitate. After 5 days, the peak remained constant, indicating a stable dispersion of silver nanoparticles. A TEM image of the particles obtained from this dispersion is shown in Figure 6-15. These particles were collected after 24 hours by a simple spray

directly onto the TEM grid surface by a depressurization of the high-pressure vessel. The image is taken at a magnification of 100k and clearly shows the presence of nanoparticles. In this experiment, we have still used an organic co-solvent to promote the stabilization of the formed nanoparticles.

In order to make the process greener, we completely removed the organic co-solvent. The UV-vis absorbance spectrum for silver nanoparticles synthesized in pure CO<sub>2</sub> is shown in Figure 6-16. As was observed with the presence of co-solvent, the absorbance peak corresponding to the presence of silver nanoparticles decreased with time as larger particles were unable to remain dispersed in the pure CO<sub>2</sub> phase. After 3 days, the absorbance ceased to change, indicating a stable dispersion of silver nanoparticles. Figure 6-17 shows a TEM image of the silver nanoparticles recovered from the CO<sub>2</sub> phase by spraying onto a TEM grid. These particles were collected 3 days after synthesis in pure CO<sub>2</sub> at 295 K and 276 bar. The image is taken at a magnification of 80k and shows silver nanoparticles. The average size of these particles is less than 2 nm. The reason for the small size of the particles collected is that while it is likely larger particles were formed in the synthesis and subsequent growth, only the smallest particles were sufficiently solvated by CO<sub>2</sub> to be stably dispersed. This same effect was observed by the decrease in the magnitude of the UV-vis absorbance peak with time. These results are the first successful synthesis and dispersion of metallic nanoparticles in CO<sub>2</sub> without the use of any fluorinated compounds. Additionally, no organic solvents were required during the synthesis or dispersion.

One factor that had a significant impact on the nanoparticle dispersion was the presence of cyclohexane as a co-solvent. Figure 6-18 shows a comparison of UV-vis

absorbance spectra with 0, 2, and 10% cyclohexane co-solvent by volume in CO<sub>2</sub> at 295 K and 276 bar. The dotted line corresponds to the UV-vis absorbance collected 5 days after silver nanoparticles were synthesized in CO<sub>2</sub> with 10% cyclohexane co-solvent by volume, the dashed line corresponds to the UV-vis absorbance collected 3 days after particles were synthesized with 2% cyclohexane co-solvent by volume, and the solid line corresponds to the UV-vis absorbance spectrum collected 3 days after silver nanoparticles were synthesized in pure CO<sub>2</sub>. These UV-vis absorbance peaks were acquired after each system had reached a stable dispersion. Although a stable dispersion of silver nanoparticles was obtained in pure CO<sub>2</sub>, the addition of a small amount of cyclohexane co-solvent (up to 10% by volume) significantly enhanced the dispersability of the isostearic acid coated silver nanoparticles in CO<sub>2</sub>. Cyclohexane solvates the ligand tails much better than CO<sub>2</sub>, greatly increasing the solvent strength, and consequently the number of particles that can be stabilized in the mixture.

Another factor that was examined was the effect of pressure (or density) at constant temperature on the dispersability of particles formed by reduction in CO<sub>2</sub>. UV-vis absorbance spectra for dispersions of silver nanoparticles at different pressures (or densities) at 295 K are shown in Figure 6-19. These particles were synthesized by reduction in CO<sub>2</sub> with 10% cyclohexane co-solvent by volume at 295 K and 276 bar. This system was chosen because it had the largest concentration of dispersed particles, making changes in the concentration of dispersed particles easier to distinguish. After synthesis, the UV vessel was depressurized to 106 bar. Once a stable dispersion was achieved, the pressure (or density) of the mixture was increased by adding more CO<sub>2</sub>. At each pressure, the system was given enough time for the UV-vis absorbance to not

change appreciably. This time was typically less than one hour. At this time the UV-vis absorbance was recorded and the pressure increased. This process was repeated for 6 pressures until the mixture was returned to the starting point of 276 bar. These spectra are shown in Figure 6-19. As the pressure (or density) of the system was increased, the absorbance peak also increased. This increase corresponds to an increase in the concentration of dispersed particles with an increase in density. By increasing the density at a constant temperature, the solvent strength of the system improves as CO<sub>2</sub> more effectively solvates the isostearic acid ligand tails. This makes the solvent strength of the mixture better, resulting in a higher concentration of stably dispersed silver nanoparticles.

While these particles were all formed in the liquid phase at 295 K and 276 bar, the true processing advantages of CO<sub>2</sub> systems lie in the supercritical phase. To take advantage of the high diffusivities and the absence of surface tension and phase interfaces that greatly aid in nanoparticle processing, these particles must be dispersed in the supercritical phase. After forming the particles in neat CO<sub>2</sub> at 295 K and 276 bar and waiting for a stable dispersion, the temperature of the system was increased to 298 K, 303 K, and 308 K at constant density. Once each temperature was reached, no change was observed in the UV-vis absorbance spectrum for 1 hour. This time was chosen because the system stabilized at all pressures at constant temperature in less than 1 hour during the investigations of the effect of pressure (or density) on the dispersions. For 298 K, 303 K, and 308 K, there was no observable change in the UV-vis absorbance spectrum at constant density. Therefore, the silver nanoparticles can be synthesized in liquid CO<sub>2</sub> and then processed in the supercritical phase by a simple increase in the temperature.

## Conclusions

Silver nanoparticles coated with iso-stearic acid were dispersed either in pure CO<sub>2</sub> from a surface or sprayed into dense CO<sub>2</sub> using hexane. Both of these results are the first demonstrations of stable nanoparticle dispersions in a continuous CO<sub>2</sub> phase without the use of fluorinated surfactants or capping ligands. These dispersions are stabilized by molecular interactions between the isostearic acid ligand tails and CO<sub>2</sub>. Silver nanoparticles have been synthesized and stabilized in a one-step process in CO<sub>2</sub> for the first time without using any fluorinated compounds or organic solvents. The dispersion can be significantly enhanced by the addition of small amounts of cyclohexane co-solvent. Increases in pressure (or density) at a constant temperature also increase the concentration of dispersed particles. By a simple increase in temperature, the particles dispersed in the liquid CO<sub>2</sub> phase can be processed in the supercritical phase. These results are only possible because of the ability of CO<sub>2</sub> to effectively solvate the isostearic acid ligand tails.

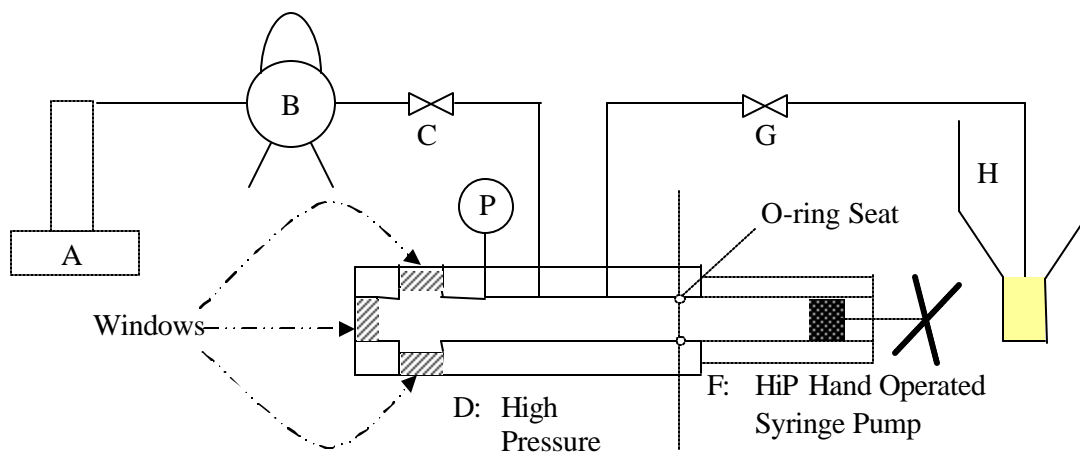


**Figure 6-1.** Schematic diagram of the setup used to concentrate the silver particles dispersed in a hexane/CO<sub>2</sub> mixture (10% hexane by volume). A represents an ISCO 260D syringe pump, B represents a 6-port injection valve, C represents a high-pressure needle valve, D represents a variable volume high-pressure UV-vis vessel with 3 quartz windows, E represents a movable piston, F represents a high-pressure hand-operated syringe pump, G represents a high-pressure needle valve, and H represents a collection vessel. The yellow portion in the bottom of the collection vessel is hexane chilled by ice water.

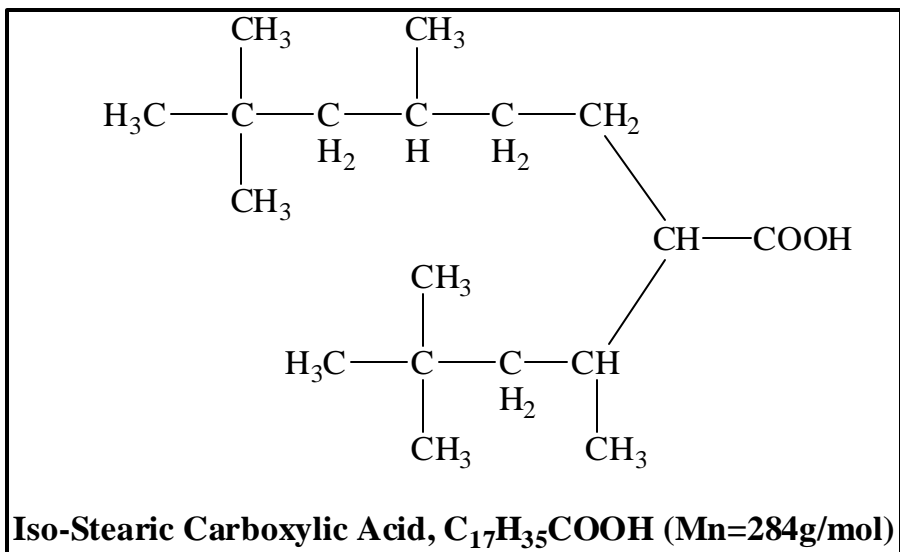


**Figure 6-2.** Molecular structure of iso-stearic acid. Mn=284 g/mol.

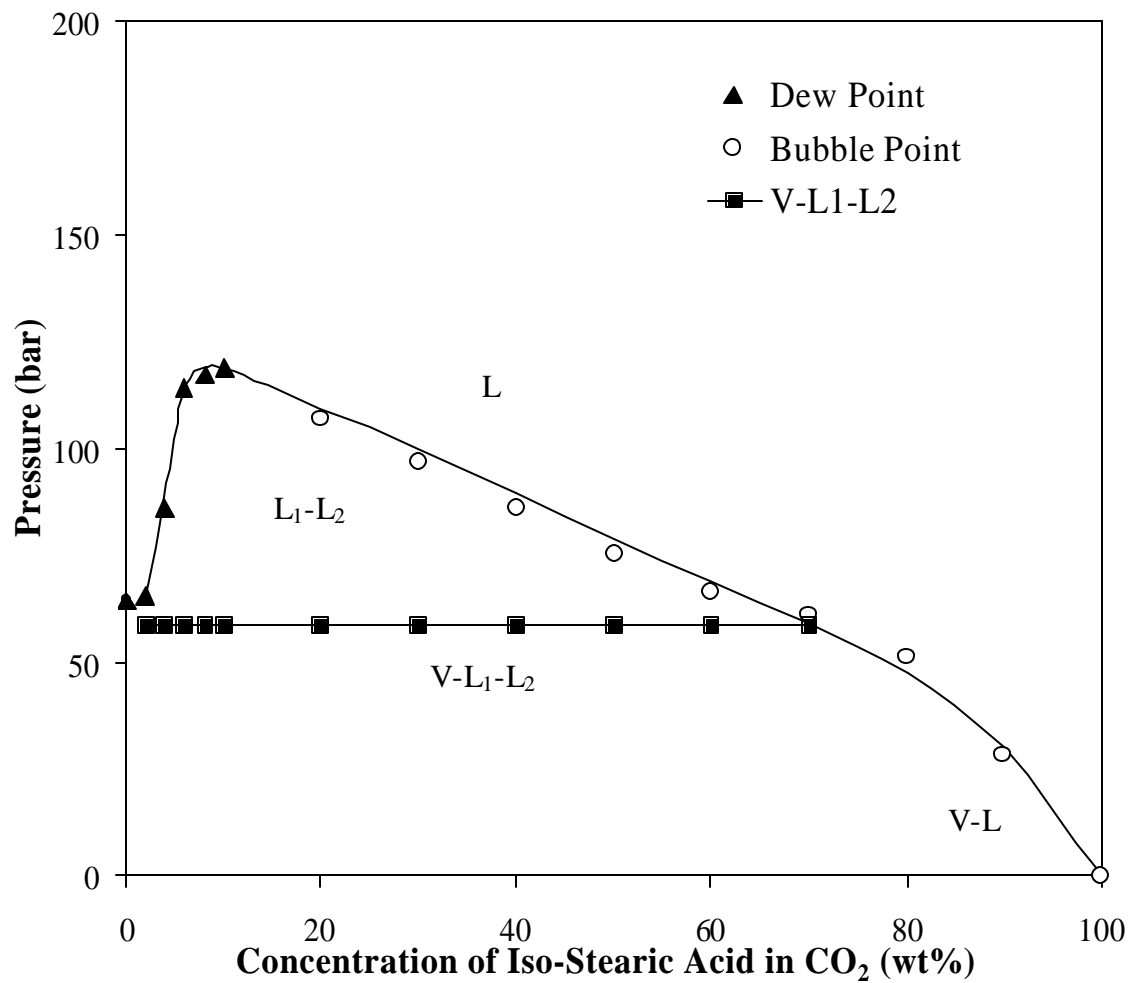


**Figure 6.3.** Phase Behavior of Iso-Stearic Acid/CO<sub>2</sub> Mixture at 295 K. No data was collected for the small VL1 two phase region at the CO<sub>2</sub>-rich end of the diagram.

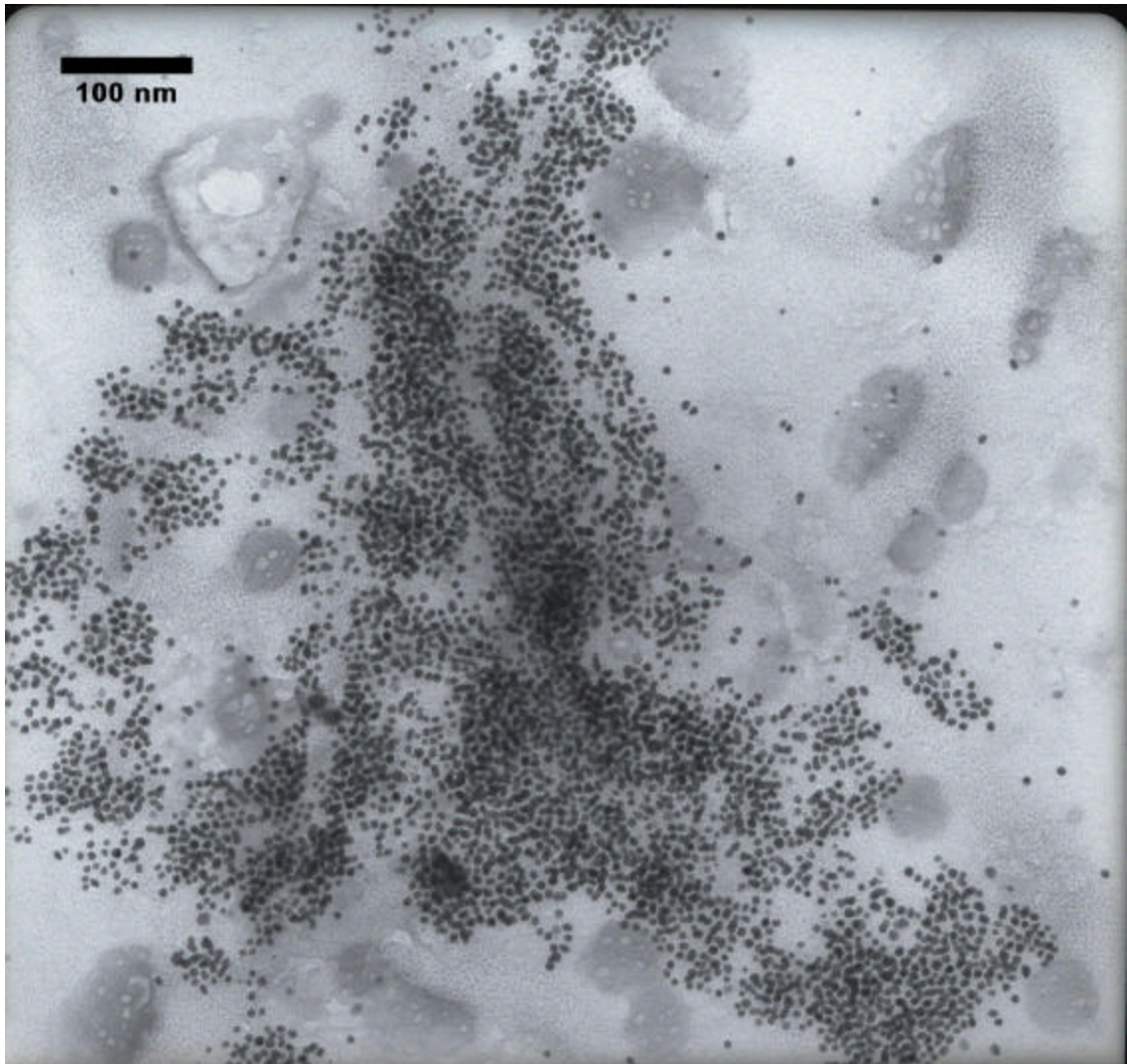


**Figure 64.** TEM image of iso-stearic acid coated silver particles precipitated from a hexane dispersion.

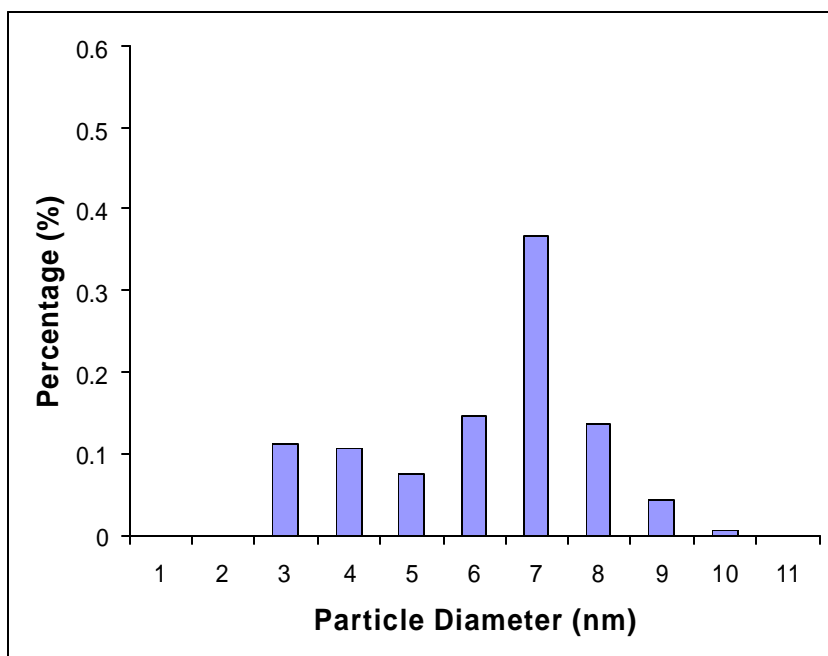


**Figure 6-5.** Particle size distribution of the iso-stearic acid coated silver nanoparticles.

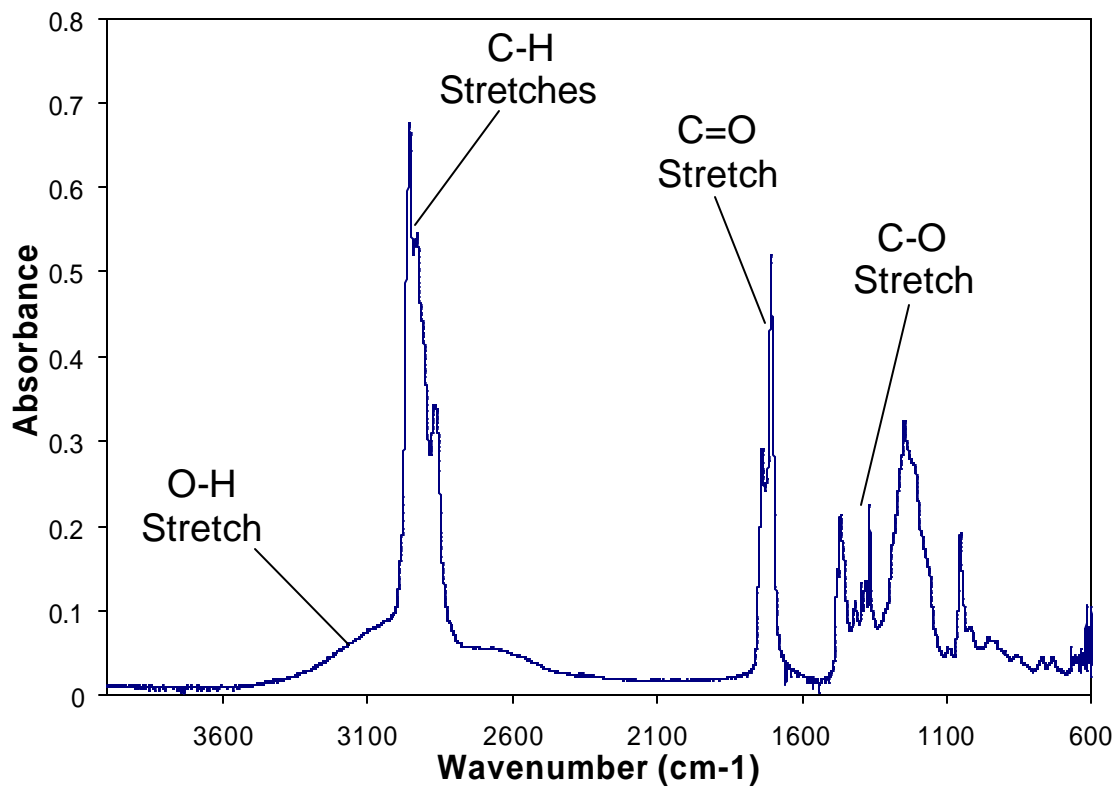


**Figure 6-6.** ATR-FTIR spectrum of iso-stearic acid coated silver nanoparticles.

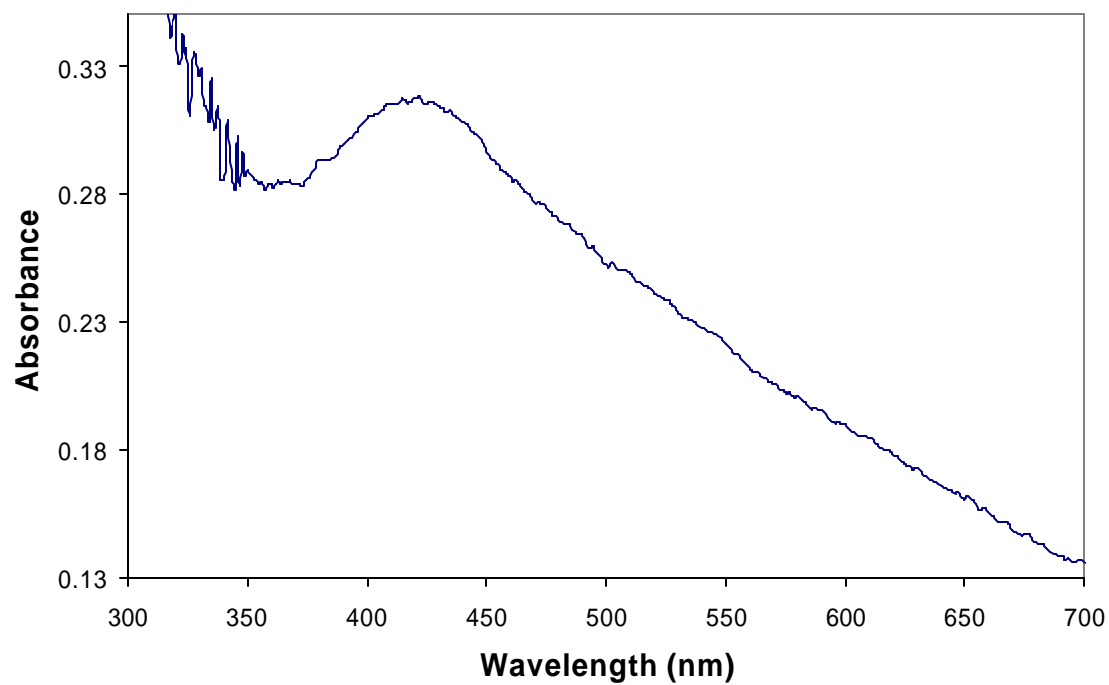


**Figure 67.** UV-vis spectrum of iso-stearic acid coated silver particles dispersed in a hexane-CO<sub>2</sub> mixture (11% hexane by volume) at 276 bar and 295 K. This spectrum was collected 4 hours after the introduction of CO<sub>2</sub> solvent and is baseline corrected.

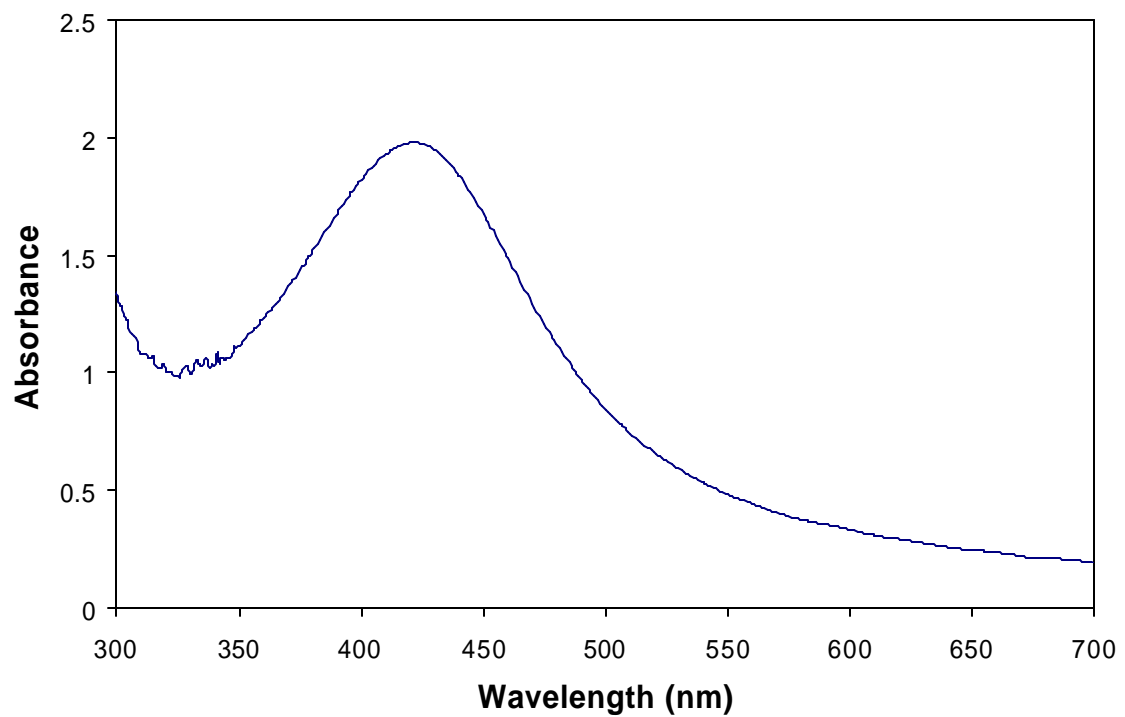


**Figure 6-8.** UV-vis spectrum of iso-stearic acid coated silver particles recovered from a hexane-CO<sub>2</sub> mixture (10% hexane by volume) at 276 bar and 295 K in hexane.

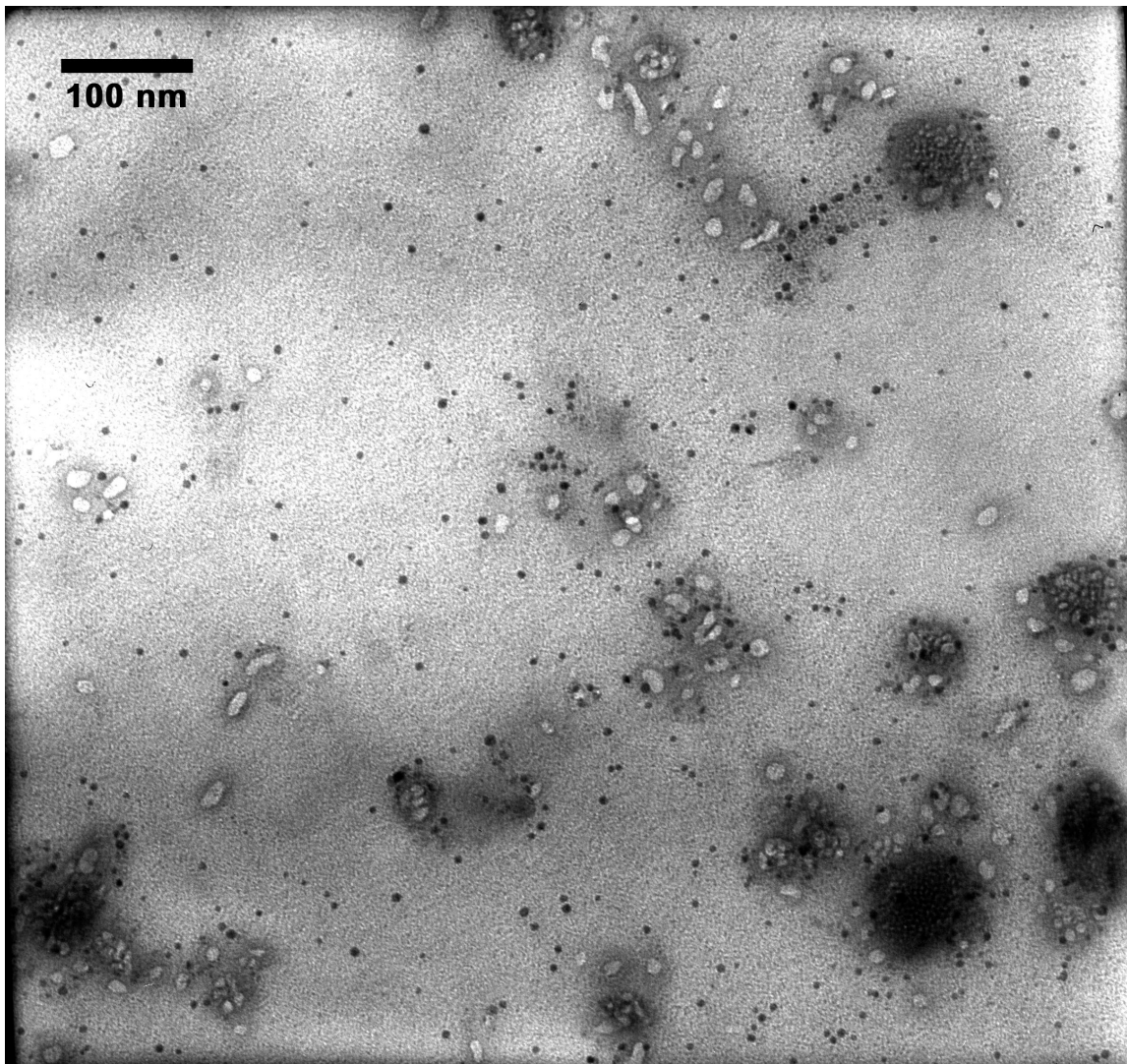


**Figure 6-9.** TEM image of iso-stearic acid coated silver particles recovered from a hexane-CO<sub>2</sub> mixture (10% hexane by volume) at 276 bar and 295 K in hexane.

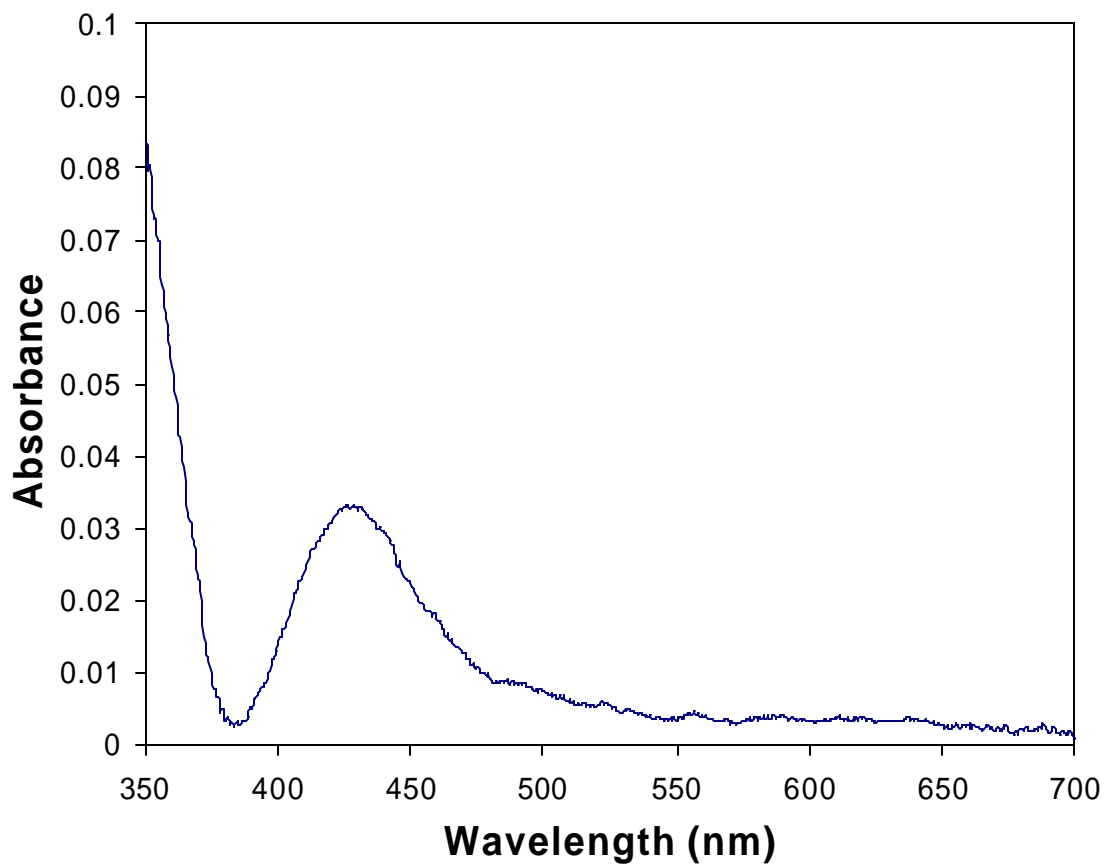


**Figure 6-10.** UV-vis spectrum of silver particles dispersed off of a quartz surface in CO<sub>2</sub> at 276 bar and 295 K. This spectrum is taken after 17 hours and has been baseline corrected.

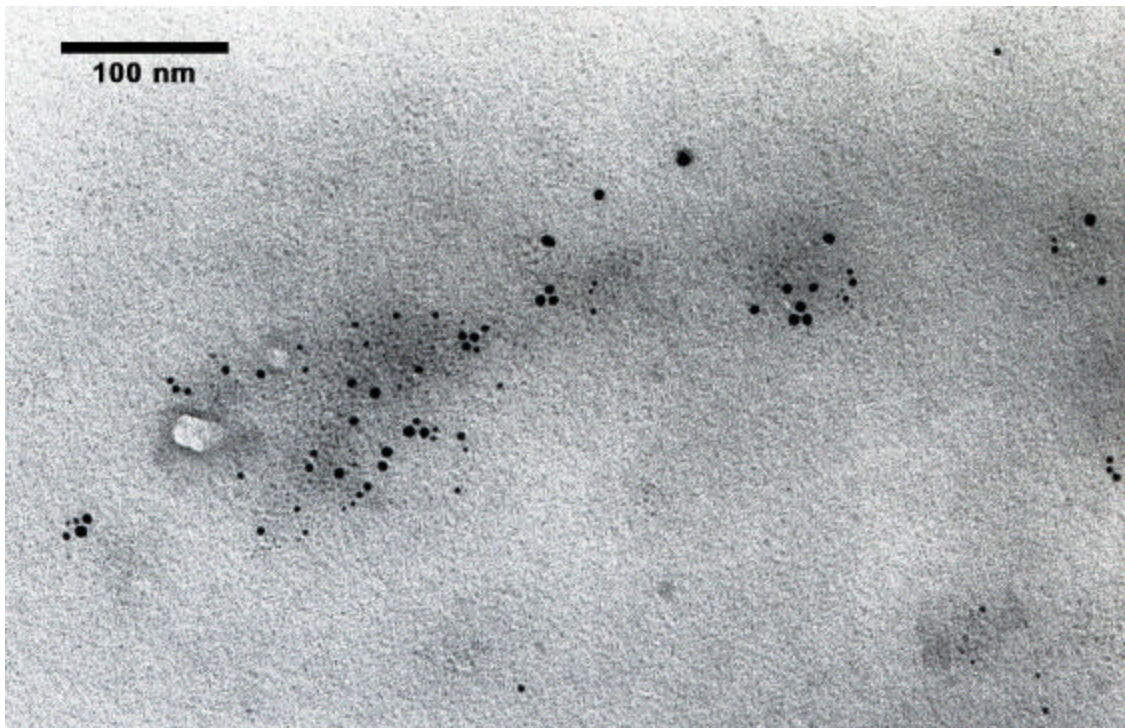


**Figure 6-11.** TEM image of iso-stearic acid coated silver particles recovered from CO<sub>2</sub> at 276 bar and 295 K in hexane.

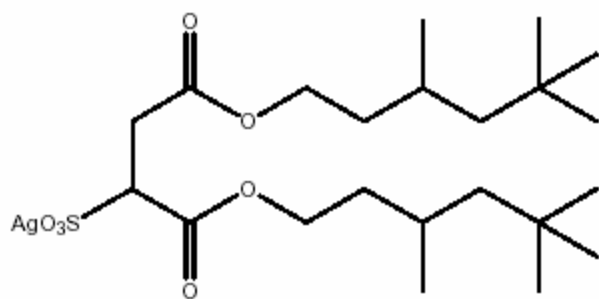


**Figure 6-12.** Molecular structure of Ag-AOT-TMH (Fan et al. 2005).

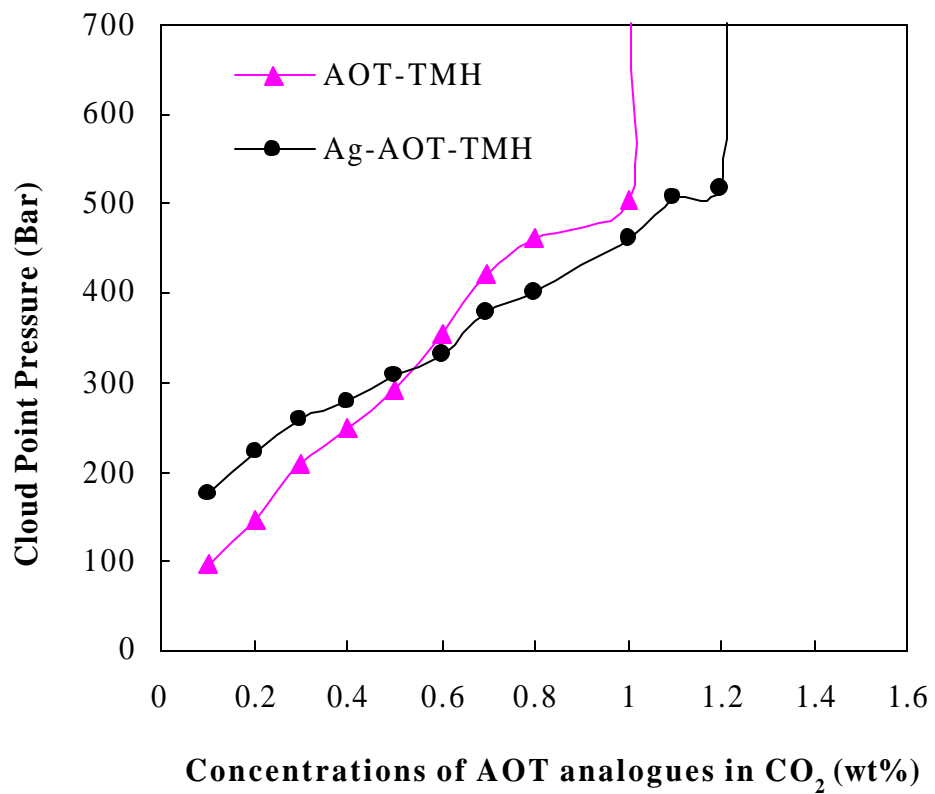


**Figure 6-13.** Phase behavior of AOT-TMH and Ag-AOT-TMH at 40 °C (Fan et al. 2005).

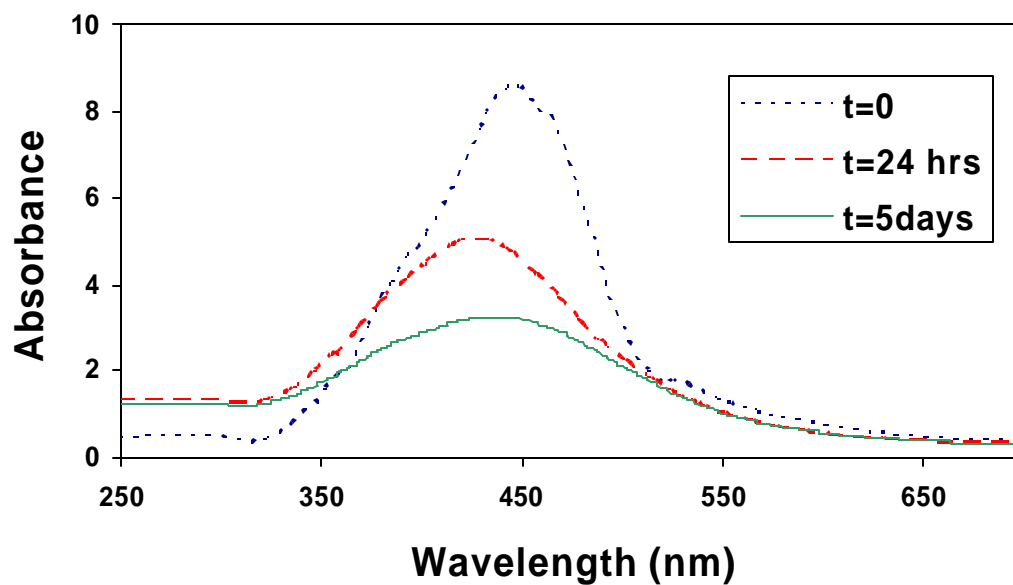


**Figure 6-14.** Uv-vis spectra of silver nanoparticles formed in CO<sub>2</sub> with 10% cyclohexane co-solvent at 295 K and 276 bar. The spectra have been scaled to have an absorbance of 0 at 700 nm for comparison. The dotted line corresponds to the initial absorbance, the dashed line to the absorbance after 24 hours, and the solid line to the absorbance after 5 days.

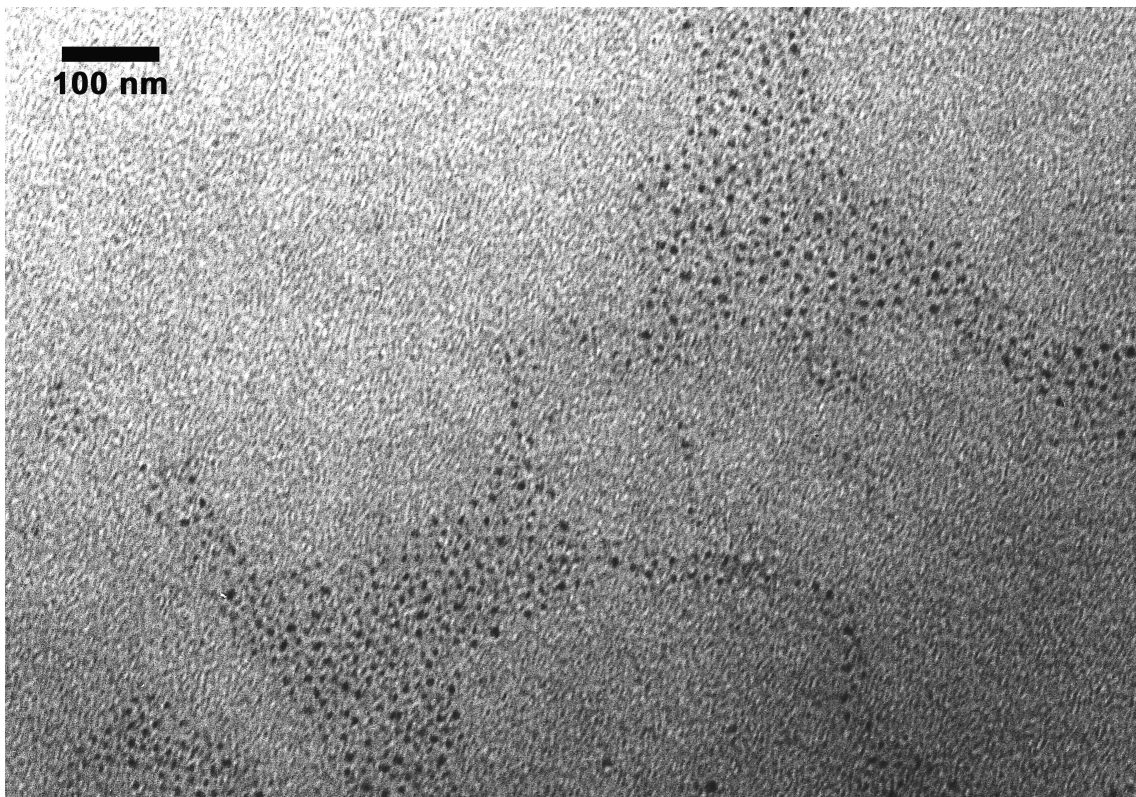


**Figure 6-15.** TEM image of silver nanoparticles collected from a 10% cyclohexane in CO<sub>2</sub> mixture at 295 K and 276 bar. These particles were collected by directly spraying the contents of the vessel onto the TEM grid by depressurization.

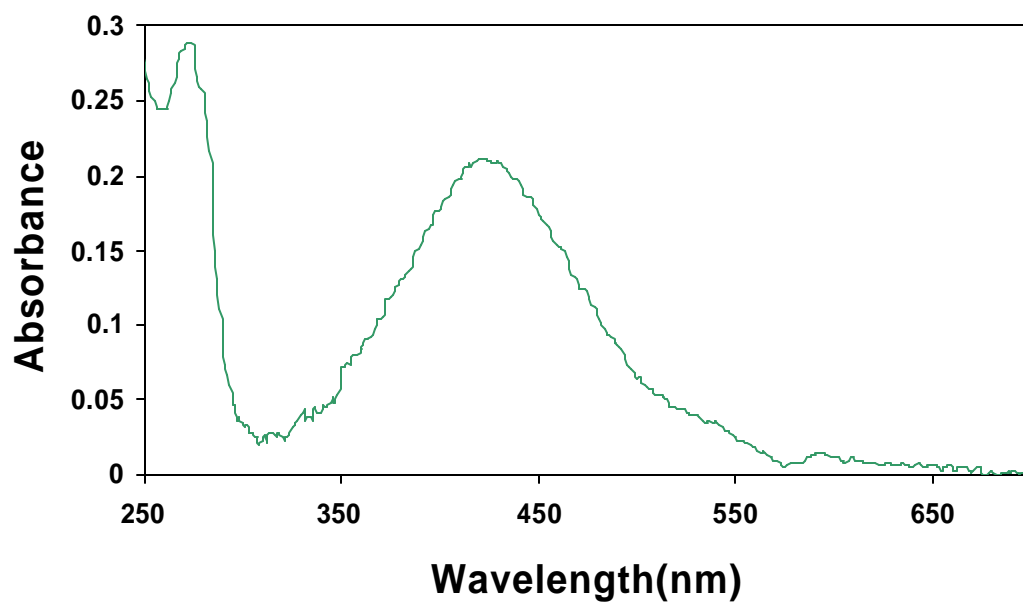


**Figure 6-16.** UV-vis absorbance spectrum of silver nanoparticles synthesized in neat CO<sub>2</sub> collected after 3 days.

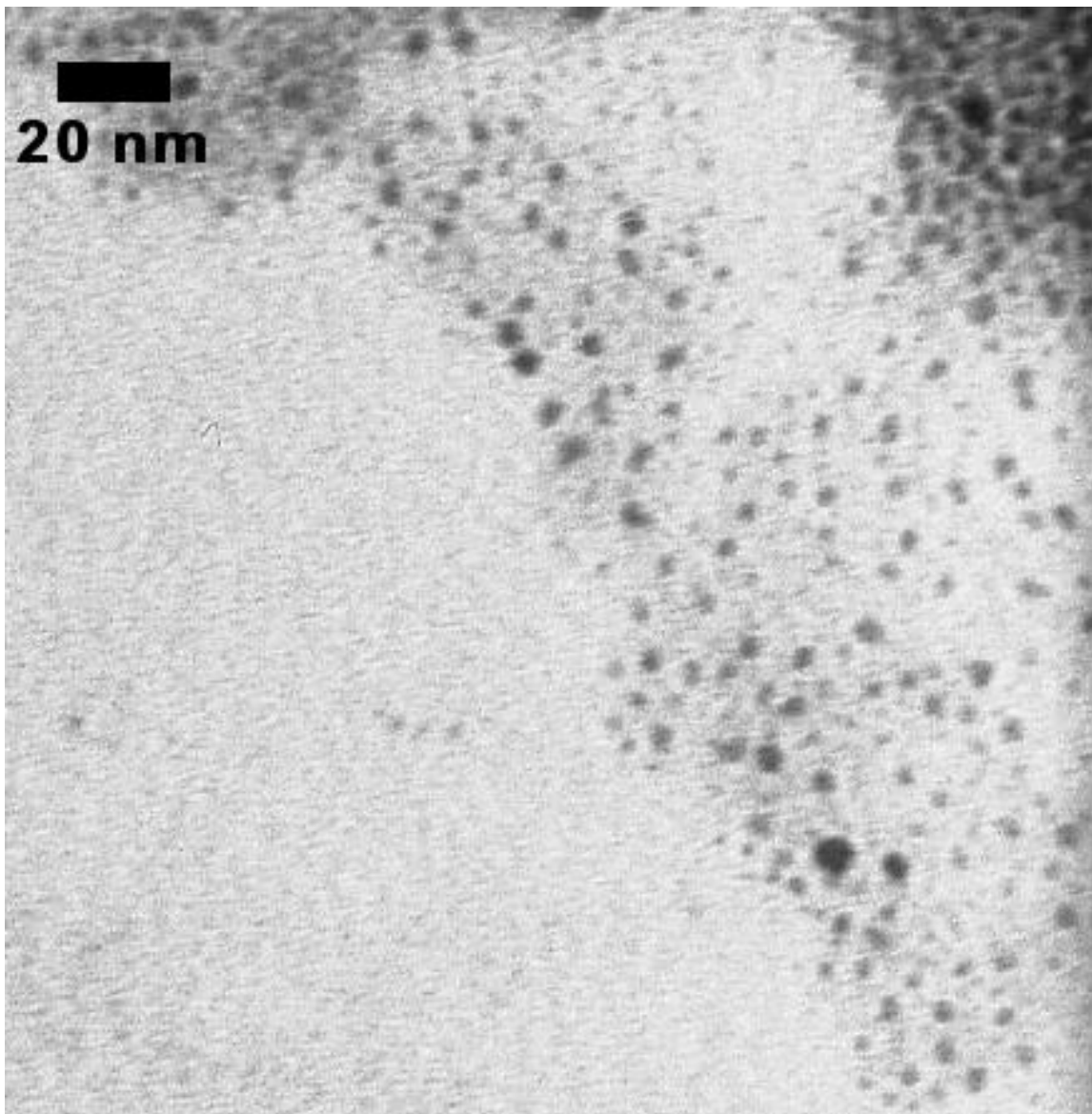


**Figure 6-17.** TEM image of silver nanoparticles collected from pure CO<sub>2</sub> at 295 K and 276 bar. These particles were collected by directly spraying the contents of the vessel onto the TEM grid by depressurization.

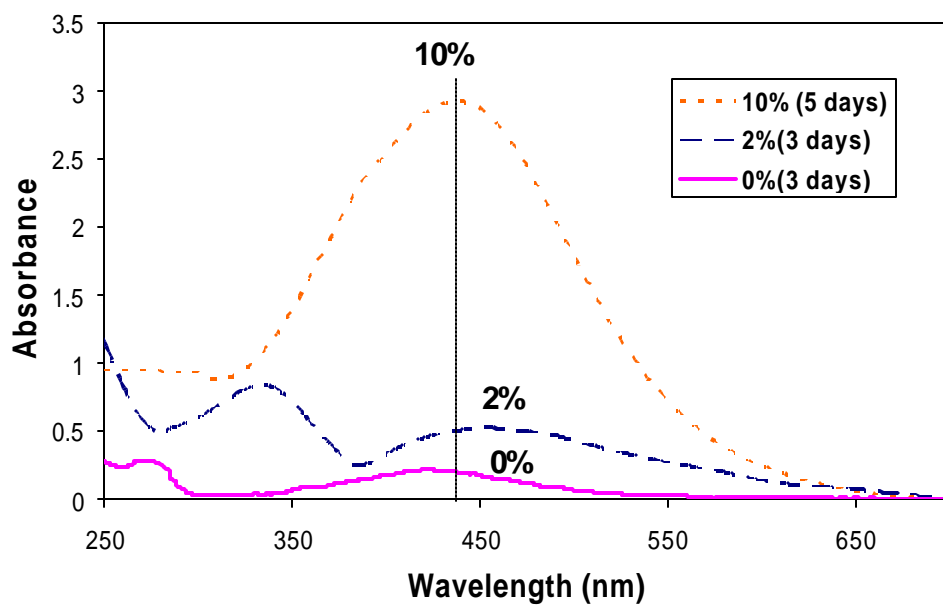


**Figure 6-18.** UV-vis absorbance spectra of nanoparticles synthesized in CO<sub>2</sub> at 295 K and 276 bar. The dotted line corresponds to 10% cyclohexane co-solvent by volume, the dashed line to 2% cyclohexane co-solvent by volume, and the solid line to no added cosolvent.

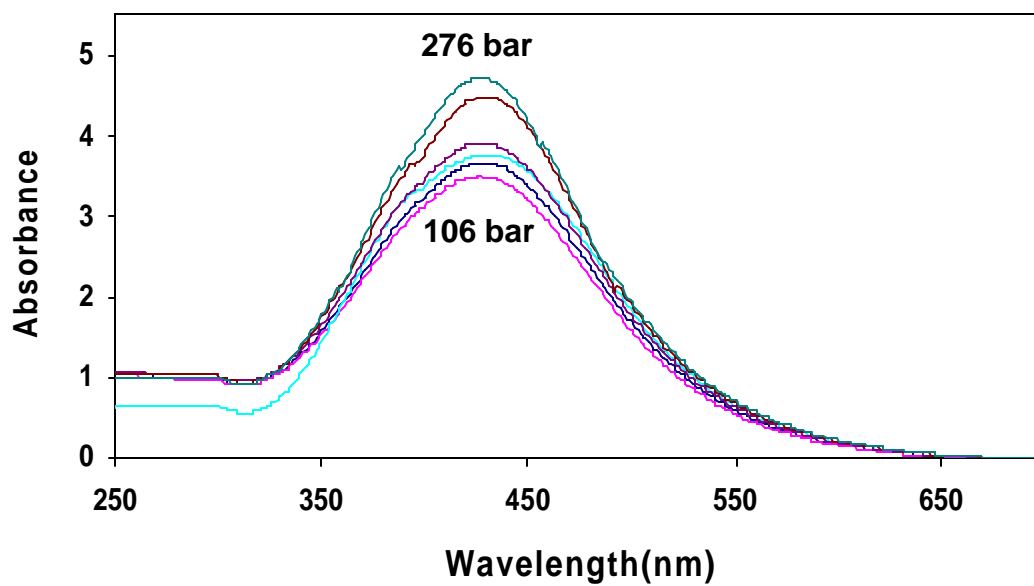


**Figure 6-19.** UV-vis absorbance spectra for silver nanoparticles dispersed in CO<sub>2</sub> at 295 K with 10% cyclohexane co-solvent by volume. Each curve corresponds to a different pressure going from the bottom curve (106 bar) to the top curve (276 bar).

## CHAPTER 7

### CONCLUSIONS

#### **IR Studies of Carbon Dioxide Effects on Carboxylic Acid Dimerization Constants**

Fundamental IR studies were done to explore the nature of the interaction between CO<sub>2</sub> and carboxylic acids. Both formic acid and propionic acid hydrogen-bonding studies showed that the monomer form was much more stabilized in CO<sub>2</sub> than in ethane relative to the dimer. As the density of the CO<sub>2</sub> solvent increased, the equilibrium constant decreased strongly, due to the existence of a specific interaction between the acids and the CO<sub>2</sub> solvent. Whereas, the equilibrium constant remained relatively constant as ethane density was increased. The density dependence for hydrogen-bonding was modeled using MLFHB theory, which suggested that both the acid monomers were stabilized by roughly the same amount relative to the acid dimers as the CO<sub>2</sub> density is increased. Therefore, the carbon number seems to have little effect on the specific interactions of CO<sub>2</sub> with the acid functional group, suggesting no difference in steric hindrance. TFA did not exist purely as a monomer / cyclic dimer equilibrium in all conditions. Studies showed the existence of a third peak in CO<sub>2</sub> at a low temperature (298 K) and high densities (0.781 - 0.816 g/cm<sup>3</sup>) which corresponded to the linear dimer of TFA. All of these results suggest that a combination of Lewis acid-Lewis base

interactions between the carbon on CO<sub>2</sub> and the carbonyl oxygen on the acids and between an oxygen on CO<sub>2</sub> and the acidic proton on the acids act to stabilize the monomer. However, the interaction of the CO<sub>2</sub>, acting as a Lewis base, with the acidic proton seems to be the dominant solvent-solute interaction. As a result, the ability of CO<sub>2</sub> to act both as a Lewis base (this study) and as a Lewis acid (Meridith et al. 1996) and to have significant interactions should be taken into account when designing CO<sub>2</sub>-soluble molecules.

### **NMR Investigations of Specific Interactions between Carbon Dioxide and Carboxylic Acids**

The reported evidence of an electronic interaction involving the acid proton could be the result of an acid – base interaction with the CO<sub>2</sub> solvent. Unfortunately, there is the self-association of formic acid which confounds the problem. Ideally, there would be two distinct NMR resonance bands for the acid proton. One peak would be for the acid monomer and the other for the acid dimer. Since the acid monomer would be able to interact with the CO<sub>2</sub>, but not the acid dimer, the monomer peak should shift at a different rate with density than ethane, while the dimer peak should shift at the same rate as the ethane peak. Because the cell was not spun and the temperature was high to allow for a wide density range, the dimerization equilibrium was too fast to be distinguished at the NMR timescale used. This resulted in a broad hump rather than two distinct peaks that changed with density. The average peak shift, as reported, can also not be used to determine if there is an interaction with CO<sub>2</sub> because the dimerization equilibrium is density dependent in CO<sub>2</sub>. As a result, the effects of specific interactions with CO<sub>2</sub> are indistinguishable from the change in equilibrium constant for the formic acid system.

This problem is not unique to formic acid, but to carboxylic acids in general. To probe the ability of CO<sub>2</sub> to act as a Lewis base, a molecule with a relatively strong Lewis acid group that cannot hydrogen bond with itself should be used. Such a molecule would allow for an experimental determination of the ability of CO<sub>2</sub> to act as a Lewis base.

### **High-Resolution Imaging of the Supercritical Antisolvent Process**

One key application that utilizes interactions with CO<sub>2</sub> is the precipitation of various molecules insoluble in CO<sub>2</sub> into particles by using the CO<sub>2</sub> as an antisolvent to dissolve the solvent carrying the insoluble molecules. A technique for the visualization of particle formation processes in supercritical fluids was developed. The PCA process was imaged with a high magnification and high resolution imaging system that allowed for the observation of particle and droplet evolution. Images were captured that provided information on jet breakup, particles, particle agglomeration, droplet size and morphology, and jet flow phenomena. The jet breakup length was measured in several experiments, as well as droplet and particle diameters. The system is capable of achieving magnifications ranging from 1.28  $\mu\text{m}/\text{pixel}$  to 0.21  $\mu\text{m}/\text{pixel}$ . These high magnifications and resolutions for imaging these high pressure particle production processes are paramount to study the system dynamics.

Although image processing and further experiments are needed to make quantitative conclusions, there are several observations of importance. First, we observed conditions in which no droplets formed (high CO<sub>2</sub> densities). Particles were formed in this kind of process, and therefore were the result of nucleation and growth within gas-like shear layers, as suggested by Lengsfeld (Lengsfeld et al. 2000). At low CO<sub>2</sub>

densities, however, we observed droplet formation that occurred by atomization as predicted by Dixon et al. (Dixon et al. 1993) and Randolph et al. (Randolph et al. 1993). The jet breakup lengths measured for pure solvent agreed well with those predicted by Lengsfeld et al. (Lengsfeld et al. 2000). Although a relatively uniform particle size distribution was obtained for PLA, the images showed a wide range of droplet sizes at several positions in the jet spray. These results show that there is not a direct correlation between droplet size and distribution and particle size and distribution. In some cases, especially for budesonide solutions injected into CO<sub>2</sub>, non-spherical droplets were observed indicating the effect of viscous forces. The video (time sequence images) allowed us to observe that the flow developed very quickly. For the 1 weight percent solution of PLA, the spray was fully developed after 1 second. By sizing the droplets formed in the precipitation process at each position, we saw that the droplets swelled as they moved away from the nozzle as predicted by Randolph et al. (Randolph et al. 1993) and Werling and Debenedetti (Werling and Debenedetti 1999). Again, a very large range of droplet sizes at each position was observed.

This study has only imaged the SAS process for one specific set of experimental conditions. Several changes in the overall formation process are to be expected with changes in the processing parameters. For instance, Werling and Debenedetti (Werling and Debenedetti 2000) suggest that no droplets are formed when the solvent is miscible with the antisolvent. This miscibility is achieved as the mixture of the two fluids is brought to its supercritical state. Thus, by raising temperature and pressure, droplet formation would cease due to complete miscibility. By changing both the operating pressure and the operating temperature, changes in droplet formation and behavior may

be examined. Another important process parameter to examine is the flow rate of the liquid solution. Changing the flow rate of the solution changes the Reynolds number and the Weber number. These changes affect the spray characteristics and may result in faster or slower jet breakup into droplets. To further address the underlying thermodynamics and mass transport in the SAS process, it would be useful to track individual droplets. This can be achieved by using a CCD camera with a higher frame rate such that a single droplet will appear in the focal plane for more than one successive frame. A higher frame rate would allow for a more detailed view of droplet behavior. It may be possible to image droplets coalescing, dividing, or even disintegrating into particles. To examine the mass transport, another future modification would be to use a dye in the solvent. In this way, the relative concentration profile of the liquid solvent may be monitored with time. To study particle formation dynamics, the polymer solute may be modified to include a fluorescent group. Using a laser to induce fluorescence, the behavior of the solutes may also be monitored to give thermodynamical information about their formation process. A combination of all of these modifications would result in a more complete understanding of the SAS process.

### **Polymerization and Precipitation during the Supercritical Antisolvent Precipitation Process**

Two new methods for polymerization have been developed. The reaction of caprolactam with CO<sub>2</sub> and polymerization followed by precipitation during the SAS process was explored. The addition of TiO<sub>2</sub> particles caused the product to form spheres instead of spheres and particles. Product analysis suggested that the product was a mixture of the caprolactam and nylon 6. A second polymerization reaction involving the

sonication induced free radical polymerization of MAA to PMAA during the SAS-EM process was also explored. The product is believed to be pure PMAA. These results produced limited quantities of product. Future experiments must be performed to advance the development of these novel processes. A mass transport model for the polymerization of caprolactam in the SAS process was also developed for a position in the spray well away from the spray entrance where the droplets are well separated. These processes are only possible because of the interactions of the monomers with the CO<sub>2</sub> to form the polymers. In the case of caprolactam, it is a reaction with CO<sub>2</sub>. The CO<sub>2</sub> dissolves MAA, due to interactions with the carboxylic acid group, allowing the polymerization to occur. In each case, the product is insoluble in CO<sub>2</sub>, making product recovery simple.

### **Stable Dispersions of Silver Nanoparticles in Carbon Dioxide with Fluorine-Free Ligands**

Silver nanoparticles coated with iso-stearic acid were dispersed either in pure CO<sub>2</sub> from a surface or sprayed into dense CO<sub>2</sub> using hexane. Both of these results are the first demonstrations of stable nanoparticle dispersions in a continuous CO<sub>2</sub> phase without the use of fluorinated surfactants or capping ligands. These dispersions are stabilized by molecular interactions between the isostearic acid ligand tails and CO<sub>2</sub>. Silver nanoparticles have been synthesized and stabilized in a one-step process in CO<sub>2</sub> for the first time without using any fluorinated compounds or organic solvents. The dispersion can be significantly enhanced by the addition of small amounts of cyclohexane co-solvent. Increases in pressure (or density) at a constant temperature also increase the concentration of dispersed particles. By a simple increase in temperature, the particles

dispersed in the liquid CO<sub>2</sub> phase can be processed in the supercritical phase. These results are only possible because of the ability of CO<sub>2</sub> to effectively solvate the isostearic acid ligand tails. Further understanding of the solvent nature of CO<sub>2</sub> will lead to the development of more CO<sub>2</sub>-soluble ligands and surfactants for use in nanomaterial synthesis, dispersion, and processing in CO<sub>2</sub>.

## **Conclusion**

Molecular interactions involving CO<sub>2</sub> are of critical importance in supercritical fluid processes and nanoparticle processing. This dissertation has examined specific interactions between CO<sub>2</sub> and carboxylic acids in a fundamental manner using FTIR and NMR spectroscopy. The effects of interactions on solubility in the SAS process were examined by high resolution imaging. Specific interactions of CO<sub>2</sub> with secondary amines and carboxylic acids were exploited in two new polymerization techniques which occur during the SAS process. Finally, the ability of CO<sub>2</sub> to effectively solvate the branched, methylated tails of isostearic acid and Ag-AOT-TMH was used to synthesize and stably disperse silver nanoparticles in CO<sub>2</sub> without the need for fluorinated compounds. Further understanding of the solvent nature of CO<sub>2</sub> is critically important to make full use of the processing advantages CO<sub>2</sub> offers over traditional organic solvents. A better understanding can allow for the development of more CO<sub>2</sub>-soluble compounds.

## REFERENCES

- Adamsky, F. A.; Beckman, E. J. Inverse Emulsion Polymerization of Acrylamide in Supercritical Carbon Dioxide. *Macromolecules* **1994**, *27*, 312.
- Agrawal, A. K.; Devika, K.; Manabe, T. Simulation of Hydrolytic Polymerization of Nylon-6 in Industrial Reactors: Part I. Mono-Acid-Stabilized Systems in VK Tube Reactors. *Ind. Eng. Chem. Res.* **2001**, *40*, 2563.
- Allen, G.; Caldin, E. F. The association of carboxylic acids. *Q. Rev. Chem. Soc.* **1953**, *7*, 255.
- Angus, S.; Armstrong, B.; Reuk, K. *International Thermodynamics Tables of the Fluid State of Carbon Dioxide*; Pergamon Press: Elmsford, NY, **1976**.
- Armellini, F. J.; Tester, J. W. Precipitation of Sodium Chloride and Sodium Sulfate in Water from Sub- to Supercritical Conditions: 150 to 550°C, 100 to 300 bar. *Journal of Supercritical Fluids* **1994**, *7*, 147.
- Bai, S.; Taylor, C. M.; Mayne, C. L.; Pugmire, R. J.; Grant, D. M. A New High Pressure Sapphire Nuclear Magnetic Resonance Cell. *Rev. Sci. Instrum.* **1996**, *67*(1), 240.
- Ballard, L.; Reiner, C.; Jonas, J. High-Resolution NMR Probe for Experiments at High Pressures. *J. Magn. Reson.* **1996**, *123*, 81-96.
- Ballard, L.; Yu, A.; Reiner, C.; Jonas, J. A High-Pressure, High-Resolution NMR Probe for Experiments at 500 MHz. *J. Magn. Reson.* **1998**, *133*, 190.
- Baradie, B.; Shoichet, M. S. Synthesis of Fluorocarbon-Vinyl Copolymers in Supercritical Carbon Dioxide: Insight into Bulk Properties. *Macromolecules* **2002**, *35*, 3569.
- Baradie, B.; Shoichet, M. S. Insight into the Surface Properties of Fluorocarbon-Vinyl Acetate Copolymer Films and Blends. *Macromolecules* **2003**, *36*, 2343.
- Blatchford, M. A.; Raveendran, P.; Wallen, S. L. Raman Spectroscopic Evidence for Cooperative C-H . . O Interactions in the Acetaldehyde-CO<sub>2</sub> Complex. *J. Am. Chem. Soc.* **2002**, *124*, 14818.
- Blatchford, M. A.; Raveendran, P.; Wallen, S. L. Spectroscopic Studies of Model Carbonyl Compounds in CO<sub>2</sub>: Evidence for Cooperative C-H . . O Interactions. *J. Phys. Chem. A*, **2003**, *107*, 10311.
- Bleich, J.; Kleinebudde, P.; Muller, B. W. Influence of Gas Density and Pressure on Microparticles Produced with the ASES Process. *Int. J. Pharm.* **1994**, *106*, 77.
- Boys, S. F.; Bernardi, F. The calculation of small molecular interaction by the difference of separate total energies. Some procedures with reduced errors. *Molecular Physics*, **1970**, *19*(4), 553.
- Bukur, D. B.; Lang, X.; Akgerman, A.; Feng, Z. Effect of Process Conditions on Olefin Selectivity during Conventional and Supercritical Fischer-Tropsch Synthesis. *Ind. Eng. Chem. Res.* **1997**, *36*, 2580.

- Cai, B.; Li, J. Evaluation of trifluoroacetic acid as an ion-pair reagent in the separation of small ionizable molecules by reversed-phase liquid chromatography. *Analytica Chimica Acta* **1999**, 399, 249.
- Chattopadhyay, P.; Gupta, R. B. Supercritical CO<sub>2</sub>-Based Production of Fullerene Nanoparticles. *Ind. Eng. Chem. Res.* **2000**, 39, 2281.
- Chattopadhyay, P.; Gupta, R. B. Production of Antibiotic Nanoparticles Using Supercritical CO<sub>2</sub> as Antisolvent with Enhanced Mass Transfer. *Ind. Eng. Chem. Res.* **2001**, 40, 3530.
- Chattopadhyay, P.; Gupta, R. B. Production of Griseofulvin Nanoparticles using Supercritical CO<sub>2</sub> Antisolvent with Enhanced Mass Transfer. *Inter. J. Pharm.* **2001**, 228, 19.
- Chattopadhyay, P.; Gupta, R. B. Production of Griseofulvin Nanoparticles using Supercritical CO<sub>2</sub> Antisolvent with Enhanced Mass Transfer. *Ind. Eng. Chem. Res.* **2002**, 41(24), 6049.
- Chattopadhyay, P.; Gupta, R. B. Supercritical CO<sub>2</sub>-Based Formation of Silica Nanoparticles Using Water-in-Oil Microemulsions. *Ind. Eng. Chem. Res.* **2003**, 42, 465.
- Chavez, F.; Debenedetti, P. G.; Luo, J. J.; Dave, R. N.; Pfeffer, R. Estimation of the Characteristic Time Scales in the Supercritical Antisolvent Process. *Ind. Eng. Chem. Res.* **2003**, 42, 3156.
- Chen, A. U.; Basaran, O. A. A New Method for Significantly Reducing Drop Radius Without Reducing Nozzle Radius in Drop-on-Demand Drop Production. *Physics of Fluids* **2002**, 14(1), L1.
- Chiger, N. Optical Imaging of Sprays. *Prog. Energy Combust. Sci.* **1991**, 17, 211.
- Christian, S. D.; Stevens, T. L. Association of Trifluoroacetic Acid in Vapor and in Organic Solvents. *J. Phys. Chem.* **1972**, 76, 2039.
- Clarke, M. J.; Harrison, K. L.; Johnston, K. P.; Howdle, S. M. Water in Supercritical Carbon Dioxide Microemulsions: Spectroscopic Investigation of a New Environment for Aqueous Inorganic Chemistry. *J. Am. Chem. Soc.* **1997**, 119, 6399.
- Connon, C. S.; Barocas, V. H.; Randolph, T. W. Application of Jet Breakup Models to Systems with Low Liquid-Gas Density Ratios and High Miscibilities. Los Alamos Days, Boulder, CO, 1998.
- Coolidge, A. The vapor density and some other properties of formic acid. *J. Am. Chem. Soc.* **1928**, 50, 2166.
- Crooks, J. E.; Donnellan, J. P. Kinetics and Mechanism of the Reaction between Carbon Dioxide and Amines in Aqueous Solution. *J. Chem. Soc. Perkin Trans. II* **1989**, 331.
- da Rocha, S. R. P.; Dickson, J. L.; Cho, D.; Rossky, P. J.; Johnston, K. P. Surfactants for Stabilization of Water and CO<sub>2</sub> Emulsions: Trisiloxanes. *Langmuir* **2003**, 19, 3114.
- Danckwerts, P. V. The Reaction of Carbon Dioxide with Ethanolamines *Chem. Eng. Sci.* **1979**, 34, 443.

- Dardin, A.; DeSimone, J. M.; Samulski, E. T. Fluorocarbons Dissolved in Supercritical Carbon Dioxide: NMR Evidence for Specific Solute-Solvent Interactions. *J. Phys. Chem. B* **1998**, 102, 1775.
- DeSimone, J. M.; Guan, Z.; Elsbernd, C. S. Synthesis of Fluoropolymers in Supercritical Carbon Dioxide. *Science* **1992**, 257, 945.
- Dickson, J. L.; Binks, B. P.; Johnston, K. P. Stabilization of Carbon Dioxide-in-Water Emulsions with Silica Nanoparticles. *Langmuir* **2004**, 20, 7976.
- Dickson, J. L.; Smith, P. G. Jr.; Dhanuka, V. V.; Srinivasan, V.; Stone, M. T.; Rossky, P. J.; Behles, J. A.; Keiper, J. P.; Xu, B.; Johnson, C.; DeSimone, J. M.; Johnston, K. P. Interfacial Properties of Fluorocarbon and Hydrocarbon Phosphate Surfactants at the Water-CO<sub>2</sub> Interface. *Ind. Eng. Chem. Res.* **2005**, 44, 1370.
- Dimitrov, S.; Kemenska, V.; Walker, J. D.; Windle, W.; Purdy, R.; Lewis, M.; Mekenyan, O. Predicting the Biodegradation Products of Perfluorinated Chemicals using CATABOL. *SAR QSAR Environ. Res.* **2004**, 15, 69.
- Dixon, D. J.; Johnston, K. P.; Bodmeier, R. A. Polymeric Materials Formed by Precipitation with a Compressed Fluid Antisolvent. *AIChE J.* 1993, 39(1), 127.
- Dong, X.; Potter, D.; Erkey, C. Synthesis of CuS Nanoparticles in Water-in-Carbon Dioxide Microemulsions. *Ind. Eng. Chem. Res.* **2002**, 41(18), 4489.
- Eastoe, J.; Dupont, A.; Steytler, D. C.; Thorpe, M.; Gurgel, A.; Heenan, R. K. Micellization of Economically Viable Surfactants in CO<sub>2</sub>. *J. Coll. Inter. Sci.* **2003**, 258,367.
- Eastoe, J.; Paul, A.; Nave, S.; Steytler, D. C.; Robinson, B. H.; Rumsey, E.; Thorpe, M.; Heenan, R. K. Micellization of Hydrocarbon Surfactants in Supercritical Carbon Dioxide. *JACS* **2001**, 123, 988.
- Eckert, C. A.; Knutson, B. L.; Debenedetti, P. G. Supercritical fluids as solvents for chemical and materials processing. *Nature* **1996**, 383(6598), 313.
- Economou, I. G.; Donohue, M. D. Chemical, quasi-chemical and perturbation theories for associating fluids. *AIChE J.* **1991**, 37, 1875.
- Ellington, J. B.; Park, K. M.; Brennecke, J. F. Effect of Local Composition Enhancements on the Esterification of Phtalic Anhydride with Methanol in Supercritical Carbon Dioxide. *Ind. Eng. Chem. Res.* **1994**, 33, 965.
- Elvassore, N.; Cozzi, F.; Bertucco, A. Mass Transport Modeling in a Gas Antisolvent Process. *Ind. Eng. Chem. Res.* **2004**, 43, 4935.
- Ershov, B. G.; Henglein, A. Reduction of Ag<sup>+</sup> on Polyacrylate Chains in Aqueous Solution. *J. Phys. Chem. B* **1998**, 102, 10663.
- Fan, X.; McLeod, M. C.; Enick, R. M.; Beckman, E. J.; Roberts, C. B. Preparation of Silver Nanoparticles via Reduction of a Highly CO<sub>2</sub>-Soluble Hydrocarbon-Based Metal Precursor. *Ind. Eng. Chem. Res.* (submitted)
- Fan, X.; Potluri, V. K.; McLeod, M. C.; Wang, Y.; Liu, J.; Enick, R. M.; Hamilton, A. D.; Roberts, C. B.; Johnson, J. K.; Beckman, E. J. Oxygenated Hydrocarbon Ionic Surfactants Exhibit CO<sub>2</sub> Solubility. *JACS* **2005**, 127(33), 11754.
- Fang, Z.; Kozinski, J. A. Phase Changes of Benzo(a)Pyrene in Supercritical Water Combustion. *Combustion and Flame* **2001**, 124, 255.
- Fink, R.; Hancu, D.; Valentine, R.; Beckman, E. J. Toward the Development of "CO<sub>2</sub>-philic" Hydrocarbons. 1. Use of Side-Chain Functionalization to Lower the

- Miscibility Pressure of Polydimethylsiloxanes in CO<sub>2</sub>. *J. Phys. Chem. B* **1999**, *103*, 6444.
- Foresman, J. B.; Frisch, Æ. *Exploring Chemistry with Electronic Structure Methods: 2nd Edition*; Gaussian, Inc.: PA, 1996.
- Frisch, Æ.; Frisch, M. J. *Gaussian98 User's Reference, Second Edition*; Gaussian Inc.: PA, 1999.
- Frisch, M. J.; Trucks, G. W.; Schlegel, H. B.; Scuseria, G. E.; Robb, M. A.; Cheeseman, J. R.; Zakrzewski, V. G.; Montgomery, J. A. J.; Stratmann, R. E.; Burant, J. C.; Dapprich, S.; Millam, J. M.; Daniels, A. D.; Kudin, K. N.; Strain, M. C.; Farkas, O.; Tomasi, J.; Barone, V.; Cossi, M.; Cammi, R.; Mennucci, B.; Pomelli, C.; Adamo, C.; Clifford, S.; Ochterski, J.; Petersson, G. A.; Ayala, P. Y.; Cui, Q.; Morokuma, K.; Salvador, P.; Dannenberg, J. J.; Malick, D. K.; Rabuck, A. D.; Raghavachari, K.; Foresman, J. B.; Cioslowski, J.; Ortiz, J. V.; Baboul, A. G.; Stefanov, B. B.; Liu, G.; Liashenko, A.; Piskorz, P.; Komaromi, I.; Gomperts, R.; Martin, R. L.; Fox, D. J.; Keith, T.; Al-Laham, M. A.; Peng, C. Y.; Nanayakkara, A.; Challacombe, M.; Gill, P. M. W.; Johnson, B.; Chen, W.; Wong, M. W.; Andres, J. L.; Gonzalez, C.; Head-Gordon, M.; Replogle, E. S.; Pople, J. A. *Gaussian, Inc., Pittsburgh PA* **2001**.
- Fujii, A.; Ebata, T.; Mikami, N. Direct Observation of Weak Hydrogen Bonds in Microsolvated Phenol: Infrared Spectroscopy of OH Stretching Vibrations of Phenol-CO and -CO<sub>2</sub> in S0 and D0. *J. Phys. Chem. A* **2002**, *106*, 10124.
- Fujii, Y.; Yamada, H.; Mizuta, M. Self-association of acetic acid in some organic solvents. *J. Phys. Chem.* **1988**, *92*, 6768.
- Fulton, J. L.; Yee, G. G.; Smith, R. D. Hydrogen bonding of methyl alcohol-d in supercritical carbon dioxide and supercritical ethane solutions. *J. Am. Chem. Soc.* **1991**, *113*, 8327.
- Griffith, A. T.; Park, Y.; Roberts, C. B. Separation and Recovery of Nylon From Carpet Waste Using a Supercritical Fluid Antisolvent Technique. *Polymer-Plastics Tech. Eng. J.* **1999**, *38*(3), 411.
- Gupta, R. B.; Brinkley, R. L. Hydrogen-bond cooperativity in 1-alkanol + n-alkane binary mixtures. *AIChE J.* **1998**, *44*, 207.
- Gupta, R. B.; Combes, J. R.; Johnston, K. P. Solvent effect on hydrogen bonding in supercritical fluids. *J. Phys. Chem.* **1993**, *97*, 707.
- Gupta, R. B.; Panayiotou, C. G.; Sanchez, I. C.; Johnston, K. P. Theory of hydrogen bonding in supercritical fluids. *AIChE J.* **1992**, *38*, 1243.
- Hampe, E. M.; Rudkevich, D. M. Reversible Covalent Chemistry of CO<sub>2</sub>. *Chem. Commun.* **2002**, *14*, 1450.
- Heidemann, R. A.; Prausnitz, J. M. A van der Waals-type equation of state for fluids with associating molecules. *Proc. Natl. Acad. Sci. U.S.A.* **1976**, *73*, 1773.
- Hizagy, W. S.; Taha, A. A. The Extent of Self-Association of Trifluoroacetic Acid in Different Nonpolar Solvents. *J. Phys. Chem.* **1970**, *74*, 1982.
- Hoefling, T. A.; Beitle, R. R.; Enick, R. M.; Beckman, E. Design and Synthesis of Highly CO<sub>2</sub>-Soluble Surfactants and Chelating Agents. *J. Fluid Phase Equilibria* **1993**, *83*, 203.

- Hoefling, T. A.; Enick, R. M.; Beckman, E. J. Microemulsions in Near-Critical and Supercritical CO<sub>2</sub>. *J. Phys. Chem.* **1991**, 95, 7127.
- Hoffmann, M. M.; Conradi, M. S. Nuclear Magnetic Resonance Probe for Supercritical Water and Aqueous Solutions. *Rev. Sci. Instrum.* **1997**, 68(1), 159.
- Hoffmann, M. M.; Conradi, M. S. Are There Hydrogen Bonds in Supercritical Water? *J. Am. Chem. Soc.* **1997**, 119, 3811.
- Hoffmann, M. M.; Conradi, M. S. Are There Hydrogen Bonds in Supercritical Methanol and Ethanol? *J. Phys. Chem. B* **1998**, 102, 263.
- Holmes, J. D.; Bhargava, P. A.; Korgel, B. A.; Johnston, K. P. Synthesis of Cadmium Sulfide Q Particles in Water-in-CO<sub>2</sub> Microemulsions. *Langmuir* **1999**, 15, 6613.
- Horvath, I. T.; Ponce, E. C. New Valve Design for High-Pressure Sapphire Tubes for NMR Measurements. *Rev. Sci. Instrum.* **1991**, 62(4), 1104.
- Hou, Z.; Han, B.; Zhang, X.; Zhang, H.; Liu, Z. Pressure Tuning of Reaction Equilibrium of Esterification of Acetic Acid with Ethanol in Compressed CO<sub>2</sub>. *J. Phys. Chem. B* **2001**, 105, 4510.
- Huang, S. H.; Radosz, M. Equation of state for small, large, polydisperse, and associating molecules. *Ind. Eng. Chem. Res.* **1990**, 29, 2284.
- Huang, S. H.; Radosz, M. Equation of state for small, large, polydisperse, and associating molecules: extension to fluid mixtures. *Ind. Eng. Chem. Res.* **1993**, 32, 762.
- Huang, X.; Roberts, C. B. Selective Fischer-Tropsch Synthesis Over an AL<sub>2</sub>O<sub>3</sub> Supported Cobalt Catalyst in Supercritical Hexane. *Fuel Process. Techn.* **2003**, 83, 81.
- Hughmark, G. A. Liquid-Liquid Spray Column Drop Size, Holdup and Continuous Phase Mass Transfer. *Ind. Eng. Chem. Res.* **1967**, 6, 409.
- Huyskens, P. L. Mobile and static molecular disorder in liquids. *J. Mol. Struct.* **1992**, 274, 223.
- Hyatt, J. A. Liquid and Supercritical Carbon Dioxide as Organic Solvents. *J. Org. Chem.* **1984**, 49, 5097.
- Jameson, C. J. Gas-Phase NMR Spectroscopy. *Chem. Rev.* **1991**, 91, 1375.
- Jentschura, U.; Lippert, E. NMR spectroscopic investigations on self-association of carboxylic acids in inert solvents. II. Thermodynamic parameters of propionic acid association. *Ber. Bunsenges. Phys. Chem.* **1971**, 75, 782.
- Ji, M.; Chen, X.; Wai, C. M.; Fulton, J. L. Synthesizing and Dispersing Silver Nanoparticles in a Water-in-Supercritical Carbon Dioxide Microemulsion. *JACS* **1999**, 121, 2631.
- Johnston, K. P.; Cho, D.; DaRocha, S. R. P.; Psathas, P. A.; Ryoo, W.; Webber, S. E.; Eastoe, J.; Dupont, A.; Steytler, D. C. Water in Carbon Dioxide Macroemulsions and Miniemulsions with a Hydrocarbon Surfactant. *Langmuir* **2001**, 17, 7191.
- Johnston, K. P.; Harrison, K. L.; Clarke, M. J.; Howdle, S. M.; Heitz, M. P.; Bright, F. V.; Carlier, C.; Randolph, T. W. Water-in-Carbon Dioxide Microemulsions: An Environment for Hydrophiles Including Proteins. *Science* **1996**, 271, 624.
- Jonas, J.; Ballard, L.; Nash, D. High-Resolution, High-Pressure NMR Studies of Proteins. *Biophys. J.* **1998**, 75(1), 445.
- Jonas, J.; Koziol, P.; Peng, X.; Reiner, C.; Campbell, D. M. High-Resolution NMR Spectroscopy at High Pressures. *J. Magn. Reson.* **1993**, 102, 299.

- Kanakubo, M.; Umecky, T.; Liew, C. C.; Aizawa, T.; Hatakeda, K.; Ikushima, Y. High-Pressure NMR Studies on Solvation Structure in Supercritical Carbon Dioxide. *Fluid Phase Equilibria* **2002**, 194, 859.
- Kazarian, S. G.; Gupta, R. B.; Clarke, M. J.; Johnston, K. P.; Poliakov, M. How is hydrogen-bonding influenced by solvent density? The spectroscopic study and modeling of the interaction between a proton donor and acceptor from the gas phase to supercritical fluid states. *J. Am. Chem. Soc.* **1993**, 115, 11099.
- Kazarian, S. G.; Vincent, M. F.; Bright, F. V.; Liotta, C. L.; Eckert, C. A. Specific Intermolecular Interaction of Carbon Dioxide with Polymers. *J. Am. Chem. Soc.* **1996**, 118, 1729.
- Kemmere, M.; Kuijpers, M.; Keurentjes, J. Ultrasound-Induced Polymerization of Methyl Methacrylate in Liquid Carbon Dioxide: A Clean and Safe Route to Produce Polymers with Controlled Molecular Weight. *Macromolecular Symposia* **2004**, 206, 321.
- Kerst, A. W.; Judat, B.; Schlunder, E. U. Flow Regimes of Free Jets and Falling Films at High Ambient Pressure. *Chemical Eng. Sci.* **2000**, 55, 4189.
- Kirszenbaum, M.; Corset, J.; Josien, M. L. Trifluoroacetic Acid. The Nature of Association in Diluted Solutions in Inert and Slightly Basic Solvents. *J. Phys. Chem.* **1971**, 75(9), 1327.
- Kitchens, C. L.; Roberts, C. B. Copper Nanoparticle Synthesis in Compressed Liquid and Supercritical Fluid Reverse Micelle Systems. *Ind. Eng. Chem. Res.* **2004**, 43(19), 6070.
- Kojima, Y.; Koda, S.; Nomura, H. Effect of Ultrasonic Frequency on Polymerization of Styrene under Sonication. *Ultrasonics Sonochemistry* **2001**, 8(2), 75.
- Kompella, U.; Koushik, K. Preparation of drug delivery systems using supercritical fluid technology. *Crit. Rev. Thera. Drug Carr. Sys.* **2001**, 18(2), 173.
- Laitinen, A.; Jantti, M. Solubility of 6-Caprolactam in Supercritical Carbon Dioxide. *J. Chem. Eng. Data* **1996**, 41, 1418.
- Lengsfeld, C. S.; Delplanque, J. P.; Barocas, V. H.; Randolph, T. W. Mechanism Governing Microparticle Morphology during Precipitation by a Compressed Antisolvent: Atomization vs Nucleation and Growth. *J. Phys. Chem. B* **2000**, 104, 2725.
- Lim, Y.; Nugara, N. E.; King, A. D. NMR Chemical Shifts of Xenon-129 in Liquid Carbon Dioxide, Nitrous Oxide, Ethane, and Propane at 23 °C. *J. Phys. Chem.* **1993**, 97, 8816.
- Liu, H. *Science and Engineering of Droplets*, Noyes Publications, New Jersey, 2000.
- Liu, J.; Han, B.; Li, G.; Zhang, X.; He, J.; Liu, Z. Investigation of Nonionic Surfactant Dynol-604 Based Reverse Microemulsions Formed in Supercritical Carbon Dioxide. *Langmuir* **2001**, 17, 8040.
- Liu, J.; Raveendran, P.; Shervani, Z.; Ikushima, Y.; Hakuta, Y. Synthesis of Ag and AgI Quantum Dots in AOT-Stabilized Water-in-CO<sub>2</sub> Microemulsions. *Chem. Europ. Journ.* **2005**, 11, 1854.
- Lora, M.; Bertucco, A.; Kikic, I. Simulation of the Semicontinuous Supercritical Antisolvent Recrystallization Process. *Ind. Eng. Chem. Res.* **2000**, 39, 1487.

- Lora, M.; Rindfleisch, F.; McHugh, M. A. Influence of the Alkyl Tail on the Solubility of Poly(alkyl acrylates) in Ethylene and CO<sub>2</sub> at High Pressures: Experiments and Modeling. *J. Appl. Polym. Sci.* **1999**, 73, 1979.
- Lousenberg, R. D.; Shoichet, M. S. Synthesis of Linear Poly(tetrafluoroethylene-*co*-vinyl acetate) in Carbon Dioxide. *Macromolecules* **2000**, 33, 1682.
- Lu, J.; Han, B.; Yan, H. Solvent Effect on Monomer-Dimer Equilibrium in Supercritical Fluid: Spectroscopic and Thermodynamic Studies. *Phys. Chem. Chem. Phys.* **1998**, 1, 449.
- Luo, J. J.; Shen, Y.; Zhu, C.; Dave, R. N.; Pfeffer, R.; Debenedetti, P. G. Khusid, B. In-Situ Optical Studies on Drop/Particle Formation Under Supercritical Conditions. AICHE Annual Meeting 1998.
- Marioth, E.; Koenig, B.; Krause, H.; Loebbecke, S. Fast Particle Size and Droplet Size Measurements in Supercritical CO<sub>2</sub>. *Ind. Eng. Chem. Res.* **2000**, 39, 4853.
- Martin, T.; Bandi, N.; Shulz, R.; Roberts, C. B.; Kompella, U. Preparation of Budesonide and Budesonide-PLA Microparticles Using Supercritical Fluid Processing Technology. *AAPS PharmSciTech* **2002**, 3(3).
- Martin, T. M. *Phase Behavior and Particle Formation of Polymers in Supercritical Fluid Solvents*, Ph. D. Dissertation, Auburn University, Auburn 2000.
- Mawson, S.; Kanakia, S.; Johnston, K. P. Coaxial Nozzle for Control of Particle Morphology in Precipitation with a Compressed Fluid Antisolvent. *J. Appl. Polym. Sci.* **1997**, 64(11), 2105.
- Mayer, W.; Tamura, H. Propellant Injection in a Liquid Oxygen/Gaseous Hydrogen Rocket Engine. *Journal of Propulsion and Power* **1996**, 12(6), 1137.
- McHugh, M. A.; Krukonis, V. J. *Supercritical Fluid Extraction: Principles and Practice*; Butterworths: Boston, 1994.
- McLeod, M. C.; Gale, W. F.; Roberts, C. B.; Roberts, C. B. Metallic Nanoparticle Production Utilizing a Supercritical Carbon Dioxide Flow Process. *Langmuir* **2004**, 20(17), 7078.
- McLeod, M. C.; Kitchens, C. L.; Roberts, C. B. CO<sub>2</sub>-Expanded Liquid Deposition of Ligand-Stabilized Nanoparticles as Uniform, Wide-Area Nanoparticle Films. *Langmuir* **2005**, 21(6), 2414.
- McLeod, M. C., McHenry, R. S., Beckman, E. J., and Roberts, C. B. Synthesis and Stabilization of Metallic Nanoparticles and Pre-metallic Intermediates in PFPE/CO<sub>2</sub> Reverse Micelle Systems. *Phys. Chem. B* **2003**, 107(12), 2693.
- Melikova, S. M.; Rutkowski, K. S.; Rodziewicz, P.; Koll, A. Unusual Spectroscopic Properties of CF<sub>3</sub>H Dissolved in Liquified Ar, N<sub>2</sub>, CO, and CO<sub>2</sub>. *Chem. Phys. Lett.* **2002**, 352, 301.
- Meredith, J. C.; Johnston, K. P.; Seminario, J. M.; Kazarian, S. G.; Eckert, C. A. Quantitative Equilibrium Constants between CO<sub>2</sub> and Lewis Bases from FTIR Spectroscopy. *J. Phys. Chem.* **1996**, 100, 10837.
- Mikhailova, O. K.; Solomentseva, T. V.; Markuzin, N. P. Equilibrium of acetic and propionic acids with associated vapor. *Deposited Doc.* **1981**, 9.
- Miyamoto, S.; Nakamura, S.; Iwai, Y.; Arai, Y. Measurement of Vapor-Phase Compressibility Factors of Monocarboxylic Acids Using a Flow-Type Apparatus and Their Association Constants. *J. Chem. Eng. Data* **1999**, 44, 48.

- Mukhopadhyay, M.; Dalvi, S. V. Mass and Heat Transfer Analysis of SAS: Effects of Thermodynamic States and Flow Rates on Droplet Size. *J. Supercritical Fluids* **2004**, *30*, 333.
- Mukhopadhyay, M.; Dalvi, S. V. Partial Molar Volume Fraction of Solvent in Binary (CO<sub>2</sub>-Solvent) Solution for Solid Solubility Predictions. *J. Supercritical Fluids* **2004**, *29*, 221.
- Murty, T. S. S. R. Perfluorinated aliphatic carboxylic acids. Nature of association in dilute solutions in nonpolar solvents. *J. Phys. Chem.* **1971**, *75*, 1330.
- Murty, T. S. S. R.; Pitzer, K. S. Trifluoroacetic acid. Nature of association in dilute solutions in nonpolar solvents. *J. Phys. Chem.* **1969**, *73*, 1426.
- Nave, S.; Eastoe, J.; Penfold, J. What is So Special About Aerosol-OT? 1. Aqueous Systems. *Langmuir* **2000**, *16*(23), 8733.
- Nelson, M.; Borkman, R. Ab initio calculations on CO<sub>2</sub> binding to carbonyl groups. *J. Phys. Chem. A* **1998**, *102*, 7860.
- Notz, P. K.; Chen, A. U.; Basaran, O. A. Satellite Drops: Unexpected Dynamics and Change of Scaling During Pinch-Off. *Physics of Fluids* **2001**, *13*(3), 549.
- Ohde, H.; Ye, X.; Wai, C. M.; Rodriguez, J. M. Synthesizing Silver Halide Nanoparticles in Supercritical Carbon Dioxide Utilizing a Water-in-CO<sub>2</sub> Microemulsion. *Chem. Comm.* **2000**, *23*, 2353.
- O'Neill, M. L.; Cao, Q.; Fang, M.; Johnston, K. P.; Wilkinson, S. P.; Smith, C. D.; Kerschner, J. L.; Jureller, S. H. Solubility of Homopolymers and Copolymers in Carbon Dioxide. *Ind. Eng. Chem. Res.* **1998**, *37*(8), 3067.
- O'Shea, K. E.; Kirmse, K. M.; Fox, M. A.; Johnston, K. P. Polar and Hydrogen-Bonding Interactions in Supercritical Fluids. Effects on the Tautomeric Equilibrium of 4-(Phenylazo)-1-naphthol. *J. Phys. Chem.* **1991**, *95*, 7863.
- Owens, J. L.; Anseth, K. S.; Randolph, T. W. Compressed Antisolvent Precipitation and Photopolymerization To Form Highly Cross-Linked Polymer Particles. *Macromolecules* **2002**, *35*, 4289.
- Owens, J. L.; Anseth, K. S.; Randolph, T. W. Mechanism of Microparticle Formation in the Compressed Antisolvent Precipitation and Photopolymerization (CAPP) Process. *Langmuir* **2003**, *19*, 3926.
- Panayiotou, C.; Sanchez, I. C. Hydrogen bonding in fluids: an equation-of-state approach. *J. Phys. Chem.* **1991**, *95*, 10090.
- Park, Y.; Curtis, C. W.; Roberts, C. B. Formation of nylon particles and fibers using precipitation with a compressed antisolvent. *Ind. Eng. Chem. Res.* **2002**, *41*(6), 1504.
- Park, Y.; Gupta, R. B.; Curtis, C. C.; Roberts, C. B. Solvent Effects on the Self-Association of Formic Acid in Carbon Dioxide and Ethane. *J. Phys. Chem. B* **2002**, *106*, 9696.
- Petit, C.; Lixon, P.; Pileni, M. P. In Situ Synthesis of Silver Nanocluster in AOT Reverse Micelles. *J. Phys. Chem.* **1993**, *97*(49), 12974.
- Pfund, D. M.; Zemanian, T. S.; Linehan, J. C.; Fulton, J. L.; Yonker, C. R. Fluid Structure in Supercritical Xenon by Nuclear Magnetic Resonance Spectroscopy and Small Angle X-ray Scattering. *J. Phys. Chem.* **1994**, *98*, 11846.

- Phillips, J. H.; Robey, R. J. Solvent Strength and Selectivity Properties of Supercritical Carbon Dioxide Relative to Liquid Hexane. *J. Chromatogr.* **1989**, 465, 177.
- Pileni, M. P.; Zemb, T.; Petit, C. Solubilization by Reverse Micelles: Solute Localization and Structure Perturbation. *Chem. Phys. Lett.* **1985**, 118(4), 414.
- Potluri, V. K.; Xu, J.; Enick, R. M.; Beckman, E. J.; Hamilton, A. D. Peracetylated Sugar Derivatives Show High Solubility in Liquid and Supercritical Carbon Dioxide. *Org. Lett.* **2002**, 4(14), 2333.
- Ramon, J. M. H.; Rios, M. A. A new intermolecular polarizable potential for cis-formic acid. Introduction of many-body interactions in condensed phases. *Chem. Phys.* **1999**, 250, 155.
- Randolph, T. W.; Randolph, A. D.; Mebes, M.; Yeung, S. Sub-Micrometer-Sized Biodegradable Particles of Poly(L-Lactic Acid) via the Gas Antisolvent Spray Precipitation Process. *Biotechnol. Prog.* **1993**, 9, 429.
- Raveendran, P.; Wallen, S. Cooperative C-H...O hydrogen bonding in CO<sub>2</sub>-Lewis base complexes: implications for solvation in supercritical CO<sub>2</sub>. *J. Am. Chem. Soc.* **2002**, 124, 12590.
- Raveendran, P.; Wallen, S. L. Exploring CO<sub>2</sub>-Philicity: Effects of Stepwise Fluorination. *J. Phys. Chem. B* **2003**, 107, 1473.
- Raveendran, P.; Wallen, S. L. Dissolving Carbohydrates in CO<sub>2</sub>: Renewable Materials as CO<sub>2</sub>-philes. *ACS Symp. Ser.* **2003**, 860, 270.
- Reilly, J. T.; Bokis, C. P.; Donohue, M. D. An experimental investigation of Lewis acid-base interactions of liquid carbon dioxide using Fourier transform infrared (FT-IR) spectroscopy. *Int. J. Thermophys.* **1995**, 16, 599.
- Reverchon, E.; Della Porta, G. Supercritical Fluids-Assisted Micronization Techniques. Low-Impact Routes for Particle Production. *Pure Appl. Chem.* **2001**, 73(8), 1293.
- Riley, D.; McGhee, W. D.; Waldman, T. Generation of Urethanes and Isocyanates from Amines and Carbon Dioxide. *ACS Symp. Ser.* **1994**, 577, 122.
- Rindfleisch, F.; DiNoia, T.; McHugh, M. J. Solubility of Polymers and Copolymers in Supercritical CO<sub>2</sub>. *J. Phys. Chem.* **1996**, 100, 15581.
- Roe, D. C. Sapphire NMR Tube for High-Resolution Studies at Elevated Pressure. *J. Magn. Reson.* **1985**, 63, 388.
- Ryoo, W.; Webber, S. E.; Johnston, K. P. Water-in-Carbon Dioxide Microemulsions with Methylated Branched Hydrocarbon Surfactants. *Ind. Eng. Chem. Res.* **2003**, 42(25), 6348.
- Said, S.; Rajewski, R. A.; Valentino, S.; Subramaniam, B. Methods and Apparatus for Particle Precipitation and Coating Using Near-Critical and Supercritical Antisolvents. USA pat. # WO9731691, 1997.
- Sarbu, T.; Styranec, T. J.; Beckman, E. J. Design and Synthesis of Low Cost, Sustainable CO<sub>2</sub>-philes. *Ind. Eng. Chem. Res.* **2000**, 39, 4678.
- Sarbu, T.; Styranec, T. J.; Beckman, E. J. Non-fluorous Polymers with Very High Solubility in Supercritical CO<sub>2</sub> Down to Low Pressures. *Nature* **2000**, 405, 165.
- Saunders, A. E.; Shah, P. S.; Park, E. J.; Lim, K. T.; Johnston, K. P.; Korgel, B. A. Solvent Density-Dependent Steric Stabilization of Perfluoropolyether-Coated Nanocrystals in Supercritical Carbon Dioxide. *J. Phys. Chem. B* **2004**, 108(41), 15969.

- Schueuermann, G.; Cossi, M.; Barone, V.; Tomasi, J. Prediction of the pKa of Carboxylic Acids Using the ab Initio Continuum-Solvation Model PCM-UAHF. *J. Phys. Chem. A* **1998**, *102*, 6706.
- Schultz, C. P.; Eysel, H. H.; Mantsch, H. H.; Jackson, M. Carbon Dioxide in Tissues, Cells, and Biological Fluids Detected by FTIR Spectroscopy. *J. Phys. Chem.* **1996**, *100*, 6845.
- Shah, P. S.; Hanrath, T.; Johnston, K. P.; Korgel, B. A. Nanocrystal and Nanowire Synthesis and Dispersibility in Supercritical Fluids. *J. Phys. Chem. B* **2004**, *108*(28), 9474.
- Shah, P. S.; Holmes, J. D.; Doty, R. C.; Johnston, K. P.; Korgel, B. A. Steric Stabilization of Nanocrystals in Supercritical CO<sub>2</sub> Using Fluorinated Ligands. *JACS* **2000**, *122*(17), 4245.
- Shah, P. S.; Holmes, J. D.; Johnston, K. P.; Korgel, B. A. Size-Selective Dispersion of Dodecanethiol-Coated Nanocrystals in Liquid and Supercritical Ethane by Density Tuning. *J. Phys. Chem. B* **2002**, *106*(10), 2545.
- Shah, P. S.; Husain, S.; Johnston, K. P.; Korgel, B. A. Nanocrystal Arrested Precipitation in Supercritical Carbon Dioxide. *J. Phys. Chem. B* **2001**, *105*(39), 9433.
- Shah, P. S.; Husain, S.; Johnston, K. P.; Korgel, B. A. Role of Steric Stabilization on the Arrested Growth of Silver Nanocrystals in Supercritical Carbon Dioxide. *J. Phys. Chem. B* **2002**, *106*(47), 12178.
- Shah, P. S.; Novick, B. J.; Hwang, H. S.; Lim, K. T.; Carbonell, R. G.; Johnston, K. P.; Korgel, B. A. Kinetics of Nonequilibrium Nanocrystal Monolayer Formation: Deposition from Liquid Carbon Dioxide. *Nano Lett.* **2003**, *3*(12), 1671.
- Shekunov, B. Y.; Baldyga, J.; York, P. Particle Formation by Mixing with Supercritical Antisolvent at High Reynolds Numbers. *Chem. Eng. Sci.* **2001**, *56*, 2421.
- Shekunov, B. Y.; Hanna, M.; York, P. Crystallization Process in Turbulent Supercritical Flows. *Journal of Crystal Growth* **1999**, *198*(199), 1345.
- Shen, Z. McHugh, M. A.; Xu, J. Belardi, J.; Kilic, S.; Mesiano, A.; Bane, S.; Karnikas, C.; Beckman, E.; Enick, R. CO<sub>2</sub>-solubility of oligomers and polymers that contain the carbonyl group. *Polymer* **2003**, *44*(5), 1491.
- Sigman, M. E.; Lindley, S. M.; Leffler, J. E. Supercritical Carbon Dioxide: Behavior of p\* and b Solvatochromic Indicators in Media of Different Densities. *J. Am. Chem. Soc.* **1985**, *107*, 1471.
- Span, R.; Wagner, W. A New Equation of State for Carbon Dioxide Covering the Fluid Region from the Triple-Point Temperature to 1100 K at Pressures up to 800 MPa. *J. Phys. Chem. Ref. Data* **1996**, *25*(6), 1509.
- Stein, M.; Sauer, Formic acid tetramers: structure isomers in the gas phase. *J. Chem. Phys. Lett.* **1997**, *267*, 111.
- Stephens, A. P. *Visualization of Particle Formation Processes in Supercritical Fluids*, Ph. D. Dissertation, Auburn University, Auburn 2003.
- Stone, M. T.; DaRocha, S. R. P.; Rossky, P. J.; Johnston, K. P. Molecular Differences between Hydrocarbon and Fluorocarbon Surfactants at the CO<sub>2</sub>/Water Interface. *J. Phys. Chem. B* **2003**, *107*(37), 10185.

- Stone, M. T.; Smith, P. G. Jr.; DaRocha, S. R. P.; Rossky, P. J.; Johnston, K. P. Low Interfacial Free Volume of Stubby Surfactants Stabilizes Water-in-Carbon Dioxide Microemulsions. *J. Phys. Chem. B* **2004**, 108(6), 1962.
- Sun, Y. *Supercritical Fluid Technology in Materials Science and Engineering Syntheses, Properties, and Applications*, Culinary and Hospitality Industry Publications Services, Weimar, Texas, 2002.
- Sychev, V. V.; Selover, T. B.; Slark, G. E. *Thermodynamic Properties of Ethane*; Hemisphere Publishing Corp.: New York, 1987.
- Tai, C. C.; Pitts, J.; Main, A. D.; Linehan, J. C.; Munshi, P.; Jessop, P. G. In-Situ Formation of Ruthenium Catalysts for the Homogeneous Hydrogenation of Carbon Dioxide. *Inorg. Chem.* **2002**, 41, 1606.
- Teramoto, M.; Huang, Q.; Watari, T.; Tokunaga, Y.; Nakatani, R.; Maeda, T.; Matsuyama, H. Facilitated Transport of CO<sub>2</sub> Through Supported Liquid Membranes of Various Amine Solutions-Effects of Rate and Equilibrium of Reaction between CO<sub>2</sub> and Amine. *J. Chem. Eng. Jap.* **1997**, 30(222), 328.
- Thote, A. J.; Gupta, R. B. Formation of Nanoparticles of a Hydrophilic Drug Using Supercritical Carbon Dioxide and Microencapsulation for Sustained Release. *Nanomedicine* **2005**, 1(1), 85.
- Tison, J. K.; Hunt, E. R. Self-Diffusion, Spin-Lattice Relaxation, and Density of SF<sub>6</sub> near the Critical Point. *J. Chem. Phys.* **1971**, 54(4), 1526.
- Van Dyke, M. *An Album of Fluid Motion*, The Parabolic Press, Stanford, 1982.
- Wallen, S. L.; Palmer, B. J.; Garrett, B. C.; Yonker, C. R. Density and Temperature Effects on the Hydrogen Bond Structure of Liquid Methanol. *J. Phys. Chem.* **1996**, 100, 3959.
- Wallen, S. L.; Schoenbachler, L. K.; Dawson, E. D.; Blatchford, M. A. A Polymer NMR Cell for the Study of High-Pressure and Supercritical Fluid Solutions. *Anal. Chem.* **2000**, 72, 4230.
- Werling, J. O.; Debenedetti, P. G. Numerical Modeling of Mass Transfer in the Supercritical Antisolvent Process. *J. Supercritical Fluids* **1999**, 16, 167.
- Werling, J. O.; Debenedetti, P. G. Numerical Modeling of Mass Transfer in the Supercritical Antisolvent Process: Miscible Conditions. *J. Supercritical Fluids* **2000**, 18, 11.
- Wilkes, E. D.; Phillips, S. D.; Basaran, O. A. Computational and Experimental Analysis of Dynamics of Drop Formation. *Physics of Fluids* **1999**, 11(12), 3577.
- Winkler, A.; Hess, P. A Study of the Energetics and Dynamics of Hydrogen Bond Formation in Aliphatic Carboxylic Acid Vapors by Resonant Photoacoustic Spectroscopy. *J. Am. Chem. Soc.* **1994**, 116(20), 9233.
- Wolbach, J. P.; Sandler, S. I. Thermodynamics of hydrogen-bonding from Molecular Orbital Theory: I. Water. *AIChE Journal* **1997**, 43, 1589.
- Wong, M. W.; Frisch, M. J.; Wiberg, K. B. Solvent Effects. 1. The Mediation of Electrostatic Effects by Solvents. *J. Am. Chem. Soc.* **1991**, 113, 4776.
- Xie, J. Kinetics and Simulation of Solid-State Polymerization for Nylon 6. *Ind. Eng. Chem. Res.* **2001**, 40, 3152.

- Xiong, Y.; Kiran, E. Prediction of high-pressure phase behaviour in polyethylene/n-pentane/carbon dioxide ternary system with the Sanchez-Lacombe model. *Polymer* **1994**, 35(20), 4408.
- Yamada, H. Pressure-Resisting Glass Cell for High Pressure, High Resolution NMR Measurement. *Rev. Sci. Instrum.* **1974**, 45(5), 640.
- Yamada, H.; Nakatsuka, M.; Yamochi, H.; Sawamura, M.; Sera, A. Spinning Glass Cell for High-Pressure High-Resolution NMR Measurements. *Rev. Sci. Instrum.* **1991**, 62(3), 700.
- Yamamoto, M.; Iwai, Y.; Nakajima, T.; Arai, Y. Fourier Transform Infrared Study on Hydrogen Bonding Species of carboxylic Acids in Supercritical Carbon Dioxide with Ethanol. *J. Phys. Chem. A* **1999**, 103, 3525.
- Yeo, S.; Debenedetti, P. G.; Radosz, M.; Schmidt, H. Supercritical Antisolvent Process for Substituted Para-Linked Aromatic Polyamides: Phase Equilibrium and Morphology Study. *Macromolecules* **1993**, 26, 6207.
- Yonker, C. R. Solution Dynamics of Perfluorobenzene, Benzene, and Perdeuterobenzene in Carbon Dioxide as a Function of Pressure and Temperature. *J. Phys. Chem. A* **2000**, 104, 685.
- Yonker, C. R.; Linehan, J. C. Investigation of the Hydroformylation of Ethylene in Liquid Carbon Dioxide. *J. Organomet. Chem.* **2002**, 650, 249.
- Yonker, C. R.; Linehan, J. C.; Fulton, J. L. The Use of High Pressure NMR for the Determination of Phase Behavior for Select Binary Solvent Systems. *J. Supercritical Fluids* **1998**, 14, 9.
- Yonker, C. R.; Palmer, B. J. Investigation of CO<sub>2</sub>/Fluorine Interactions through the Intermolecular Effects on the <sup>1</sup>H and <sup>19</sup>F Shielding of CH<sub>3</sub>F and CHF<sub>3</sub> at Various Temperatures and Pressures. *J. Phys. Chem. A* **2001**, 105, 308.
- Yonker, C. R.; Wallen, S. L.; Linehan, J. C. Reaction Chemistries in Supercritical Fluid Solutions. *J. Micro. Separ.* **1998**, 10(1), 153.
- Yonker, C. R.; Zemanian, T. S.; Wallen, S. L.; Linehan, J. C.; Franz, J. A. A New Apparatus for the Convenient Measurement of NMR Spectra in High Pressure Liquids. *J. Magn. Reson.* **1995**, 113, 102.
- York, P.; Hanna, M. Particle Engineering by Supercritical Fluid Technologies for Powder Inhalation Drug Delivery. Conference on Respiratory Drug Delivery, Phoenix, 1995, 231.
- Zhang, R.; Liu, J.; He, J.; Han, B.; Wu, W.; Jiang, T.; Liu, Z.; Du, J. Organic reactions and nanoparticle preparation in CO<sub>2</sub>-induced water/P104/p-Xylene microemulsions. *Chem. Eur. J.* **2003**, 9(10), 2167.
- Zhang, Z.; Patel, R. C.; Kothari, R.; Johnson, C. P.; Friberg, S. E.; Aikens, P. A. Stable Silver Clusters and Nanoparticles Prepared in Polyacrylate and Inverse Micellar Solutions. *J. Phys. Chem. B.* **2000**, 104(6), 1176.